Development of novel Particle Image Thermometry methods for highly resolved measurements of temperature and velocity fields in fluids

Entwicklung neuartiger Particle Image Thermometry Methoden zur hochauflösenden Messung von Temperatur- und Geschwindigkeitsfeldern in Flüssigkeiten

TECHNISCHE
UNIVERSITÄT
DARMSTADT

Development of novel Particle Image Thermometry methods for highly resolved measurements of temperature and velocity fields in fluids

Vom Fachbereich Maschinenbau
an der Technischen Universität Darmstadt
zur
Erlangung des akademischen Grades Doktor-Ingenieur (Dr.-Ing.)
genehmigte

Dissertation

von Dipl.-Ing. Jan Vogt aus Miltenberg

1. Gutachten: Prof. Dr.-Ing. Peter Stephan
2. Gutachten: Prof. Dr.-Ing. Cameron Tropea

Tag der Einreichung: 29.04.2013
Tag der Prüfung: 11.07.2013

Darmstadt 2014
D 17

Für meine Familie

Erklärung zur

Hiermit versichere ich, die vorliegende ohne Hilfe Dritter nur mit den angegebenen Quellen und Hilfsmitteln angefertigt zu haben. Alle Stellen, die aus Quellen entnommen wurden, sind als solche kenntlich gemacht. Diese Arbeit hat in gleicher oder ähnlicher Form noch keiner Prüfungsbehörde vorgelegen.

Darmstadt, den 29.04.2013

(Jan Vogt)

Vorwort

Diese Arbeit entstand im Laufe meiner Tätigkeit als Stipendiat und wissentschaftlicher Mitarbeiter am Fachgebiet für Technische Thermodynamik der TU Darmstadt. Bei Herrn Prof. Dr.-Ing. Peter Stephan möchte ich mich ganz herzlich für die Betreuung der Arbeit, die Unterstützung und das entgegengebrachte Vertrauen bedanken. Zudem möchte ich hier die sehr guten Rahmenbedingungen für eine Promotion erwähnen, die am Fachgebiet geschaffen wurden. Vor allem die sehr gute Ausstattung der Labore (Laser, Hochgeschwindigkeitskameras, etc.) haben erst das Gelingen dieser experimentellen Arbeit ermöglicht. Bei Prof. Dr.-Ing. Cameron Tropea möchte ich mich zum einen für die Übernahme des Koreferats bedanken, zum anderen eröffnete er mir durch die Aufnahme als Stipendiat in das Graudiertenkolleg 1114 die Möglichkeit zur Promotion. Bedanken möchte ich mich auch bei allen weiteren Mitgliedern des GRK1114, die durch Diskussionen auf zahlreichen Seminar- und Klausurtagen neue Anstöße geliefert haben. Für die finanzielle Unterstützung durch das GRK1114/Deutsche Forschungsgemeinschaft möchte ich mich ebenfalls recht herzlich bedanken.

Bei allen Kollegen am Fachgebiet TTD möchte ich mich für die gute Stimmung am Institut, die Unterstützung jeglicher Art und die anregenden Unterhaltungen während der Mittagszeit bedanken. Besonders erwähnen möchte ich Ralph Nasarek, bei dem ich als Student im Rahmen meiner Diplomarbeit die Möglichkeit bekam in das Gebiet der optischen Messtechnik einzusteigen und der mich zu diesem Promotionsvorhaben ermutigte. Außerdem möchte ich im Besonderen Martin Still und Axel Sielaff für das Korrekturlesen der Arbeit und die niveauvollen Diskussionen bedanken.

Florian Erbacher, Andreas Preusche und Martin Liebig haben als Studenten in besonderem Maße zum Gelingen dieser Arbeit beigetragen und haben mich, auch bei längerdauernden Messkampagnen, stets bestens unterstützt.

Bei Gaby Gunkel, Ingrid Benz und Heike Kagerbauer möchte ich mich für die Unterstützung in allen möglichen Situationen und die Hilfe bei der Erledigung von Formalitäten bedanken.

An die Werkstatt des TTD ergeht ebenfalls mein herzlicher Dank für die Unterstützung bei allen experimentellen Vorhaben und die kompetente Umsetzung nicht immer normgerechter Zeichnungen.

Robert Schrod und Jörg Dittmann möchte ich für die sehr gute Kaffeekultur in unserem Büro danken. Robert Schrod unterstützte mich zudem in vielen Laborfragen und wenn der Laser einmal wieder streikte.

Zu guter letzt möchte ich mich bei meiner Frau Mareike für ihr Verständnis und alle Unterstützung während der gesamten Zeit der Promotion bedanken, ohne die diese Arbeit sicher nicht möglich gewesen wäre. Auch allen Freunden und dem Rest meiner Familie, insbesondere meinen Eltern, möchte ich für die Kinderbetreuung und die entgegengebrachte Unterstützung in allen Lebenslagen bedanken.

Weinheim, im April 2013

Jan Vogt

Kurzfassung

Die vorliegende Dissertationsschrift beschäftigt sich mit der Entwicklung eines Verfahrens für die simultane Messung von Temperatur- und Geschwindigkeitsfeldern in Flüssigkeiten, basierend auf lumineszierenden Partikeln. Dieses Verfahren soll für die experimentelle Untersuchung transienter Phasenwechselvorgänge, wie etwa dem Blasensieden, die sich auf kleinen räumlichen Skalen abspielen, eingesetzt werden. Somit ist eine Hauptanforderung an die entwickelte Messtechnik ein hohes räumliches und zeitliches Auflösungsvermögen. Bestehende Methoden bieten entweder keine entsprechend hohe Auflösung oder ermöglichen keine simultane Messung von Temperatur und Geschwindigkeit.

Zwei unterschiedliche Ansätze für die partikelbasierte Messung von Temperaturen werden vorgestellt. Für den ersten Ansatz werden Mikrokapseln genutzt, deren Kern aus einer Flüssigkeit besteht, in der ein temperatursensitiver Farbstoff gelöst wurde. Der zweite basiert auf der temperaturabhängigen Fluoreszenz eines Farbstoffgemisches, das direkt in ein Polymer eingebracht wurde. Die Fluoreszenzeigenschaften der entwickelten Mikrokapseln ermöglichen die Anwendung eines 2-Farb-LIF Messverfahrens. Die Anregung der Fluoreszenz erfolgt mit einem Laser bei einer Wellenlänge von 532 nm und die resultierenden Signale (temperaturabhängiges Signal und Referenzsignal) werden getrennt erfasst mittels zweier Hochgeschwindigkeitskameras und entsprechender optischer Filter. Dabei dient die Helligkeit der Partikel in den Bildern der beiden Kameras als Messgröße für die Temperatur. Die Geschwindigkeit ergibt sich aus aufeinanderfolgenden Bildern einer einzelnen Kamera durch Anwendung des PIV Verfahrens. Die Anwendbarkeit dieser Technik für hochauflösende Messungen wird sowohl für Aufbauten in denen die Beleuchtung durch einen Lichtschnitt erfolgt, als auch für solche mit Volumenbeleuchtung dargestellt. Zu diesem Zweck werden die Ergebnisse der experimentellen Untersuchung einer natürlichen Konvektionsströmung und einer druckgetriebenen Strömung innerhalb eines Kapillarröhrchens, mit dem Resultat einer entsprechenden numerischen Simulation verglichen. Weiterhin wird das entwickelte Messverfahren hinsichtlich Genauigkeit und möglicher Fehlerquellen charakterisiert.

Die mit temperatur-sensitiven Farbstoffen eingefärbten Polymere werden hingegen nur auf ihre generelle Anwendbarkeit für Temperaturmessungen untersucht.

Das Temperaturfeld um eine wachsende Dampfblase wird mittels laserinduzierter Fluoreszenz eines in Aceton gelösten, temperatursensitiven Farbstoffgemisches gemessen, womit auch die generelle Eignung optischer Messmethoden für diese zukünftige Anwendung analysiert wird.

Abstract

The subject of present thesis is the development of a technique for simultaneous measurement of temperature and velocity fields in liquids based on the luminescence of particles. This technique is intended to be used for the experimental investigation of transient phase change phenomena like nucleate boiling that takes place on a small spatial scale. For that reason, the main requirement for the developed technique is the ability for temporally and spatially highly resolving measurements. Existing methods either do not offer such high resolution or do not facilitate simultaneous temperature and velocity measurements.

Two different approaches for particle-based temperature measurements are presented, one using microcapsules with a temperature-sensitive dye solution in the core and the other using particles fabricated from dyed polymers. The developed microcapsules have a fluorescence characteristic that enables the implementation of a 2-colour-LIF procedure. Fluorescence is excited using a laser with a wavelength of 532 nm and the resulting signals (temperature-sensitive signal and reference signal) are detected by two separate high-speed cameras with appropriate filters. While the brightness of the particles in the images of both cameras serves as temperature indicator, velocity information is extracted from subsequent images of a single camera by means of the PIV method. The applicability of this technique for highly resolved measurements is shown for light-sheet and volume illumination. Therefore, experimental results from a stationary flow driven by natural convection and a flow through a capillary tube driven by a pressure difference are compared to the respective numerical solution of these flows. Moreover, the technique is characterized with regard to accuracy and possible sources of error.

The dyed polymers on the contrary, are only investigated with regard to their general applicability for temperature measurements.

Laser induced fluorescence with dyes dissolved in acetone is used to measure the temperature field around a growing vapour bubble and the suitability of optical methods for this future application is analyzed.

Contents

Nomenclature

Latin symbols

Symbol	Description	Unit
a	Thermal diffusivity	m^2/s
Bi	Biot number	-
C	1. Molar concentration	mol/m^3
	2. Mass concentration	kg/m^3
c_p	Specific heat capacity (constant pressure)	$J/(kgK)$
c_1	Ratio of dye concentrations in liquid core	-
d	Diameter (of microcapsules)	m
F_p	Pressure force	N
F_b	Buoyancy force	N
f	Focal length	m
Fo	Fourier number	-
g	Gravitational acceleration	m/s^2
I	1. Radiant flux ("Intensity")	W
	2. Identity matrix	-
I_{ex}	Irradiance of exciting light	W/m^2
K	Constants (specific for measurement setup)	-
l	Length	m
L	Length	m
M, N, n	Integer number	-
M^2	Quality factor	-
p	Pressure	N/m^2
P	Power	W
R	1. Ratio of temperature sensitive and reference signal	-
	2. Radius (of capillary tube)	m
r	Radius (of microcapsules)	m
Re	Reynolds number	-
S	Electrical measurement signal	V
s	Integer number	-
SNR	Signal-to-noise ratio	-
T	1. Temperature	K
	2. Relative transmission	-
t	Time	s
u	1. Velocity vector	m/s
	2. Velocity horizontal direction	m/s
v	Velocity vertical direction	m/s
V	Volume	m^3
$\dot{V}$	Volumetric flow rate	m^3/s
W	Matrix (Interrogation window)	-
w_{min}	Minimum beam waist	m

X	Matrix (resulting from cross-correlation)	-
x	1. Optical path in absorbing medium	m
	2. Coordinate	m
y	1. Optical path in absorbing medium	m
Z	Integer number	-
z	1. Coordinate	m
	2. Integer number	-

Greek symbols

Symbol	Description	Unit
α	Molar absorption coefficient	m^2/mol
β	Temperature sensitivity (exponential approach)	1/K
χ	Heat transfer coefficient	$W/(m^2K)$
ϕ	Quantum efficiency	-
Φ	Molar absorption coefficient times quantum efficiency	m^2/mol
κ	Thermal conductivity	W/(mK)
λ	Wavelength	m
μ	Dynamic viscosity	kg/m^3
ν	Kinematic viscosity	m^2 /s
π	Binding molecule orbitals	-
Θ_m	Dimensionless temperature	-
ρ	Density	kg/m^3
σ	1. Standard deviation	various
	2. Binding molecule orbitals	-

Subscripts

Subscript	Description
0	Initial value
A	Quantity related to camera A
B	Quantity related to camera B
b_1, b_2	Quantity of image 1, image 2
cams	Cameras
det	Detection unit
dichroic	Dichroic mirror
el	Electrical
em,max	Emission maximum
glyc	Glycerin
in	Inlet condition
max	Maximum
opt	Optical setup
ref	Reference signal
spec	Spectroscopic quantity
shortpass	Shortpass filter
single	Quantity without averaging
λ	Quantity at specific wavelength
sens	Temperature sensitive signal
total	Quantity of temperature sensitive signal divided by quantity of reference signal

Superscript

Superscript	Description
$*$	Excited state

Abbreviations

Abbreviation	Description
CCD	Charge-coupled device
CMOS	Complementary metal-oxide-semiconductor
D	Donor
DCM	4-(Dicyanomethyl)-2-methyl-6-(4-dimethyl-amino-styryl)-4-H-pyran
EuTTA	Europium thenoyltrifluoroacetonate
FEP	Fluorinated ethylene propylene
LBO	Lithium triborate
LED	Light emitting diode
LIF	Laser induced fluorescence
Nd:YAG	Neodymium-doped yttrium aluminum garnet
PBMA	Polybutylmethacrylate
PIT	Particle image thermometry
PIV	Particle image velocimetry
PMMA	Poly(methyl methacrylate)
PM567	Pyrromethene 567
PM597-8C9	Pyrromethene 597-8C9
PTFE	Polytetrafluoroethylene
PVAc	Polyvinyl acetate
Q	Quencher
RGB	Red green blue
Rh19	Rhodamine 19
Rh110	Rhodamine 110
RhB	Rhodamine B
Ru(bpy)	Tris(bipyridine)ruthenium
S	Singlet state
SNR	Signal-to-noise ratio
SRhB	Sulforhodamine B
T	Triplet state
TC	Thermocouple
TLC	Thermochromic liquid crystal
TSP	Temperature sensitive paint
UV	Ultraviolet

1 Introduction

1.1 Motivation

In many applications in science and industry, the measurement of temperature is of great importance. Besides widely-used contacting measurement devices, like thermocouples, resistor-type thermometer or liquid expansion thermometer, non-contacting optical temperature measurement methods exist. The great progresses in camera technology and soft- and hardware for image processing caused a rapidly growing spread of optical measurement techniques in the last decade. The development of digital high-speed cameras with framerates up to 15000 fps and more than 1000×1000 pixels lead to an increasing importance of these techniques in science.

One great advantage of optical methods is their non-invasive or only slightly invasive character, meaning that the observed object or medium is not or only minimally affected by the measurement. Moreover, contacting measurement devices offer temperature information only at one single point, while optical methods with cameras can resolve the temperature distribution in two dimensions.

Optical measurement techniques are of particular interest, if phenomena taking place on small spatial and temporal scales are to be observed. In the field of heat transfer such small-scale, highly transient mechanisms play an important role during nucleate boiling and other phase transition processes. However, these mechanisms are only partly understood due to their complex nature. They are the subject of recent research activities, since the energy efficiency of many devices and industrial processes can be increased by an optimization of the heat transfer rates. Experimental investigations using optical measurement methods can help to understand these phenomena and to validate existing numerical models.

For temperature measurements by optical methods, there are different physical phenomena such as the infrared radiation of matter or the fluorescence of certain substances after proper excitation that can be used as indicators. Due to the coupling of heat and mass transfer in the applications mentioned above, a proper measurement technique should be able to determine temperature and velocity fields simultaneously with a high temporal and spatial resolution. Well-established techniques, like laser-induced fluorescence (LIF) and particle image velocimetry (PIV) can only measure temperature and velocity separately. One existing method for simultaneous measurement of these parameters is the particle image thermometry (PIT) using thermochromic liquid crystals (TLCs), which does not offer a sufficiently high resolution. Further methods for simultaneous temperature or velocity measurements exist, but they are only poorly investigated and offer some crucial drawbacks.

1.2 Goals and conception

The goal of the present thesis is the development and experimental characterization of a method for simultaneous measurement of temperature and velocity fields in liquids, facilitating experimental analyses with high temporal and spatial resolution.

The basic concept is the combination of LIF and PIV using particles that exhibit luminescent properties depending on temperature. Velocity fields can be determined from the displacement of the particles in subsequent images and the temperature is calculated from the luminescence characteristics that are represented by the brightness of the particles in the images.

Two different techniques for the creation of such particles were identified and are investigated:

- Microencapsulation of a solution containing fluorescent dyes,
- Solid particles with luminescent dyes incorporated in the polymer matrix.

For both types of particles, the temperature is determined from the ratio of a temperature-sensitive luminescent signal and a reference luminescent signal, following the 2-colour-LIF (or ratio-metric LIF) approach. The reference signal is necessary to compensate for fluctuating factors (e.g. particle size or illumination intensity) that influence the intensity of the luminescent signal. These signals are detected by high-speed cameras, which facilitate two-dimensional measurements with a high temporal resolution.

In preliminary investigations, appropriate dyes must be identified showing the desired temperature-sensitive luminescent characteristics in the solution of the microcapsules' core respectively when they are incorporated in a polymer. The next step is the fabrication of microcapsules or dyed polymer particles with suitable dyes and their examination with regard to their applicability for temperature measurements. Therefore, a benchmark experiment must be developed and implemented, which allows the characterization of the developed technique with regard to accuracy and resolution, by comparison of measurement results with accordant numerical simulations or theoretical analyses.

The development of appropriate image processing algorithms for the fast and automated analysis of acquired camera images is an essential part of the this thesis.

2 State of the art

In the first part of this chapter physical laws that govern photoluminescence phenomena are explained. Based on this knowledge, principle aspects of existing optical temperature and velocity measurement techniques are illustrated and relevant publications for each method are discussed.

2.1 Physical principle

The spontaneous emission of photons by excited atoms or molecules is generally called fluorescence. Substances that can be added to another medium (e.g. dissolved in a liquid) and show fluorescence after proper excitation are commonly named "fluorescent dyes" or simply "dyes". Some of these dyes show a fluorescent emission characteristic that depends on temperature and can thus be used as an optical indicator for temperature measurements by means of the laser-induced fluorescence (LIF). The physical principle of fluorescence will be described in detail in the following section and further phenomena like photobleaching, solvent relaxation and self-absorption that can have a significant influence on the measured signal are explained.

2.1.1 Photoluminescence

Fluorescence and phosphorescence are combined in the term "Photoluminescence". The exact difference between fluorescence and phosphorescence will be explained in the course of this section. Photoluminescence is an example for the interaction of matter and electromagnetic radiation. It results from absorption and spontaneous reemission of a photon by a molecule. A photon is absorbed when the photon's energy matches the energy gap between energetic states of this molecule.

These energetic states can be subdivided into electronic, vibrational and rotational energy states. Figure 2.1 shows the three different types of energetic states and their typical energy gaps. Electronic energy states correspond to the potential energies of electrons in the molecular orbitals. The transition between two electronic states typically correlates with radiation in the visible range.

Due to the oscillations of single atoms or groups of atoms in the molecule, different vibrational energetic states exist. Usually, the energy differences between vibrational states are as big as the energy that a photon in the infrared range possesses.

The rotation of two or more atoms around a shared center of mass leads to different rotational energy states in the molecule. Rotational energy is comparatively small and corresponds to radiation in the microwave range.

Electronic excited states

Molecular orbitals can be seen as the interference of atomic orbitals that are available for bonding interactions in the molecule. Additive (symmetric) combination of atomic orbitals results in bonding molecular orbitals (σ and π orbitals) and the subtractive (antisymmetric) combination in antibonding molecular orbitals (σ^* and π^* orbitals) respectively. For some molecules also non-bonding orbitals (n orbitals) exist.

Bonding orbitals reduce the molecule's total energy and consequently stabilize the molecule, while antibonding orbitals increase the total energy and therefore destabilize the molecule.

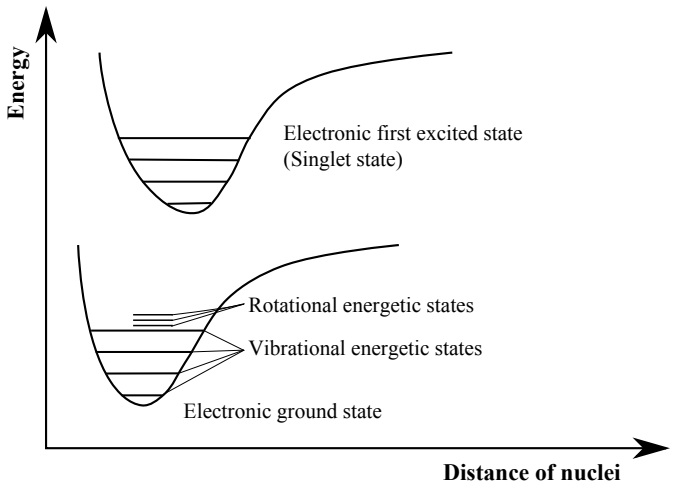

Figure 2.1: Different energetic states of a notional molecule. Energy differences of electronic states are larger than energy differences of vibrational and rotational energetic states. Note that the rotational states exist for all other vibrational states as well, but are not shown in this Figure (after Haken and Wolf [25]).

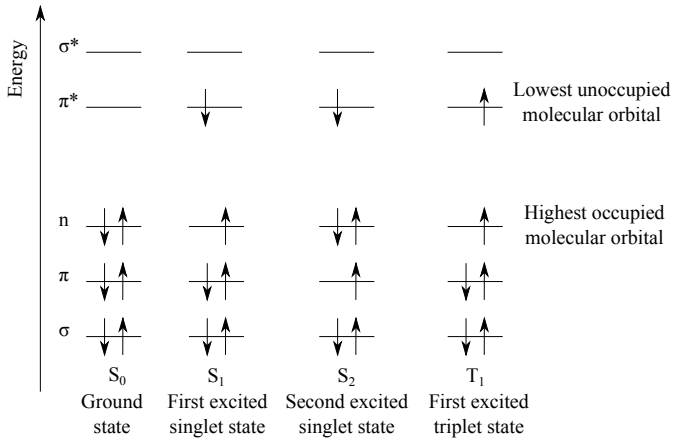

Figure 2.2: Illustration of bonding, antibonding and non-bonding molecule orbitals and their occupation in different electronic states. Arrows symbolizing electrons in the orbitals. Their spin is indicated by the arrows direction (after Susdorf [79]).

Figure 2.2 shows the occupation of the previously described σ, π, σ^*, π^* and n orbitals for different electronic states (S_0 ground state, S_1 first singlet (excited) state, S_2 second singlet state, T_1 triplet state) of a notional molecule. In the triplet state the resulting unpaired electrons are parallel, so that the total spin is 1 (each electron's spin equals 1/2), while in the singlet state the unpaired electrons have anti-parallel spin, resulting in a total spin of 0.

Therefore the transitions from the singlet to the triplet states are spin-forbidden processes due to different multiplicities. However this so called Intersystem-Crossing is allowed by spin-orbit coupling, which is particularly facilitated by the presence of a heavy atom [82].

Figure 2.3 shows the so called Jablonski diagram illustrating different energetic states that were previously described. Possible transitions between energetic states are indicated by arrows. A molecule is excited from ground state to the singlet state ($S_0 \rightarrow S_1$) by absorption of a photon of adequate energy.

The radiative transition from a singlet state to the ground state ($S_1 \rightarrow S_0$) (a photon is emitted) is in general called fluorescence, while the radiative transition from the triplet state to the ground state

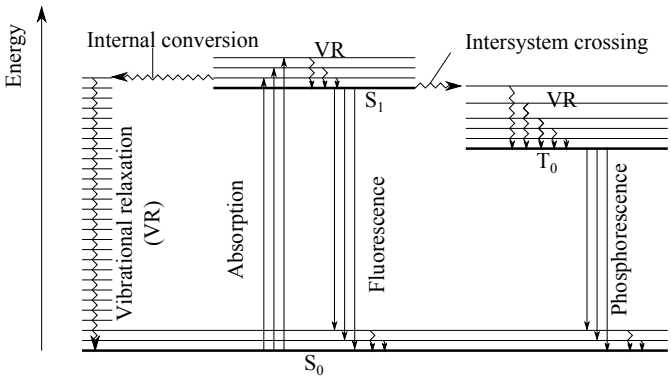

Figure 2.3: Jablonski diagram visualizing energetic states and possible radiative (straight arrows) und radiationless transitions (staggered arrows) between these states (after Valeur [82]).

($T_1 \rightarrow S_0$) (which is also a spin-forbidden process) is called phosphorescence. Besides that, non-radiative transitions (vibrational relaxation, internal conversion, intersystem crossing) occur. All these phenomena will be explained in more detail in the following sections.

2.1.2 Absorption of light

Absorption of a photon with appropriate energy causes an electronic transition of a dye molecule from the ground state to the singlet state ($S_0 \rightarrow S_1$). This transition can occur from any existing vibrational energy level of S_0 to any vibrational energy level of S_1.

Big organic molecules (dye molecules) have got many vibrational and rotational degrees of freedom. Thus, overlapping vibrational and rotational energetic states lead to a broad, continuous absorption spectrum instead of many discrete lines of absorption. Figure 2.4 shows the typical absorption and emission spectrum of a dye molecule in solution.

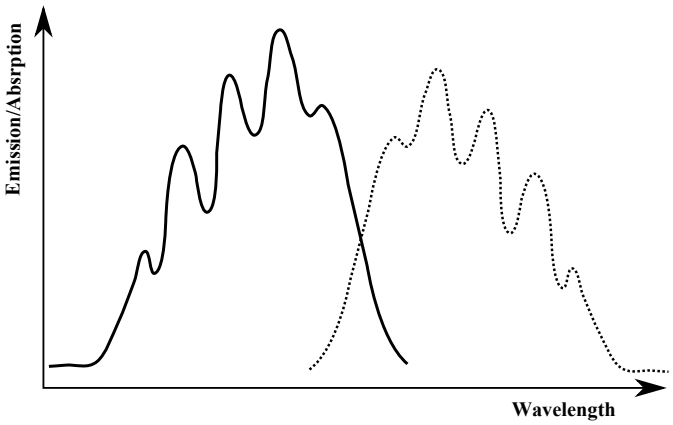

Figure 2.4: Absorption (solid line) and emission (dashed line) spectra of a notional dye molecule in a liquid solvent. No single absorption/emission lines can be observed, but a continuous absorption/emission band.

Absorption normally occurs from the lowest vibrational level of the S_0 state to any vibrational level of the S_1 state, while fluorescence is taking place from the lowest vibrational level of the S_1 state to any vibrational level of the S_0 state (ground state). For that reason, emission and absorption spectra appear mirrored. Due to radiationless deactivation of the excited state, the number of emitted photons is lower than the number of absorbed photons.

Overlapping of the emission and absorption spectrum can be observed, because absorption can also take place from higher vibrational states of the electronic ground state and occupation of vibrational states follows a Boltzmann distribution.

Absorption is a very fast process and takes place within 10^{-15} s [79]. In principal there are two possibilities for the excited molecule to go back to ground state: First the radiative deactivation (photon emission) and the radiationless deactivation, which will both be described in the following sections.

2.1.3 Radiative deactivation (fluorescence, phosphorescence)

As previously described, there are two radiative processes bringing a molecule from an excited state to the ground state. Depending on the multiplicity of the excited state, the process is called fluorescence ($S_1 \rightarrow S_0$ transition) or phosphorescence ($T_1 \rightarrow S_0$ transition). While fluorescence is taking place within 10^{-9} s to 10^{-7} s, phosphorescence has typically longer lifetimes reaching from 10^{-6} s up to some minutes. This is due to the fact that the $T_1 \rightarrow S_0$ transition is a spin-forbidden process, and therefore very unlikely to happen, while also the intersystem crossing to the S_0 state is not efficient due to the high energy difference [66].

For fluorescence and phosphorescence the wavelength of the absorbed light is shorter than the wavelength of the emitted light. This difference in wavelength is called Stokes-shift and can be explained by the vibrational relaxation taking place on a short timescale 10^{-12} s prior to the fluorescence or phosphorescence. For that reason, the radiative deactivation always takes place from the lowest vibrational energy level of the excited state and the emission spectrum is independent from the excitation wavelength.

2.1.4 Intramolecular radiationless deactivation

As shown in Figure 2.3, there are different ways for the excited molecule to get back to the ground state. All the effects shown there are intramolecular effects. Internal conversion denotes the transition of an electronic excited state S_1 to a vibrational level of the ground state S_0, while the total energy of the molecule is preserved. It can be promoted by specific molecular groups, allowing an intramolecular energy transfer and thus facilitating the existence of vibrational states with high energies. Since the occupation of vibrational energy levels follows a Boltzmann distribution, the probability for internal conversion also depends on temperature [46], [31].

From these vibrational (and rotational) states with higher energy this energy is transfered to the surrounding molecules until a thermal equilibrium is reached. This dissipation of energy is called vibrational relaxation. Intersystem crossing describes the transition from states with different multiplicities (singlet $\rightarrow$ triplet state). As mentioned previously, this is a spin-forbidden process, but allowed by spin-orbit coupling. The effectiveness of intersystem crossing is increased in the presence of heavy atoms, but can also be influenced by the surroundings.

2.1.5 Intermolecular radiationless deactivation

Other possibilities for the deactivation of excited states exist when the excited molecule interacts with its environment. The reduction of fluorescent intensity by these intermolecular processes that will be described in the following, is generally called fluorescence quenching [82].

The electronically excited molecule (D*) can transfer energy to the surrounding medium (Quencher (Q)) by a mechanism called Fluorescence Resonance Energy Transfer (FRET). Therefore, no direct contact between D* and Q is necessary, as the energy is transfered via dipole-dipole interactions. After this interaction, Q is in the excited state (Q*) [66].

Collisional quenching, on the contrary, requires direct contact between D* and Q. The excitation energy is converted to vibrational and rotational energy so that both molecules are in the ground state after this interaction.

Special substances can act as very effective quenchers, which means that the fluorescence intensity is reduced in their presence. Oxygen is such a matter due to fact that a triplet ground state exists. It serves as a "catalyst" that brings the excited molecule (singlet state) very effectively to the triplet state. In the long-living triplet state, the dye molecule does not exhibit fluorescence [65].

2.1.6 Chemical processes and photobleaching

There are numerous processes that can influence or destroy dye molecules decreasing the fluorescence intensity. Unlike the fluorescence quenching phenomena, they lead to an irreversible deactivation of dye molecules. One such process is photobleaching that can be caused by multiple electronic excitations of the dye (especially from the long-living triplet state, $T_1 \rightarrow T_n$), inducing a destabilization of the molecule and consequently its dissociation [65], [39].

Chemical reactions can lead to the formation of dimers or complexes, which do not show any or an altered fluorescence.

2.1.7 Solvent relaxation

Electronic excitation leads to an expansion of the electron cloud and therefore changes the molecule's polarity. This again induces a reorientation of the surrounding solvent molecules. The energy level of the excited molecule is decreased, because this reorientation dissipates part of the excitation energy. Therefore, in the following radiative transition to the ground state, a photon of less energy is emitted and consequently the light is shifted to longer wavelengths [37], [65], [96]. Due to this phenomenon, the solvent polarity and viscosity can have a significant influence on the fluorescence characteristics.

2.1.8 Temperature sensitivity of quantum yield

The quantum yield ϕ describes the quotient of emitted photons Z_{emitted} to absorbed photons Z_{absorbed}.

$$\phi = Z_{\text{emitted}}/Z_{\text{absorbed}}$$

It ranges from 0 to 1 depending on the probabilities for radiative and radiationless deactivation of the excited state. As these probabilities are depending on various intramolecular (section 2.1.4) and intermolecular interactions (section 2.1.5), ϕ can be influenced by the molecular structure of the dye molecule and the solvent's properties (temperature, polarity, viscosity).

An increase of temperature leads to the occupation of states with higher vibrational energy and therefore it makes internal conversion more probable. Additionally, intermolecular energy transfer (fluorescence quenching) is more effective due to the increased kinetic energy of the solvent molecules. Both phenomena lead to a decrease of the fluorescence intensity with increasing temperature, which can be observed for most dyes used for LIF-measurements.

As explained in section 2.1.7, polarity (and viscosity) strongly influence the fluorescence and therefore also the temperature sensitivity of ϕ. This can be observed for rhodamine B (a popular temperature-sensitive dye for LIF), which shows a temperature sensitivity of -2.6 %/K in water and only -1.4 %/K in ethanol [51].

Due to the complex concurrences of influencing factors, only vague predictions can be made for the temperature sensitivity of a dye molecule in a specific solvent. The influence of temperature on the fluorescence emission has to be determined experimentally.

2.1.9 Self-absorption and re-emission effects caused by Beer-Lambert's law

Due to an overlap of emission and absorption spectra that most fluorescing substances exhibit, part of the emitted light is re-absorbed, while it travels through the fluorescing medium. This process is known as self-absorption. Corresponding to the quantum yield, a part of the re-absorbed light causes fluorescent emission at longer wavelengths, which is named re-emission. These effects can strongly affect the temperature measurement for some applications and thus some theoretical aspects of self-absorption and re-emission are discussed in the following.

The attenuation of light traversing an absorbing fluid is described by the law of Beer-Lambert with the following equation [25]:

$$I = I_0 e^{-\alpha C x} \tag{2.1}$$

where I_0 denotes the initial intensity for the path length $x = 0$ through the absorbing medium. C represents the concentration of the absorbing substance in the fluid, with the coefficient of absorption α. Considering two signals $I_{\lambda 1}$, $I_{\lambda 2}$ at different wavelengths, the equation is rewritten as

$$I_{\lambda 1} = I_{0,\lambda 1} e^{-\alpha_{\lambda 1} C x} \tag{2.2}$$

Thus the ratio of $I_{\lambda 1}$ and $I_{\lambda 2}$ is described by

$$R = \frac{I_{\lambda 1}}{I_{\lambda 2}} = \frac{I_{0,\lambda 1}}{I_{0,\lambda 2}} \cdot e^{(\alpha_{\lambda 2} - \alpha_{\lambda 1}) C x} \tag{2.3}$$

From equation 2.3 it becomes clear that the ratio of two signals at different wavelengths depends on the optical path length x through the absorbing medium, concentration C and the difference between the absorption coefficients.

Above equations are generally valid for absorbing substances showing no fluorescence. For fluorescing substances the situation is more complex, as part of the absorbed light is re-emitted at longer wavelengths increasing the ratio's dependency on the path length.

In the following, it is assumed that $\alpha_{\lambda 2}$ is zero, which is valid if λ_2 is on the right side of the overlapping region of absorption and emission (see Figure 2.4). On the contrary, λ_1 is chosen within this overlapping region. Taking two fluorescence signals $I_{0,\lambda 1}$ and $I_{0,\lambda 2}$ generated at one point in the medium, the ratio R of the signals $I_{\lambda 1}$, $I_{\lambda 2}$ detected at a distance x is

$$R = \frac{I_{\lambda 1}}{I_{\lambda 2}} = \frac{I_{0,\lambda 1} e^{-\alpha_{\lambda 1} C x}}{I_{0,\lambda 2} e^{-\alpha_{\lambda 2} C x} + (1 - e^{-\alpha_{\lambda 1} C x}) I_{0,\lambda 1} \phi} \tag{2.4}$$

where the second summand in the denominator represents the re-emitted portion of the absorbed signal (λ_1). The quantum efficiency ϕ specifies the ratio of re-emitted and absorbed photons.

Simplifying equation 2.4 for the case that $I_{0,\lambda 1} = I_{0,\lambda 2}$ (initial intensities are the same for both wavelengths), the correlation between ratio R and x taking into account fluorescent re-emission can be expressed by

$$R = \frac{e^{-\alpha_{\lambda 1} C x}}{1 + \phi (1 - e^{-\alpha_{\lambda 1} C x})} \tag{2.5}$$

From equation 2.5 it can be recognized that the enumerator decreases with the path length x and concentration C while the denominator increases. Hence, R shows a stronger dependency on x and C when fluorescent re-emission is considered than for the case of pure absorption (see equation 2.3).

One possibility of minimizing the effect of re-absorption is the reduction of the dye's concentration. However, if the dye concentration is reduced, the fluorescent intensity decreases as well. Thus, there is a clear trade-off between signal intensity and reduction of reabsorption effects.

This source of errors was mentioned by Coppeta and Rogers [16] when the ratiometric LIF method was introduced. Lavieille et al. [40] analyzed the phenomenon of re-absorption in detail and corrected the influence of the optical path length by the use of a third spectral band (three-colour-LIF).

2.2 Optical methods for temperature measurements

2.2.1 LIF and 2-colour-LIF

The previously described dependency of the fluorescent emission from different factors can be used to measure these parameters by inducing fluorescence and detecting the emitted signal. Most commonly, LIF is used for concentration and temperature measurements in gases and condensed media. For the present work, only the use of LIF for temperature measurements in liquids is relevant and will be explained in the following.

LIF measurement principle and basic equations

Lemoine et al. [42] derived the following equation to describe the correlation between the fluorescent signal S and the temperature T:

$$S = I_{ex} C V K_{opt} K_{spec} \exp \frac{\beta}{T} \tag{2.6}$$

where I_{ex} indicates the intensity of the exciting light, C is the concentration of the dye in the liquid, V the measurement volume, and K_{opt} and K_{spec} are constants characterizing the spectral and optical properties of the detection system. The variable β describes the temperature sensitivity of the dye used.

Sakakibara et al. [26], [62], [63], [60] used the following equation to describe the correlation between the fluorescence intensity I emitted from a specific measurement volume V

$$I = I_{ex} C V \phi \alpha \tag{2.7}$$

where ϕ represents the quantum yield and α the absorption coefficient. For most dyes used for LIF in liquids, the absorption does not show a significant dependency on temperature, while ϕ does as described in section 2.1.8. However, for the LIF measurements the contributions of α and ϕ are combined in a single temperature sensitive variable Φ describing the ratio of incident photons and emitted photons for a measurement volume with dye concentration C.

Taking into account the characteristics of the optical setup (e.g. transmission of filters) and the detection system (e.g. quantum efficiency of cameras) by introduction of K_{opt} and K_{det}, the following equation is derived from a combination of equation 2.6 and equation 2.7

$$S = I_{ex} C V K_{opt} K_{det} \Phi(T) \tag{2.8}$$

To have a definite correlation between the measured signal S and the temperature T, all parameters besides Φ must be constant and a calibration has to be performed. The derivative of Φ with respect to temperature $\mathrm{d}\Phi/\mathrm{d}T$ is also called temperature sensitivity. For many dyes, the temperature sensitivity is nearly constant in the considered temperature range. Therefore, the change rate of fluorescent intensity with temperature is often specified in %/K.

The criterion of constant parameters cannot be met for most cases, since I_{ex} is subject to variations due to fluctuating laser power and inhomogeneous illumination. Moreover, V might also vary (e.g. in case of microencapsulated dyes). To overcome this problem, the so-called 2-colour-LIF (or ratio-metric-LIF) has been introduced by Coppeta and Rogers [16] and Sakakibara et al. [60]. In their approaches, a reference signal that shows no or only small dependency on temperature is used to compensate the fluctuations of I_{ex} and V. The temperature-sensitive signal and the reference signal must differ in their wavelengths, in order to be detected separately. The ratio R of both signals still depends on temperature, while the dependencies on the fluctuating parameters I_{ex} and V is eliminated. In the following equation,

subscript "sens" and "ref" denote the parameters for the temperature sensitive signal and the reference signal respectively.

$$R(T) = \frac{S_{\text{ref}}}{S_{\text{sens}}} = \frac{I_{\text{ex}} C_{\text{ref}} V K_{\text{opt,ref}} K_{\text{det,ref}} \Phi_{\text{ref}}(T)}{I_{\text{ex}} C_{\text{sens}} V K_{\text{opt,sens}} K_{\text{det,sens}} \Phi_{\text{sens}}(T)} \tag{2.9}$$

There are two possibilities to provide the reference signal. Either one single dye is used that shows a characteristic emission spectrum with different temperature sensitivities in specific spectral ranges (1-dye-2-colour-LIF) [10], [41], or a second dye with low temperature sensitivity is added (2-dye-2-colour-LIF) [16], [60].

For the first approach, C_{sens} equals C_{ref} and thus both can be cancelled out. For the 2-dye-2-colour-LIF approach, which is also used in the present thesis, the following equation is derived from equation 2.9 by combining the single dye's characteric parameters to one total constant that is valid for the dye mixture.

$$R(T) = \frac{C_{\text{ref}}}{C_{\text{sens}}} K_{\text{opt,total}} K_{\text{det,total}} \frac{\Phi_{\text{ref}}(T)}{\Phi_{\text{sens}}(T)} \tag{2.10}$$

The emission and absorption spectra for an idealized mixture of a sensitive and a reference dye are illustrated in Figure 2.5. To have a high temperature sensitivity, $\mathrm{d}\Phi_{\text{sens}}/\mathrm{d}T$ and $\mathrm{d}\Phi_{\text{ref}}/\mathrm{d}T$ must differ as much as possible. In the case of an ideal dye mixture, as presented in Figure 2.5, $\mathrm{d}\Phi_{\text{ref}}/\mathrm{d}T = 0$. Another requirement is that the concentrations of both dyes are the same at all measurement positions, so that $C_{\text{ref}}/C_{\text{sens}}$ is a constant. The correlation between the ratio R and the temperature T must be evaluated by means of an in-situ calibration. In the ideal case shown in Figure 2.5, the emission spectra are completely separated from the absorption spectra and both emission spectra show no overlap among each other.

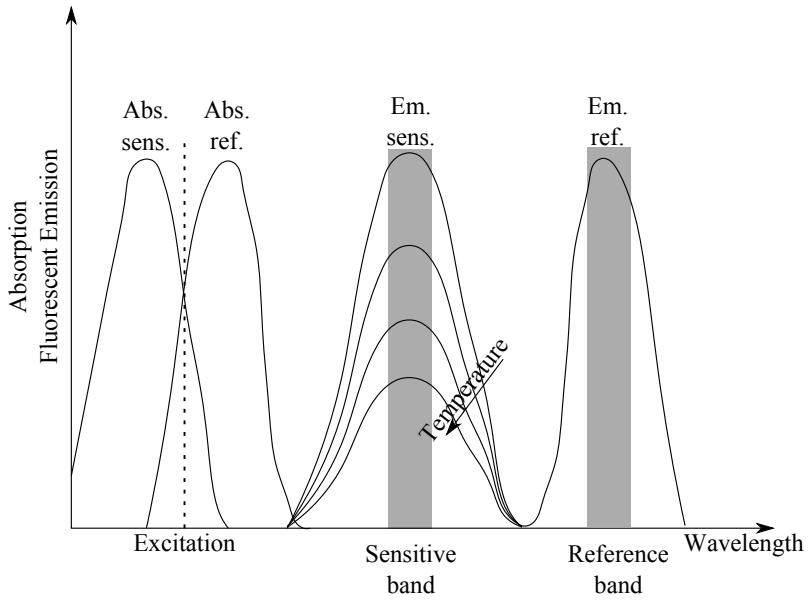

Figure 2.5: Principle of the 2-colour-LIF method showing the emission and absorption characteristic of an ideal dye mixture.

Macro-scale applications of LIF

Walker [87] used fluoresceine sodium for 0-dimensional concentration measurements. He also investigated the effect of the pH-value and temperature on the measured intensity and observed significant influences.

The most common dye used for LIF temperature measurements is rhodamine B (RhB). Sakakibara et al. used RhB to measure the temperature field during mixing of two differentially tempered water flows in an optically accessible pipe [62] and the heat transfer during impingement of a water jet on a heated surface [63]. For the latter measurements, they stated a temperature measurement uncertainty of ± 1.2 K and a spatial resolution of $2 \times 0.4 \times 0.4$ mm^3.

A detailed study about the sources of error for 1-color-LIF temperature measurements has been carried out by Coolen et al. [15]. They also used RhB in water and identified photobleaching effects, shadowgraph effects and fluctuating laser power as main sources of error. Applying an appropriate correction of photobleaching and laser power, they achieved an accuracy of ± 1.7 K for the measurements of the temperature field during natural convection in a cubic test cell (similar to the setup presented in section 3.1.4). Shadowgraph effects lead to a local variation of the excitation energy. They result from the temperature dependency of the refractive index of water and are thus a function of the measurand. Minimizing the temperature gradients occurring along the propagation direction of the light sheet, reduces shadowgraph effects.

Sakakibara and Adrian [60], [61] introduced the 2-colour-LIF method to measure the thermal convection over a heated horizontal surface 2-dimensionally. They used RhB as sensitive and Rh110 as reference dye and two separate monochrome CCD-cameras with appropriate filters for fluorescence detection. Fluorescence excitation was realized by the 488 nm emission line of an Argon-Ion laser. In their first experiments 1999 [60], the statistical error was evaluated to be ± 1.4 K for a temperature field measurement with an artificially perturbed laser sheet. Using enhanced image processing (blurring correction) and CCD-cameras with a high dynamic range (14 bit), they reduced the statistical error to ± 0.17 K for the temperature field measurements in Rayleigh-Bénard convection (thermal convection in horizontal fluid layer heated from below and cooled from above) [61]. An error analysis showed that the statistical error is mainly caused by noise in the cameras.

Lavieille et al. [41], [11] used the 2-colour-LIF for temperature measurements in evaporating ethanol droplets. However, in their approach (1-dye-2-colour-LIF) no second dye was added, but a second spectral region of the RhB fluorescent emission, for which a significantly reduced temperature sensitivity was observed, was used as reference. This reference band is situated close to the wavelengths of minimum emission. Hence also the detected fluorescent signal is low. For these experiments, however, photomultipliers with appropriate optical filters are used as detectors. Because photomultipliers have a much higher light sensitivity than CCD-cameras, the low fluorescent signal is not problematic. The random error was estimated to be approximately ± 2 K. In later publications this group introduced the measurement of a third spectral band to correct for errors caused by fluorescent reabsorption (see section 2.1.9). The applicability of this technique was demonstrated for a heated jet flowing in a water bath with a large optical path [40] and for evaporating binary droplets [47]. The 1-dye-2-colour-LIF has been extended to a 2-dimensional measurement technique by Bruchhausen et al. [10]. Two CCD-cameras were used for temperature measurements around a heated jet flowing in a water bath that was illuminated with a laser light sheet. The spatial resolution is determined to be 0.27×0.27 mm^2, while no statement is made about the uncertainty of the temperature measurements.

Mini-/Micro-scale applications of LIF

While the applications mentioned above all have a big field of view (centimeter range) and rather low spatial resolution, LIF has also been used for mini-/micro-scale applications. Ross et al. [59] used a standard fluorescence microscope with a CCD-camera, to investigate the temperature distribution in a microchannel during electrokinetic pumping which increases the temperature of the aqueous buffer solution due to Joule heating. They used the single-dye-technique (RhB as sensitive dye) and a mercury arc lamp with an appropriate filter for excitation (instead of a laser), which results in a quite low precision of ± 3.5 K. The systematic error has not been evaluated, but it might be comparatively high due to

lacking in-situ calibration. However they achieved a high spatial resolution of 1×1 μm^2 and a temporal resolution of 33 ms.

Natrajan and Christensen [51] extended the 2-colour-LIF technique for the use in micro-scale applications. They used a combination of RhB (sensitive dye) and Sulforhodamine101 (reference dye) in two different applications with different solvents (water and ethanol). A pulsed Nd:YAG-laser (second harmonic: 532 nm) has been applied, providing sufficient excitation energy in a time-scale that is short enough for instantaneous temperature measurements during thermal transports at the micro-scale. However, Rh110 that has been commonly used in 2-colour-LIF experiments in the macro-scale, cannot be applied due to its poor absorption at 532 nm. Sulforhodamine 101 was chosen as alternative. The optical setup includes a fluorescence microscope with an additional dichroic mirror and two cameras with appropriate filters for the separate detection of the sensitive and the reference signal. The technique was implemented for a set of parallel microchannels to which a temperature gradient perpendicular to the flow direction was applied. This results in a linear decrease of temperature from channel to channel, which can easily be determined in an analytical manner. A spatial resolution of 22.2×22.2 μm^2 was achieved and a measurement uncertainty of ± 0.59 K in ethanol and ± 0.49 K in water was reported. This effect of the solvent can be attributed to the different temperature sensitivities of RhB in water (-2.7 %/K) and ethanol (-1.5 %/K) respectively.

Due to limited optical access, volume illumination has to be used for most μLIF applications. Accordingly, fluorescing molecules along the beam propagation are excited and contribute to the measurement signal. If steep temperature gradients along the optical axis exist, they can produce significant errors, since the measured signal is an average of the temperature-dependent fluorescence from different measurement planes. According to [51] the comparatively high uncertainty can at least partly be attributed to the use of volume illumination, since for comparable macro-scale measurements a precision of ± 0.17 K has been reported in [61].

On the contrary, Chamarthy et al. [13] used the well-known combination of RhB and Rh110 to investigate the mixing of differentially tempered flows at the T-junction of a microchannel. Instead of using two cameras for the fluorescence detection, a standard microscope setup with a single camera was used. The sensitive signal and the reference signal are consecutively imaged onto the same camera. A filter wheel in the excitation path is used to separately excite the fluorescence of RhB and Rh110. A similar approach has been used by Kim et al. [32] to investigate the temperature field in a capillary tube. However, in their approach the filter wheel was positioned in the emission path, separating the fluorescent signals of RhB and Rh110. Both methods yield the advantage that the optical setup can be realized with minor effort and standard components.

But, this approach of temporal signal separation and detection has two major disadvantages. Firstly, only long-term steady-state phenomena can be observed, since the mechanical change of filters takes very long compared to the acquisition time of the camera. Secondly, and more importantly, the effect of fluctuating excitation on the temperature measurements cannot be removed by this technique. If the excitation source energy is subject to fluctuations, the excitation during acquisition of the sensitive image is different from that during acquisition of the reference image. Thus, only local, stationary differences of excitation energy can be considered. Chamarthy et al. compared the precision of their 2-colour-technique to the single-color technique (same measurements, only sensitive images are used) and reported values of ± 2.68 K (2-colour-LIF) and ± 1.25 K (1-colour-LIF). This result is in line with the above explanations, since no fluctuations of excitation can be compensated, while the overall noise is increased by the division of the two noisy signals (sensitive image divided by reference image). Thus, for these measurements no advantage of using the 2-colour-LIF method can be noticed.

LIF measurements with high temporal resolution

In order to resolve highly transient phenomena, a suitable measurement technique has to fulfill two key requirements. Firstly, it should have a short integration time to avoid temporal blurring. This is

achieved by pulsed lasers with pulse-lengths in the nanosecond regime. Secondly, a high acquisition rate of the fluorescence detection system is necessary, which can be realized by means of digital high-speed cameras (CMOS-cameras). In literature CCD-cameras with low acquisition rates (at maximum 60 Hz) are commonly used as detectors for LIF measurements, which limits the feasible temporal resolution.

Nasarek [50] investigated the applicability of CMOS-cameras for 1-colour-LIF and 2-colour-LIF applications using a setup similar to that described in section 3.1.4. The temperature field in a cubic cell with a flow driven by natural convection was measured by means of the 1-colour-LIF method. A good agreement with numerical simulations was found. The limiting factor for the temporal resolution was the acquisition rate of the used camera (650 fps). In the case of 2-colour-LIF, however, the reference signal was weak so that multiple laser-pulses were needed to illuminate a single image. Thus, the temporal resolution was strongly limited.

Investigation of dye combinations for 2-colour-LIF

As mentioned before, the dye combination most commonly used for 2-colour-LIF measurements in water is Rhodamine B (RhB) and Rhodamine 110 (Rh110). Only very few works can be found in literature that deal with the investigation of other dyes regarding their applicability for temperature measurements. Coppeta and Rogers performed an extensive study about the fluorescence behavior of nine different water-soluble dyes and their suitability for 2-colour-LIF applications. Further investigations on the temperature-sensitivity of selected dyes in water and ethanol were conducted in [50]. Wolff et al. [93] and Depredurand et al. [19] analyzed Pyrromethene 597-8C9 (PM597-8C9), a dye soluble in non-polar solvents (alkanes), regarding its applicability for 1-dye-2-colour-LIF measurements.

2.2.2 Temperature sensitive paints

Temperature sensitive paints (TSPs) are used for temperature measurements on surfaces. Basically, a TSP consists of a temperature-sensitive luminescent (fluorescent or phosphorescent) dye that is incorporated in an appropriate polymer binder material.

Typical luminescent dyes employed in TSPs are RhB [58](also used for LIF measurements), perylene and pyronine. Besides these organic dyes, complexes of rare earth ions with big organic molecules as ligands, such as EuTTA[1] and Ru(bpy)[2] can be counted among the TSPs. The commonly used TSPs altogether cover a measurable temperature range from -150 °C to $+150$ °C. The applications of TSPs are usually 2-dimensional temperature measurements on model surfaces in the macroscopic scale. Characteristic examples are heat transfer measurements on surfaces that are exposed to a laminar or turbulent gas flow (e.g. wind tunnel experiments). Two physical principles are used for the evaluation of temperatures. Analogously to the LIF method described above, the fluorescent intensity is a function of temperature and can be measured by an detector array (e.g. CCD-camera). The ratio-metric (2-colour-LIF) approach is also used for TSPs by adding a reference dye and detecting its signal separately [4]. Besides that, the luminescent decay time is also a function of temperature for many dyes. For fluorescent molecules, this decay time is typically in the range of some nanoseconds (10^{-9} s) and therefore not measurable with cameras. However, if the decay time is long enough or if high frequency single point measurements with a photomultiplier tube are performed, this decay time can be used to accurately determine the temperature [97]. The major advantage of this time-resolved approach, is its robustness against fluctuating factors such as the excitation energy.

An extensive description of the principles, the applications and measurement methods using TSPs can be found in [45]. If the corresponding dyes are incorporated in solid, spherical polymer-particles instead of polymer-films, TSPs can potentially be used as particle-based sensors for temperature fields in fluids. One suitable dye is EuTTA, which has also been used in some measurements presented in this thesis.

[1] Europium thenoyltrifluoroacetonate
[2] Tris(bipyridine)ruthenium

Application of EuTTA as temperature sensitive dye

According to Khalil et al. [31], the observed luminescent emission of EuTTA corresponds to the transition of the Eu^{3+}-ion from $^5D_0 \rightarrow {}^7F_2$. These states have different multiplicities and are thus spin-forbidden processes. Hence, the observed emission is generally called phosphorescence and exhibits a rather long decay time. Moreover, the decay time depends on the temperature making EuTTA a suitable indicator for decay-time based temperature measurements. Someya et al. [73] measured the decay time of particles dyed with EuTTA for different temperatures and extended this technique to measure temperature fields by means of a double imaging CCD-camera. The measurements are described in more detail in section 2.4.

Basu and Venkatraman [4], on the contrary, used the time-integrated, ratio-metric approach. In their experiments they embedded EuTTA as temperature sensitive dye and Perylene as reference dye into a film of polystyrene. Both dyes were excited in the UV-range (330 nm to 380 nm) using a Xenon-arc lamp. They observed a dependency of the temperature-sensitivity on the type of polymer (dope, polystyrene, PMMA) in which the dyes were incorporated. The highest temperature-sensitivity of -1.80 %/K was found for 2 mg EuTTA and 1 mg perylene, embedded in 500 mg of polystyrene at temperatures ranging from 5 °C to 50 °C. Due to the large shift between the emission peaks of perylene ($\approx$ 450 nm) and EuTTA ($\approx$ 615 nm) the signals can easily be separated, which makes these dyes very suitable for ratio-metric temperature measurements.

2.2.3 Thermographic phosphors

Unlike TSPs, thermographic phosphors are ceramic materials that are doped with rare earths. Their luminescence results from excitation and subsequent radiative deactivation of rare earth ions and is therefore very similar to that of EuTTA. A distinctive difference, however, is their applicable temperature range. Since they are ceramic materials, most thermographic phosphors can withstand very high temperature and are therefore often used in high-temperature applications. Since the decay time of some phosphors is also very long (millisecond range), temperature measurements based on the determination of the decay time are commonly used. Though, an intensity-based ratio-metric approach exists as well. The excitation of thermographic phosphors requires UV-light (for most cases) that is often provided by a pulsed laser (necessary for measurements of decay time) or an arc lamp with appropriate filters.

Brübach et al. [9] used the thermographic phosphor $Mg_4GeO_{5.5}F$:Mn excited with the third harmonic of a Nd:YAG-laser (355 nm), to measure the temperature field in a spray of n-dodecane. The phosphors are available in form of powder with a particle size distribution ranging from approximately 0.2 µm to 30 µm. Hence, the liquid can easily be seeded with this powder. Anologously to the 1-dye-2-colour-LIF method, two bands in the emission spectrum of this phosphor were used as temperature-sensitive and reference signal respectively. The signals were detected using a single intensified CCD-camera in combination with an image doubler. The image doubler splits the detection array of the camera in two halves and uses optical filters to project the reference signal on one half and the sensitive signal on the other half. The temperature range of these measurements was 23 °C to 170 °C.

Measurements of 2-dimensional surface temperatures resolving the decay time of the same thermographic phosphor ($Mg_4GeO_{5.5}F$:Mn) have been performed by Omrane et al. [54]. The phosphorescence signal was detected by eight consecutively gated CCD arrays. Thus, each decay curve can be resolved with eight time-points and the decay time was evaluated by an exponential fit through these points. In this way, the decay time was determined for each pixel of the image. Kissel [33] used a CMOS-high-speed camera instead so that he was able to temporally resolve the decay time of the thermographic phosphor. In order to reach the required frame-rate of 150 kHz, he had to reduce the number of active camera pixels which strongly limited the spatial resolution.

Extensive reviews on the theory and the applications of thermographic phosphors can be found in [2] and [30].

2.2.4 Thermochromic liquid crystals (TLCs)

Thermochromic liquid crystals (TLCs) are the most common optical temperature measurement method. This technique is based on the selective, temperature-dependent reflection of white light by liquid crystals. A change of their colour from red to blue can be observed when they are heated up. Various TLC-formulations exist, each of them having a specific active temperature range in which this colour-play occurs. TLCs can be used in two different forms, either as a pure substance that can be painted on a surface, or in microencapsulated form so that a small droplet of TLCs is surrounded by a capsule that protects it from environmental conditions. The latter ones can be used in liquids for simultaneous measurement of temperature and velocity. The temperature can be derived from the colour of the TLC particles in the images acquired by a colour-camera and the velocity is determined from the particle movement by means of the PIV technique. The big advantage of TLCs are the minor requirements for the measurement equipment. Only a single camera (colour-camera) is needed and there is no need for monochromatic (laser) illumination.

Nevertheless, due to several drawbacks such as the need for white-light illumination, TLCs are not applicable for spatially and temporally highly resolved measurements. At the author's institute, a detailed investigation has been performed on TLC measurements which can be found in [50].

TLCs are used in various applications and numerous publications on this topic exist. A review on TLCs used for simultaneous measurement of temperature and velocity in fluids can be found in [18].

2.3 Optical method for velocity measurements, Particle image velocimetry (PIV)

Measurement principle

The Particle Image Velocimetry is based on the measurement of particle displacement Δx in a short time step Δt, so that the velocity u can be determined by:

$$u = \Delta x / \Delta t$$

As the name indicates, the observed fluid must be seeded with tracer particles that can either just scatter the exciting light (no wavelength-shift between excitation and emission) or show fluorescence upon proper excitation. Usually, laser light sheets are used to illuminate the seeded flow and digital cameras (optical axis perpendicular to the light sheet) are used to detect the signal.

To measure high velocities on small spatial scales, very short exposure times are needed. This is realized by pulsed lasers that illuminate the field of view for a very short time (10 ns to 100 ns) so that even at very high flow velocities, the exposure time is so short that the particles are imaged as dots and not as streaks on the camera images. Additionally, these lasers are able to fire two laser pulses with a predefined temporal separation Δt (double cavity laser), illuminating the particles at two time points. Depending on the camera type used, either one image is illuminated by both pulses (double-exposure images) or two images are taken, of which each is illuminated by one pulse. The latter method requires a special camera for PIV purposes that can take two images within a very short time interval. The principle of PIV measurement and data processing is sketched in Figure 2.6.

Data and image processing

Image processing of the acquired particle images is necessary to calculate the particles' displacement Δx. Therefore, the images are subdivided into interrogation windows and for each of them one displacement vector is evaluated. The size of the interrogation windows depends mainly on the seeding density and

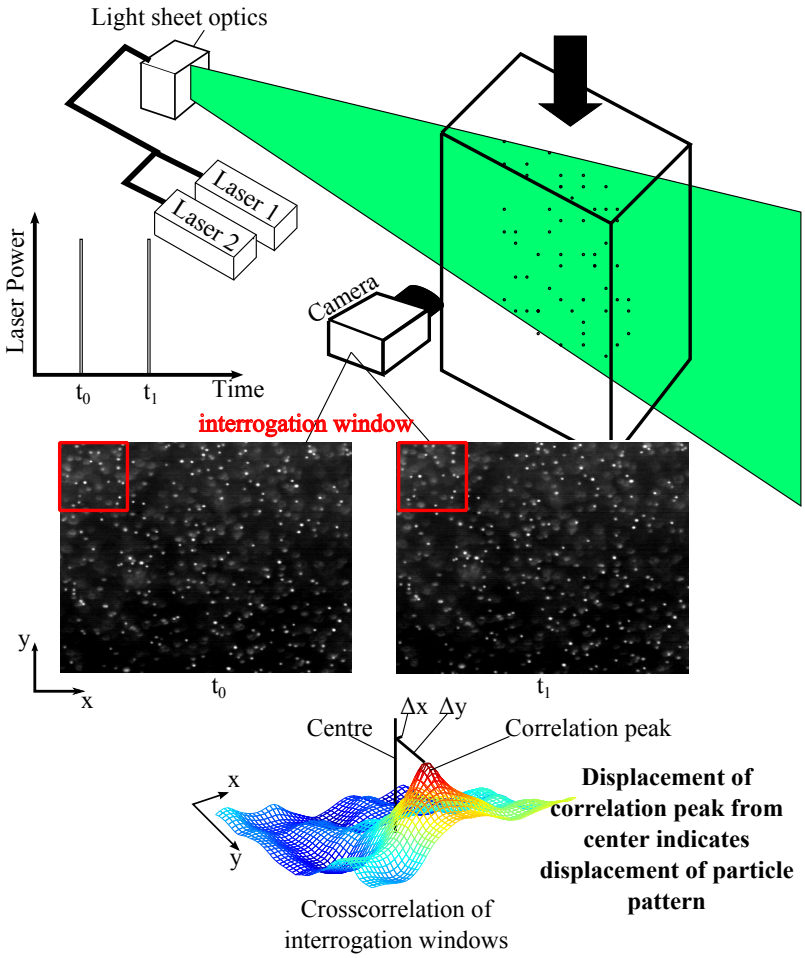

Figure 2.6: Schematic of the PIV principle. Two particle images taken in a small interval are subdivided into interrogation windows. These windows are compared by means of a cross-correlation and the particle displacement is evaluated from the displacement of the correlation peak from the centre.

must be chosen such that a considerable number of particles is involved. The evaluation of the displacement vectors is performed by cross-correlating each interrogation window of the image illuminated by the first laser pulse with the respective interrogation window of the image illuminated by the second laser pulse. Cross-correlation of digital particle images is commonly performed using following equation according to Westerweel [90] where X represents the resulting cross-correlation matrix of an $M \times N$ pixel interrogation window W_1 of the image at time t_0 and the corresponding interrogation window W_2 at t_1 for a spatial separation s, z.

$$X(s,z) = \frac{1}{MN} \sum_{m=1}^{M} \sum_{n=1}^{N} W_1(m,n) \cdot W_2(m-s, n-z) \tag{2.11}$$

In case that double-exposure images are used, an auto-correlation for each interrogation window is carried out. The maximum of the correlation matrix indicates the maximum accordance between the cross-correlated interrogation windows and thus the displacement vector results from the shift of the respective correlation peak from the center of the correlation matrix. Sub-pixel accuracy is achieved by an interpolation of the correlation peak (most commonly a 3 or 5 point gaussian or a parabolic fit is used).

Several approaches like correlation averaging, window shifting, multigrid analysis and iterative window deformation can be used to increase the accuracy of the PIV technique and enhance spatial resolution. These techniques, as well as other details about the PIV-method, are described in [81].

Applications and developments of PIV

With the development of affordable digital cameras, lasers and computers for data processing, PIV has evolved from its introduction in 1984 to a commercial off-the-shelf product that is used in a variety of applications. A comprehensive review of PIV applications and methods is given by Adrian in [1]. In recent developments, PIV was extended to a stereoscopic method [71] (which facilitates measurement of the third velocity component in the image plane). Real three-dimensional methods exist as well, such as defocussing PIV [55] and holographic PIV [68].

Micro Particle Image Velocimetry (μ-PIV)

The application of PIV on very small length scales (field of view has a size smaller than 1×1 mm^2) makes special demands on the measurement technique and thus it is often treated as a separate discipline. Illumination with a light sheet is not applicable for μ-PIV due to limited optical access and volume illumination has to be used. For that reason, also out-of-focus particles are illuminated which can superimpose the signal from in-focus particles resulting in erroneous measurements. To reduce the so-called depth of correlation (range along the optical axis for which out-of-focus particles contribute significantly to the particle image), objectives with high numerical aperture are required.

For μ-PIV applications, the use of fluorescent tracer particles is requisite in order to separate the particles' signal from exciting light that is scattered at solid boundaries. The particles' size must be chosen carefully taking into account many factors, like the magnification, the numerical aperture of optical setup and the required accuracy. The image processing is also more complex in μ-PIV applications due to a reduced seeding density and the applied volume illumination.

A very detailed description of the theory for μ-PIV can be found in [89]. Typical fields of application for μ-PIV are micro-fluidic devices [6], [27], [69] and biological systems [78], [84].

2.4 Luminescence-based methods for temperature and velocity field measurements

2.4.1 LIF with added PIV tracer particles

Several methods for simultaneous velocity and temperature measurements that are based on temperature dependent luminescence already exist. The most common one is the combination of LIF and PIV by just adding tracer particles to the dye solution. This approach has been applied by Hishida and Sakakibara [26], [62] for 2-dimensional measurements of a thermal stratified flow and a plane impinging jet. The signal from the dye solution (1-colour-LIF) was imaged on one camera, while a second camera captured the light scattered by the PIV tracer-particles.

Funatani et al. [22] extended this technique to 2-colour-LIF measurements with added PIV tracer particles. Instead of separate monochrome CCD-cameras they used a colour 3-CCD-camera[3], detecting the sensitive signal with the red-image, the reference signal with the green image and the light scattered from the particles with the blue image. They observed a decrease in temperature sensitivity with an increasing number of particles seeded to the flow. Consequently, there is a trade off between the accuracy of the temperature measurements and the accuracy of the velocity measurements.

2.4.2 Measurements resolving luminescent decay times of EuTTA dyed particles

Very recently Someya et al. [73] presented a 2-dimensional temperature and velocity measurement method based on the phophorescence decay time of particles dyed with EuTTA. The particles were prepared by adding a solution of EuTTA in ethanol to hollow, porous spherical SiO_2 particles (standard PIV particles) and sintering them under rather low temperature conditions. These temperature sensitive particles were illuminated by a pulsed, frequency tripled Nd:YAG-laser (355 nm) and the measured (point-wise measurement with photodiode) phosphorescence decay time ranged from 100 µs to 600 µs for temperatures ranging from 20 °C to 100 °C. In the next step, two-dimensional measurements were performed, by adding the particles to an oil-filled tank that was heated from the top and taking particle images with an interline transfer camera[4]. From the intensity ratio of the subsequent images in a short interval, the decay time of the phosphorescence was evaluated. A requisite for the measurement of the decay time is that the particles show no recognizable displacement between the two images. For that reason, these subsequent images cannot be used for the velocity determination by means of PIV. Thus, images illuminated by two subsequent laser pulses (10 Hz pulse rate) are used for PIV.

They further developed this measurement method [72] by replacing the interline CCD camera with a high-speed CMOS-camera, operating at a frame rate of 15 kHz. With this setup they were able to resolve the phosphorescence decay time with six instead of two images. They applied this technique to the natural convection in a cell with a free surface (driven by Marangoni convection and buoyancy forces). The spatial resolution for the determination of temperature was 0.3×0.3 mm^2 and the accuracy was estimated to be ± 0.4 K. This method requires a high-speed camera operating at very high frame-rates. Moreover, the acquisition time for one sequence is very limited, due to the high quantity of images that need to be stored on the limited internal memory of the camera.

[3] A colour 3-CCD-camera contains three single CCD-chips for red, green and blue. Thus each pixel in the image consists of a red, green and blue part.

[4] Normally used for PIV. This camera can take two images in a very short interval. However, the framerate of this camera is not higher as for conventional CCD-cameras.

3 Experiments

3.1 Microencapsulated fluorescent dyes for temperature measurement

In the next section, the development of the novel temperature measurement technique based on the microencapsulation of temperature sensitive fluorescent dyes is presented. Furthermore, the experimental setups and procedures for the investigation of these microcapsules with regard to their applicability for temperature and velocity measurements are described.

3.1.1 Development of the temperature sensitive microcapsules

Microcapsules are composed of a liquid core that is surrounded by a solid shell. Thus, the fluorescence characteristics of one dye in a specific solvent are preserved, while the microcapsule shows the mechanical behavior of a solid particle. As explained in section 2.1.7, the fluorescence properties, especially the dependency on temperature, is strongly affected by the dye's environment. This is the reason for the unpredictable behavior of fluorescent dyes when they are incorporated in different polymers, as it is shown in section 5.2.1. Microencapsulation overcomes this problem, because the environment of the dye is not altered, while it is "transformed into a solid".

Spectral characteristic of the core solution

From the microencapsulation process and the wavelength of the available laser, the following specifications for the temperature-sensitive dye (combination of dyes) arise:

- Solubility in nonpolar solvents,
- No solubility in polar solvents,
- Fluorescent absorption at 532 nm,
- Wavelength dependent temperature sensitivity.

The dye must not be soluble in polar solvents to prevent diffusion of the dye through the thin capsule shell when the microcapsules are dispersed in water. As explained in section 2.2.1, a wavelength dependent temperature sensitivity is prerequisite for the application of a 2-colour-LIF method. In reality the idealized dye combination shown in Figure 2.5 does not exist. For that reason, additional effects that will influence the accuracy of the measurement technique, must be considered during the selection of dyes and the specification of their proper concentration in the mixture. Wolff et al. [93] introduced Pyrromethene 597-8C9 (PM597-8C9)[1] as a temperature-sensitive dye soluble in alkanes. They used this dye to measure the temperature of diesel droplets during high pressure injection into a hot air chamber by means of an 1-dye-2-colour-LIF technique. To be more precise, they used two spectral bands of PM597-8C9 exhibiting different dependencies on temperature. Depredurand et al. [19] intensely investigated the suitability of PM597-8C9 as temperature-sensitive tracer for the investigation of droplets formed from different types of fuels (ethanol, 3-pentanone, dodecane). Both authors used an argon-ion laser (514 nm) for excitation.

[1] provided by Exciton, Dayton Ohio

However, spectral investigations performed in this work did not reveal a wavelength dependent temperature sensitivity of PM597-8C9 in Hexadecane (see Figure 3.1), as it is reported by the above mentioned authors for PM597-8C9 in other solvents. This is probably attributed to the longer excitation wavelength used in present studies. A temperature sensitivity of $\mathrm{d}I/\mathrm{d}T \approx -1.5$ %/K, which is almost constant for the entire wavelength range can be observed for the PM597-8C9 dye.

The temperature sensitivity presented here has been calculated from a linear fit of the intensity over temperature for all wavelengths.

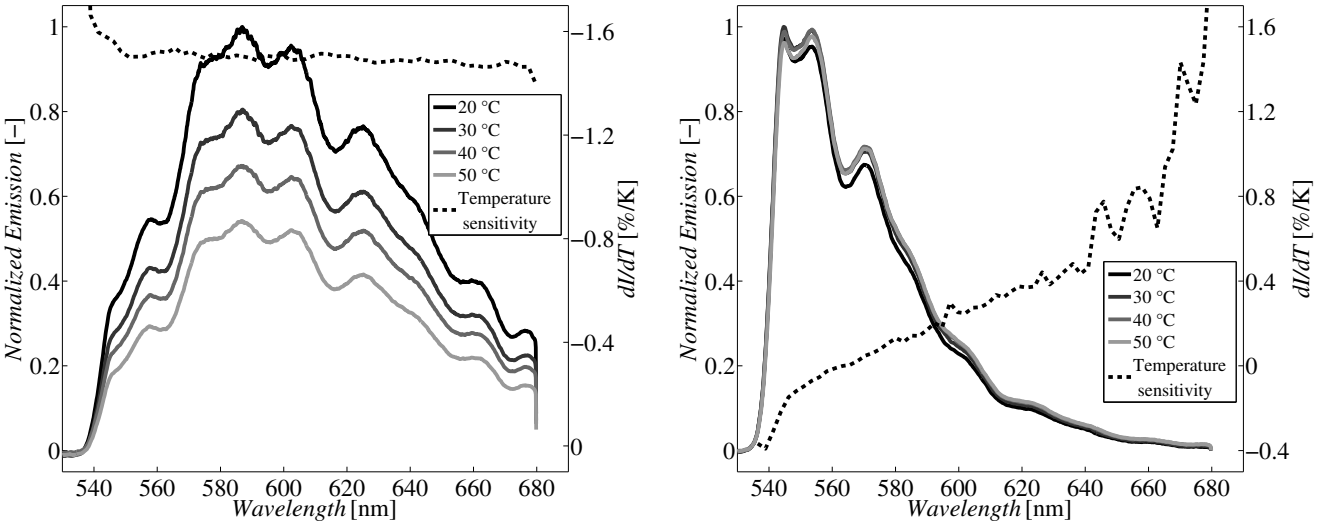

Figure 3.1: Spectra for the temperature sensitive dye PM597-8C9 (a) and the reference dye PM567 (b) recorded at different temperatures. Additionally the temperature sensitivity ($\mathrm{d}I/\mathrm{d}T$) over the wavelength is plotted. Temperature sensitivity is calculated for each wavelength as a linear fit of the plotted normalized emission over temperature. Outliers of temperature sensitivity at the left and right ends of the observed spectral region are due to poor signal-to-noise ratio.

On the contrary, PM567 shows no significant temperature sensitivity at the maximum emission wavelength, but slightly increases to a value of $\mathrm{d}I/\mathrm{d}T \approx 0.4$ %/K at a wavelength of 640 nm. Since the signal is comparatively small at this wavelength, the temperature sensitivity evaluation is very uncertain there.

From Figure 3.1 it can be concluded that a mixture of the PM567 (as the reference dye) and PM597-8C9 (as the temperature-sensitive dye) exhibits the demanded characteristics for temperature measurements by the 2-colour-LIF method. Assuming that the interaction of both dyes (e.g. by self-absorption, section 2.1.9) is negligible, the emission spectrum of the dye mixture can be modeled by the linear accumulation of the single dyes' emission spectra. The spectra of both dyes show different peak emissions, but no regions where either of them exhibits zero fluorescence emission. Thus, a temperature dependent ratio R according to equation 2.9 is expressed as:

$$R(T) = \frac{\int_{\lambda_1}^{\lambda_2} I_{\mathrm{PM567}}(\lambda)\,\mathrm{d}\lambda + \int_{\lambda_1}^{\lambda_2} I_{\mathrm{PM597-8C9}}(\lambda, T)\,\mathrm{d}\lambda}{\int_{\lambda_3}^{\lambda_4} I_{\mathrm{PM567}}(\lambda)\,\mathrm{d}\lambda + \int_{\lambda_3}^{\lambda_4} I_{\mathrm{PM597-8C9}}(\lambda, T)\,\mathrm{d}\lambda} \tag{3.1}$$

where λ_1, λ_2 are the limits for the reference part of the spectrum and λ_3, λ_4 include the temperature sensitive part respectively. If either of the two dyes dominates the fluorescent emission,

$$I_{\mathrm{PM567}} >> I_{\mathrm{PM597-8C9}}, \qquad I_{\mathrm{PM567}} << I_{\mathrm{PM597-8C9}}$$

$R(T)$ tends to

$$\frac{\int_{\lambda_1}^{\lambda_2} I_{\mathrm{PM567}}(\lambda)\,\mathrm{d}\lambda}{\int_{\lambda_3}^{\lambda_4} I_{\mathrm{PM567}}(\lambda)\,\mathrm{d}\lambda}, \qquad \frac{\int_{\lambda_1}^{\lambda_2} I_{\mathrm{PM597-8C9}}(\lambda)\,\mathrm{d}\lambda}{\int_{\lambda_3}^{\lambda_4} I_{\mathrm{PM597-8C9}}(\lambda)\,\mathrm{d}\lambda}$$

For both cases the temperature sensitivity of the ratio $\mathrm{d}R/\mathrm{d}T$ becomes very small, because $\mathrm{d}I_{\mathrm{PM597-8C9}}/\mathrm{d}T$ is constant for the observed wavelength ranges and $\mathrm{d}I_{\mathrm{PM567}}/\mathrm{d}T$ is marginal.

As the fluorescence emission is a function of the dye concentration, the temperature sensitivity of a dye mixture will also depend on the proportion of the concentrations of both dyes $C_{\mathrm{PM567}}/C_{\mathrm{PM597-8C9}}$. Consequently, it must be chosen carefully to enhance the temperature sensitivity and therefore the accuracy of the method.

To find the optimum ratio of dye concentrations ($C_{\mathrm{PM567}}/C_{\mathrm{PM597-8C9}}$) with maximum temperature sensitivity, a factor c_1 (see equation 3.2) is introduced and multiplied with $I_{\mathrm{PM567}}(\lambda)$ to represent a variation of the dye concentration C_{PM567}. According to equation 3.1, $\Delta R/\Delta T$ is then calculated using following equation

$$\frac{\Delta R}{\Delta T} = \frac{\dfrac{\int_{\lambda_1}^{\lambda_2} c_1 \cdot I_{\mathrm{PM567}}(\lambda,T_1)\,\mathrm{d}\lambda + \int_{\lambda_1}^{\lambda_2} I_{\mathrm{PM597-8C9}}(\lambda,T_1)\,\mathrm{d}\lambda}{\int_{\lambda_3}^{\lambda_4} c_1 \cdot I_{\mathrm{PM567}}(\lambda,T_1)\,\mathrm{d}\lambda + \int_{\lambda_3}^{\lambda_4} I_{\mathrm{PM597-8C9}}(\lambda,T_1)\,\mathrm{d}\lambda} - \dfrac{\int_{\lambda_1}^{\lambda_2} c_1 \cdot I_{\mathrm{PM567}}(\lambda,T_2)\,\mathrm{d}\lambda + \int_{\lambda_1}^{\lambda_2} I_{\mathrm{PM597-8C9}}(\lambda,T_2)\,\mathrm{d}\lambda}{\int_{\lambda_3}^{\lambda_4} c_1 \cdot I_{\mathrm{PM567}}(\lambda,T_2)\,\mathrm{d}\lambda + \int_{\lambda_3}^{\lambda_4} I_{\mathrm{PM597-8C9}}(\lambda,T_2)\,\mathrm{d}\lambda}}{T_2 - T_1} \tag{3.2}$$

with $I_{\mathrm{PM567}}(\lambda, T)$ and $I_{\mathrm{PM597-8C9}}(\lambda, T)$ taken from the measured values presented in Figure 3.1 and the regions of the spectrum being $\lambda_1 = 550$ nm, $\lambda_2 = 560$ nm , $\lambda_3 = 630$ nm and $\lambda_4 = 640$ nm. In Figure 3.2 the temperature sensitivity calculated from $\frac{\Delta R}{R_{\max} \cdot \Delta T}$ is plotted over c_1.

Taking into account the excitation intensity and the dyes' concentration at the measurement of the spectra in Figure 3.1, the optimum value of $C_{\mathrm{PM567}}/C_{\mathrm{PM597-8C9}}$ is calculated from $c_1 = 1.5$ to be 0.36. The absolute concentrations of C_{PM567} and $C_{\mathrm{PM597-8C9}}$ are defined to be 176 mg/l and 483 mg/l, respectively. On the one hand, the absolute concentration should be as high as possible to enhance the fluorescence signal intensity. On the other hand, the concentration should be significantly below the solubility limit and it must be checked that no concentration quenching occurs. In present work the solubility limit was not reached, even for concentrations three times higher than the actually chosen ones. Experimental investigations did not reveal concentration quenching.

In Figure 3.3 the temperature dependent spectra (a) of a solution containing 176 mg/l of the dye PM567 and 483 mg/l of PM597-8C9 in hexadecane. The spectra exhibit domains with different temperature sensitivities as it was estimated from the spectra of the single dyes. From the marked regions in (a) the ratio R is calculated according to

$$R = \frac{\int_{550nm}^{560nm} I_{\mathrm{Mixture}}(\lambda)\,\mathrm{d}\lambda}{\int_{630nm}^{640nm} I_{\mathrm{Mixture}}(\lambda)\,\mathrm{d}\lambda} \tag{3.3}$$

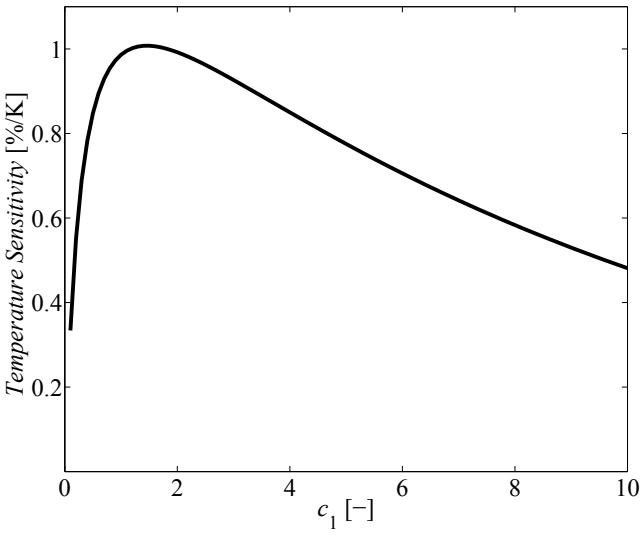

Figure 3.2: Temperature sensitivity plotted over c_1. Temperature sensitivity is calculated from $\frac{\Delta R}{R_{\max} \cdot \Delta T}$, with ΔR calculated from the spectra of the single dyes at different temperatures (Figure 3.1) according to equation 3.2. The spectrum of PM657 is weighted with the variable c_1, to model the influence of different proportions of dye concentrations $C_{\mathrm{PM567}}/C_{\mathrm{PM597-8C9}}$.

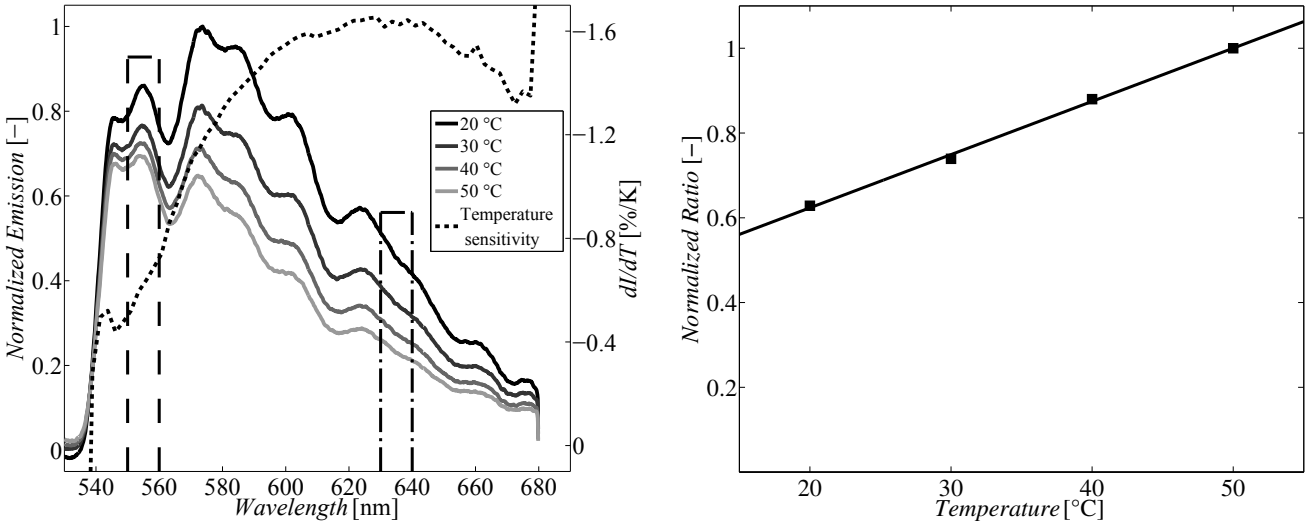

Figure 3.3: Temperature dependent spectra of a solution of 176 mg/l PM567 and 483 mg/l PM597-8C9 in hexadecane (a). The temperature sensitivity is calculated from a linear fit of the fluorescent emission over temperature at each wavelength. Fluorescent emission in regions marked in (a) is used to calculate the ratio according to equation 3.3 in (b) at each temperature measured.

normalized by its maximum value and plotted for each temperature step in (b). A linear increase of approximately 1.2 %/K can be derived from the data points. Thus, the temperature sensitivity is even higher than it was calculated from the spectra of the single dyes at an optimum proportion of the dyes' concentration (Figure 3.2). The wavelength dependent temperature sensitivity (Figure 3.3 (a)) is also slightly higher than the one for PM 597-8C9 presented in Figure 3.1 (a).

The measured spectra of PM567 and PM597-8C9 dissolved in hexadecane and the resulting temperature sensitivity confirm that the selected dye mixture, with a specific proportion of the dyes' concentrations, meets the requirements for the 2-colour-LIF method very well. Hence, also the approach used to calculate the optimum concentration proportion from the single dyes' spectra is approved for this case.

Microencapsulation process

In medical applications, microencapsulation is a common technique to transport drugs in the liquid core of the microcapsules and enable controlled release at a specific position by shell rupture. Other examples for the application of this process is the incorporation of oil-soluble flavors in food products and carbonless copy paper which uses ink-filled microcapsules that break up when appropriate pressure is applied.

Microencapsulation by coacervation can be described as a process involving two main steps. First, the liquid that should be encapsulated is emulsified in a carrier liquid. Consequently, both liquids must be immiscible (polar/nonpolar liquids, e.g. oil and water). In the next step, a solid shell is formed around the small droplets. This can be realized by precipitation of a polymer that has been previously dissolved in the carrier liquid or by polymerization of a monomer that has been added to the carrier liquid. Both processes induce an agglomeration of polymer molecules at the droplet boundaries, forming a solid polymer shell. The principle of microencapsulation with precipitation of a polymer is also illustrated in Figure 3.4.

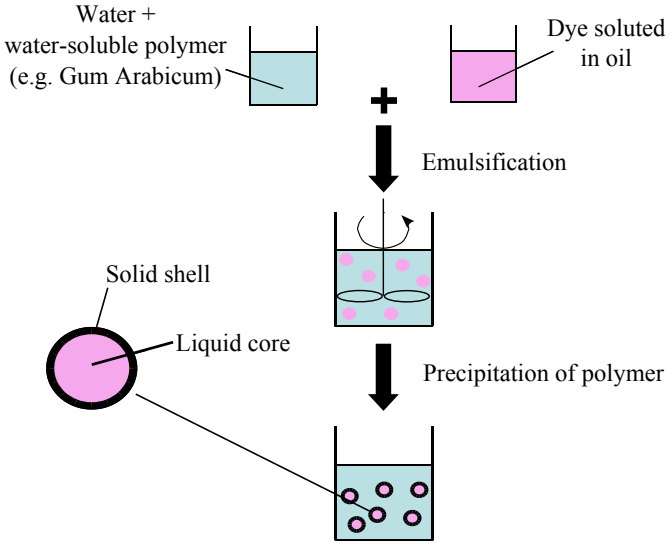

Figure 3.4: Principle of the microencapsulation technique by coacervation

There are different methods for the emulsification, for example stirring of the carrier liquid, as shown in Figure 3.4. But for this technique, the microcapsules' size shows a broad distribution and is strongly depending on the agitation speed [7]. The microcapsules presented here were produced by *Nanomi B.V.* using a technique in which the droplets of the core solution are formed by extruding through the holes of a micro-sieve. Thus, a narrow particle size distribution can be guaranteed. Polymethylmethacrylate

(PMMA) is chosen as shell material, because it exhibits a very good chemical resistance against the core material (hexadecane), little aging and comparatively high temperature resistance.

Besides the described method of microencapsulation by coacervation, there are further alternatives such as extrusion through a double nozzle. One nozzle is fed by the core solution and the other one by the shell material in liquid phase. Ultrasonic excitation leads to the formation of droplets with the core solution as the inner phase, surrounded by the liquid polymer. After solidification of the polymer, by air drying for instance, microcapsules with a solid shell are formed [80]. Detailed information about further microencapsulation techniques can be found in [5], [94], [95].

Spectral characteristics of fabricated microcapsules

The spectra presented in Figure 3.5 are measured from a dispersion of the fabricated microcapsules in water.

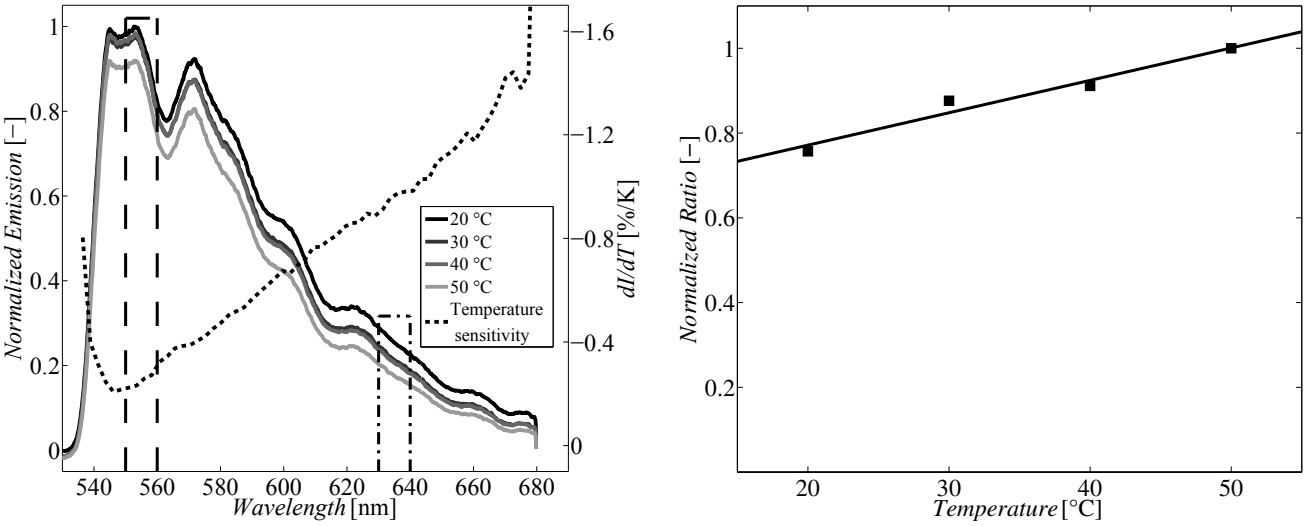

(a) (b)

Figure 3.5: Spectra for a dispersion of the fabricated microcapsules in water (a). The overall emission shows variations that are likely due to an inhomogeneity of the particles' distribution in the carrying liquid. Thus, the temperature sensitivity is hard to recognize looking at the spectra only. However, a calculation of the temperature sensitivity analogously to that in Figure 3.3 is shown in (a). The ratio of intensities in the marked region is plotted over temperature in (b).

A systematic dependency on the temperature cannot be recognized by visual inspection for these spectra. This is due to the alteration in the overall emission intensity. As this is again influenced by the number of illuminated particles in the measurement volume, these fluctuations can mainly be attributed to an inhomogeneous distribution of the particles in the dispersion. Nevertheless, the temperature sensitivity can be derived from these spectra using the same approach as for the spectra in Figure 3.3 and the result is plotted in Figure 3.5 (a).

The ratio is again calculated from the marked regions and plotted over temperature in Figure 3.5 (b). The temperature-dependent increase of the microcapsules' ratio is only 0.76 %/K and therefore significantly smaller than for the ratio of the unencapsulated solution showing a temperature sensitivity of 1.2 %/K (see Figure 3.3 (b)).

Also the emission spectra of the microcapsules differ from the emission spectra of the core solution. In Figure 3.3 the spectrum at 20 °C shows a maximum that can be attributed to the emission of PM597-8C9

(≈ 570 nm), while in Figure 3.5, the maximum emission at 20 °C can be found for shorter wavelengths, corresponding to the emission of PM567.

This finding can be explained by the influence of self-absorption and re-emission phenomena on the ratio (see section 2.1.9). These effects have not been taken into account when the optimal concentration of both dyes in the core solution has been evaluated. The core solution was in a container with a side length of 10 mm during the measurements, resulting in a path length for self-absorption of approximately 5 mm. On the contrary, the path length of approximately 5 µm for the microcapsules is defined by their diameter. The absorption spectrum of both dyes in hexadecane reveals a relatively high absorption around 550 nm and reduced absorption for wavelengths longer than 570 nm (see Figure 5.21). Consequently, such a significant reduction of the path length causes the altered emission characteristic of the microcapsules compared to that of the core solution in the test cell.

In summary, it can be said that the temperature sensitivity of the fabricated microcapsules is not as high as it was estimated from the spectra of the core solution. Thus, the temperature sensitivity can still be enhanced by fabrication of new microcapsules with adapted dye concentrations in the core solution.

Thermal response time of the developed microcapsules

The temporal resolution that can be achieved independently from the measurement devices is determined by the time that passes between the alteration of the measurand and the corresponding change in the signal. For temperature measurements by means of fluorescent emission, this time is governed by the time the fluorescent solution needs to heat up or cool down, as the fluorescence itself happens within some nanoseconds. To evaluate the time a microcapsule needs to adapt to the temperature of the surrounding fluid, the Fourier number is calculated according to [83]

$$Fo = \frac{t\ a}{r^2} \tag{3.4}$$

with the thermal diffusivity

$$a = \frac{\kappa}{\rho\ c_p} \tag{3.5}$$

where κ represents the thermal conductivity, ρ the density and c_p the specific heat capacity. The microcapsules consist of PMMA as shell material and a hexadecane solution in the core. For a conservative estimation, only the lower thermal diffusivity of both substances is used for the entire capsule. The thermal diffusivity for PMMA is $a_{\mathrm{PMMA}} = 1.29 \times 10^{-7}\ \mathrm{m^2/s}$ and $a_{\mathrm{Hexadecane}} = 1.06 \times 10^{-7}\ \mathrm{m^2/s}$. Thus, $a_{\mathrm{Hexadecane}}$ is chosen and t is set to 1 ms, corresponding to the maximum acquisition rate of the optical setup. The mean diameter of the microcapsule is 8.9 µm, resulting in a radius r of 4.5 µm. With these data, the Fourier number is evaluated to be $Fo = 4.3$.

From the solution of the unsteady heat conduction for a sphere[2], it can be seen that the dimensionless temperature Θ_m[3] tends to zero for $Fo > 2.5$ and $Bi \geq 1$. The Biot-number Bi is a dimensionless number describing the ratio of heat conductance inside the sphere and heat transfer to/from the surrounding. For the case of the microcapsules it is assumed that the temperature in immediate vicinity of the capsule wall is to be measured. Thus, the heat transfer resistance is negligible and $Bi \geq 1$ is a valid assumption.

Accordingly, it can be stated that the microcapsules adapt to the surrounding temperature within less than 1 ms, which corresponds to the maximum acquisition rate of the setup used. Hence, the thermal response time of the microcapsules is not the limiting factor for the temporal resolution in temperature measurements.

[2] Figure 10, page Ec8 in [83]

[3] Describes the temperature difference between centre of the sphere and the far field temperature

Buoyancy of microcapsules

If the specific density of the microcapsules differs significantly from the density of the surrounding liquid, this leads to a separation of the capsules from the carrier medium due to buoyancy forces. The sinking/ascending velocity u_{sinking} can be calculated following Stokes' equation [38]

$$u_{\text{sinking}} = \frac{d_{\text{capsule}}^2 g}{18\nu} \left(\frac{\rho_{\text{capsule}}}{\rho_{\text{medium}}} - 1 \right) \tag{3.6}$$

with the microcapsules diameter d_{capsule}, the gravitational acceleration g and the kinematic viscosity ν of the carrier medium. As the ratio of the specific densities $\rho_{\text{capsule}}/\rho_{\text{medium}}$ has a great influence on the sinking velocity, this value should preferably be close to 1. Microcapsules consist of different materials in the shell and the core, so the mean specific density of the microcapsules can be controlled by the core-to-shell ratio. The core material is hexadecane with $\rho_{\text{Hexadecane}} = 775$ kg/m^3 and the shell is made of PMMA with $\rho_{\text{PMMA}} = 1170$ kg/m^3. Accordingly, the core-to-shell ratio is chosen to be 1:2, resulting in $\rho_{\text{capsule}} = 1038$ kg/m^3, which is close to that of water. With an average diameter of 8.9 µm and water as the surrounding medium the sinking velocity is 2.3 µm/s.

For the measurements presented in this thesis, the minimal acquisition rate is 30 fps. In this time, the maximum displacement of the particles due to buoyancy effects is 76 nm which is a negligible contribution to the overall particle displacement caused by the observed flow.

Nevertheless, on a longer time-scale of some hours, which is the typical time needed to perform the calibration and the actual measurements, buoyancy is an important factor. It leads to separation of the microcapsules from the fluid and consequently to a change in the seeding density, which again influences the measurement accuracy. Hence, depending on the application, it might be necessary to stabilize the dispersion, by stirring or creating a flow countering the gravitational force. It becomes clear from equation 3.6 that the particles' diameter influences the sinking velocity as well.

Particles' size distribution

The size distribution of the microcapsules is shown in Figure 3.6. This data is provided by the particles' manufacturer. The microcapsules' diameter is almost normally distributed and the lower and upper limit of the 90 %-interval (90 % of all particles show a size that is located within this interval) are marked as blue lines. As mentioned above, the manufacturer of the microcapsules achieves this narrow distribution by a special microencapsulation technique. This is a prerequisite for accurate measurements, because the particles' size influences the temperature-sensitive ratio, as demonstrated in section 5.1.6.

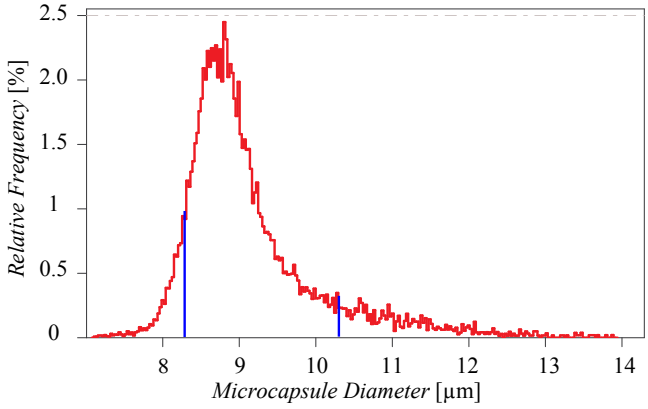

Figure 3.6: Frequency distribution of the microcapsule diameter. Blue lines mark the lower and upper limit of the 90 % interval.

3.1.2 Setup for fluorescent signal detection

In this section the optical setup will be described in detail. The main challenge is the simultaneous detection of two spectral bands on separate detectors. A high temporal and spatial resolution is required from the measurement technique and thus high-speed cameras with appropriate imaging optics are used.

Cameras and filters

In Figure 3.7 the arrangement of cameras and filters for image acquisition is sketched. Since this installation is fixed on a base plate, the whole setup can be displaced without the necessity of rearranging cameras and filters. Moreover, different imaging optics can be mounted on this acquisition unit, so that the optics can be adapted to the requirements of the specific application. The imaging optics used in this thesis are a Leica Z16APO microscope objective and a Nikon TE2000 inverted microscope. Both are described together with the respective experimental installation in section 3.1.4 and section 3.1.5. In front of each imaging optics a long-pass filter is installed (not shown in Figure 3.7) to separate the fluorescence signal from the exciting laser light. The implemented cameras[4] have a maximum acquisition rate of 3000 fps at full resolution of 1024 × 1016 pixels and a pixel depth of 10 bit grayscale. The camera sensor array is a complementary metal oxide semiconductor (CMOS), allowing a high readout speed and thus a high acquisition rate, but also showing a higher readout noise compared to charged coupled device (CCD) sensors.

Each of the CMOS-cameras detects the fluorescence signal in a different wavelength band. Camera A (CamA) is used to detect the temperature sensitive signal and camera B (CamB) captures the reference signal respectively. The fluorescence signal is split up according to its wavelength by means of a dichroic mirror[5] and the signal reaching CamB is additionally passing a shortpass filter[6].

In Figure 3.8 (a) the transmission spectra provided by the manufacturer of the optical filters are shown together with the temperature sensitivity curve from Figure 3.5. The dichroic mirror reflects light with a wavelength shorter than 590 nm, while light of longer wavelength is transmitted. However, it can be seen that in the longer wavelength region a part of the signal is reflected. To prevent this reflected light from reaching CamB, the aforementioned shortpass filter is placed into the optical path. The ratio shown in Figure 3.8 (b) is calculated using the emission data of the microcapsules I_{capsules} presented in Figure 3.5. The ratio R represents the quotient of the overall signal reaching CamB (S_{B}) and CamA (S_{A}) that is calculated by following equation

$$R = \frac{S_{\text{B}}}{S_{\text{A}}} = \frac{\sum_{\lambda=540nm}^{680nm} I_{\text{capsules}}(\lambda) \cdot (1 - T_{\text{Dichroic}}(\lambda)) \cdot T_{\text{Shortpass}}(\lambda)}{\sum_{\lambda=540nm}^{680nm} I_{\text{capsules}}(\lambda) \cdot T_{\text{Dichroic}}(\lambda)} \tag{3.7}$$

where T_{Dichroic} and $T_{\text{Shortpass}}$ represent the relative transmission of the dichroic and the shortpass-filter respectively. Since the resulting temperature-sensitivity of the ratio is 0.61 %/K and therefore only slightly smaller than calculated from the ratio in Figure 3.5, it can be concluded that the chosen optical filters are suitable for the separation of S_{A} and S_{B}.

As the temperature sensitivity increases with longer wavelengths, choosing the filters in such a way that only the emission at wavelengths higher than 650 nm reaches CamA, results in an enhancement of the temperature sensitivity and therefore the measurement accuracy. This is not applicable, though, because the radiant flux on CamA would be substantially smaller in this case, leading to dark images.

[4] *IDT*, N4 light
[5] *Omega Optical* XF2029
[6] *Omega Optical* 3rdSP570

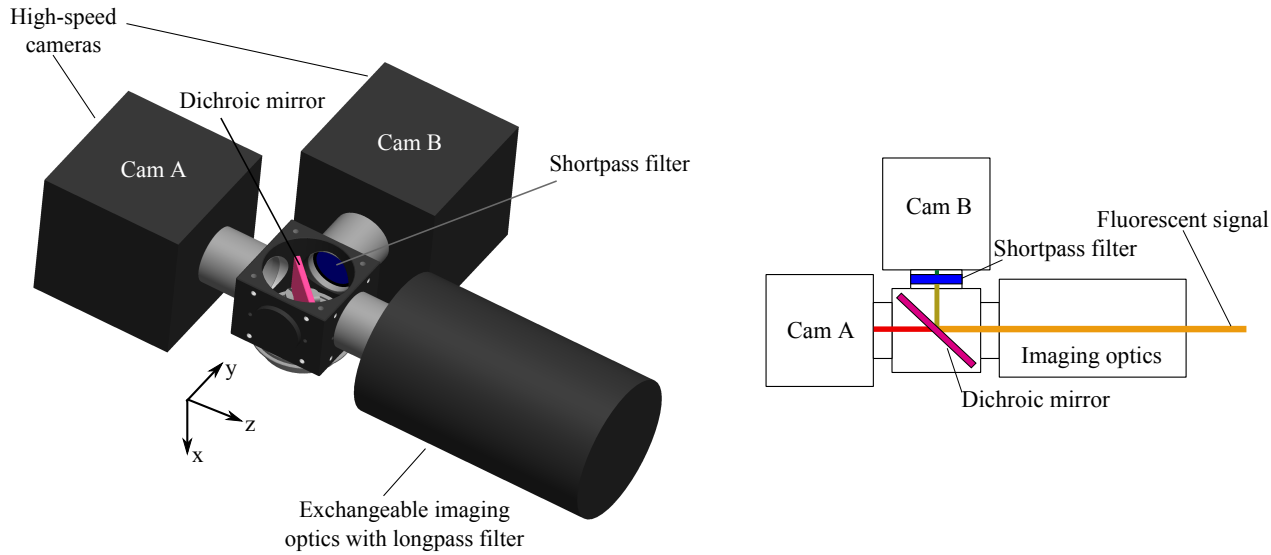

(a) (b)

Figure 3.7: Optical setup used to separate the fluorescent signal according to its wavelength and to image it on two detectors (high-speed cameras) in 3d-view (a) and in x-y-plane showing additionally the signal paths. Transmission and reflection characteristics of the filter and the dichroic mirror are shown in Figure 3.8.

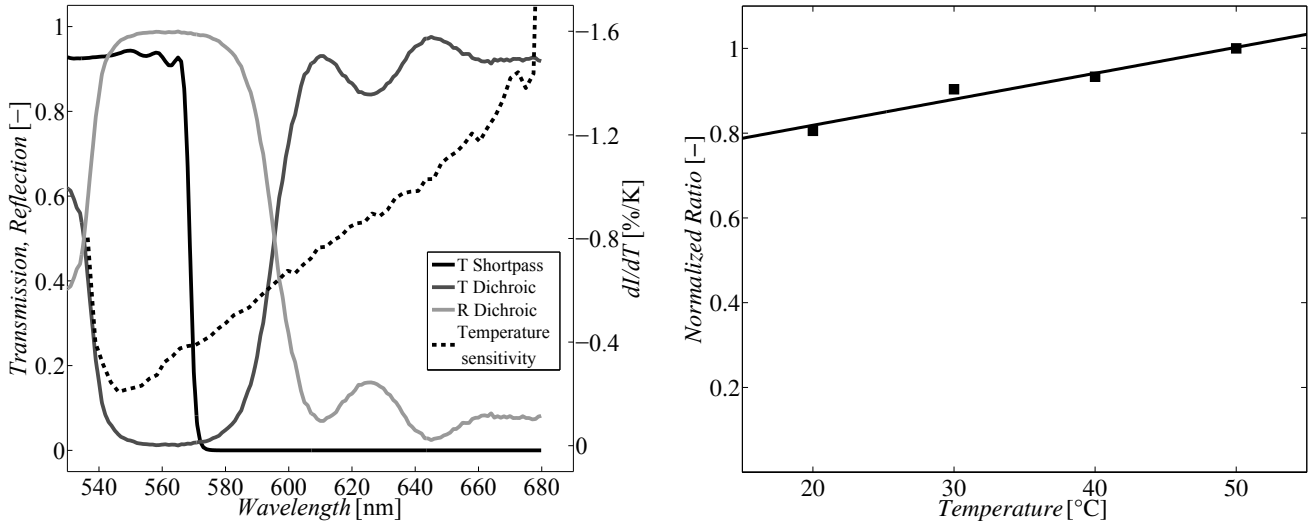

(a) (b)

Figure 3.8: Transmission (T) and reflection (R) characteristics (a) of the dichroic mirror and the shortpass filter used in the optical setup (Figure 3.7). In (b) the ratio is calculated from the spectral data of the microcapsules according to equation 3.7.

Arrangement procedure for cameras and filter

The dichroic mirror shown in Figure 3.7 is placed onto a rotatable and tiltable stage. This allows adapting the image section of CamB without altering that of CamA. CamB can be twisted around the y-axis (optical axis) and translated along this axis to adjust the image distance and therefore the magnification of both cameras. During the arrangement a glass scale with a line distance of 25 µm is used as the object that is imaged onto both cameras. Doing so, the matching of the images can be controlled very precisely. However, a physical misalignment of the cameras remains after the matching, which has to be corrected during the image processing (see section 4.1.1). After this camera alignment procedure the cameras are screwed on aluminum plates, which are again fixed in that position by a base frame.

3.1.3 Setup for excitation of fluorescence

Laser

The laser used for the fluorescence excitation is a Nd:YAG solid-state laser. There are two single laser cavities pumped by one single arc-lamp. Acoustic-optic modulators (Q-switches) enable laser pulse generation with a repetition rate of 1000 Hz and a pulse energy of 14 mJ each. The temporal shift between the pulses can be set to an arbitrary value allowing PIV also for fast moving particles at high optical magnifications. Nevertheless, for the measurements presented in this thesis, both pulses were always fired at the same instant. For simplicity's sake in the following this "double-pulse" will be treated as a single pulse with double pulse energy.

The light exiting the laser cavities has a wavelength of 1064 nm. Using non-linear effects of a Lithium triborate (LBO)-crystal, the light's wavelength is converted to 532 nm (second harmonic generation) before the laser pulses leave the laser unit.

Synchronization and triggering of cameras and laser

As the laser power shows fluctuations from pulse to pulse, it is very important that the corresponding images of CamA and CamB are illuminated by the same laser pulse. Thus, laser pulse generation and camera acquisition must be synchronized exactly. To ensure this, an external trigger signal is generated (5 V, TTL-signal) that starts image acquisition and laser pulse generation simultaneously. In Figure 3.9 the triggering and timing of laser and cameras is sketched.

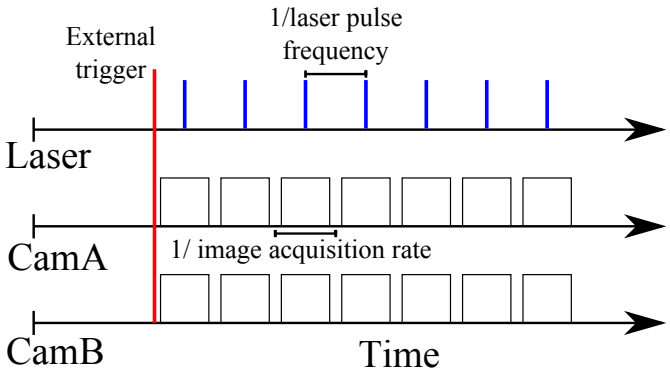

Figure 3.9: Timing diagram for synchronized laser pulses and camera acquisition.

Camera exposure time (min. 1×10^{-3} s) is long compared to the laser pulse and fluorescence duration ($\approx1\times10^{-7}$ s). Since the dark noise increases with the exposure time, it is desirable to reduce it. The

exposure time can be shortened independently from the image acquisition rate. However, for pulsed illumination with such short pulses, the exposure time must be set to the maximum (1/acquisition rate), because otherwise it can happen that the laser pulse is fired, while the camera shutters are closed. This is due to the fact that the location of the time slot, during which the camera shutters are open, cannot be controlled. Consequently, a decrease in the image acquisition rate results in images with a higher contribution of dark noise.

The maximum pulse repetition rate of the laser is 1000 Hz, while the maximum camera acquisition rate is 3000 Hz. Thus, the maximum acquisition rate for the presented setups is 1000 Hz.

Light sheet optics

The laser light is guided by a laser arm containing mirrors at its joints. In this way the position of the laser exit can be easily adjusted to the actual setup.

For some experimental installations, a light sheet is formed from the round laser beam. This is done by focusing the collimated beam using a spherical convex lens and expanding the beam in one direction by a cylindrical concave lens. Such a light sheet optic is illustrated in Figure 3.10. For the present work convex lenses with different focal lengths reaching from $f_{\text{convex}} = 77$ mm to $f_{\text{convex}} = 333$ mm and concave lenses with $f_{\text{concave}} = -100$ mm or $f_{\text{concave}} = -400$ mm are used.

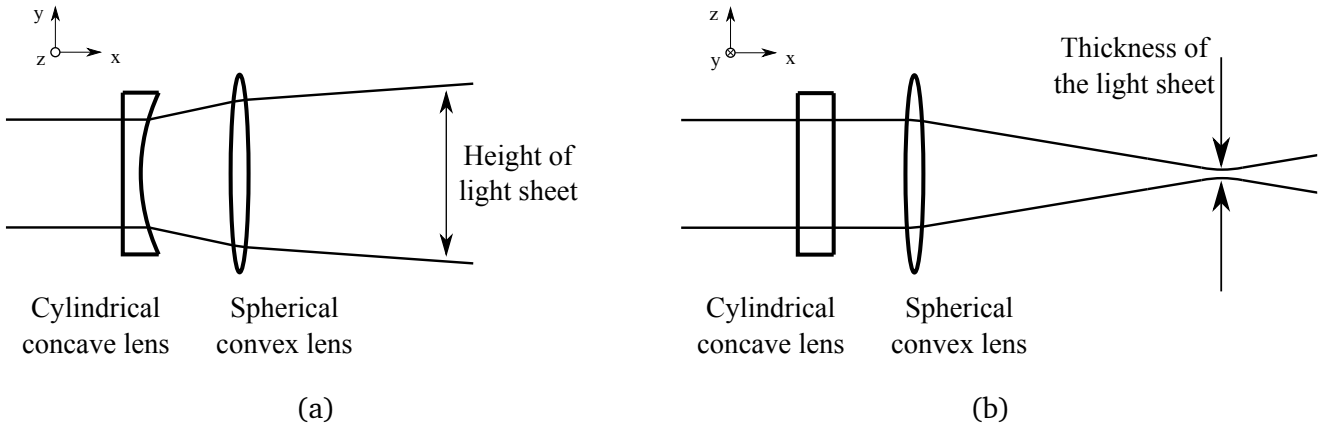

Figure 3.10: Schematic of the optics used to form the laser light sheet in x-y-plane (a) and x-z-plane (b)

According to [17] the minimum waist w_{min} of the (gaussian) laser beam, which corresponds to the minimum thickness of the generated light sheet, can be calculated from equation

$$w_{\text{min}} = \frac{4\lambda \cdot f \cdot M^2}{\pi \cdot w_{\text{exit}}} \tag{3.8}$$

with a quality factor of $M^2 = 12$ (characteristic quantity of the laser) , a wavelength of 532 nm and a beam diameter at the laser arm exit of $w_{\text{exit}} = 10$ mm specified for this laser and a total focal length of the convex lenses $f = 333$ mm this results in $w_{\text{min}} = 0.27$ mm.

The height of the light sheet is measured and is approximately 30 mm for $f_{\text{convex}} = 333$ mm, $f_{\text{concave}} = -100$ mm and approximately 2 mm for $f_{\text{convex}} = 77$ mm and $f_{\text{concave}} = -400$ mm at the measurement position.

3.1.4 Natural convection experiments using light sheet illumination

Setup

The setup described in the following is used to create a homogeneous temperature distribution in the measurement volume during calibration and create a temperature difference between two side walls resulting in a flow driven by natural convection for the subsequent measurements. The results of these experiments are presented in section 5.1.4 and demonstrate the applicability of the developed microcapsules for simultaneous temperature and velocity measurements.

In Figure 3.11 the experimental setup is sketched. Two water-bath thermostats are used to set temperature T_1 and T_2 in two copper blocks forming the boundaries on the right and the left side of the measurement volume. Its remaining walls are made from polycarbonate. This construction is called "Convection Cube" and is shown in Figure 3.12.

The temperature is measured inside the copper blocks and in the investigated fluid in which the microcapsules are dispersed by means of thermocouples (TC). To excite the microcapsules in the entire measurement plane, the light sheet optics described in section 3.1.3 is used. The fluorescence signal is then imaged on two cameras using the optical setup described in section 3.1.2 in combination with an Leica Z16APO objective. This results in grayscale images of the particles, seen as small bright dots on a black background.

The Convection Cube together with the light sheet optics are attached to translation stages, allowing correct positioning of the measurement volume in the field of view as well as adaption of the object distance. For the imaging optics used, the object distance (78 mm) is fixed, while the optical magnification can be adapted from 0.57 to 9.2. Due to missing specifications, the depth of field of the optics can not be calculated. However, the depth of field was estimated experimentally by alteration of the object distance. The measured depth of field is approximately 0.5 mm for the optical magnification of approximately 1 used in most of the presented experiments. Since the depth of field exceeds the thickness of the light sheet, all illuminated particles appear non blurred in the images.

Experimental procedure

The preparation of the investigated fluid seeded with microcapsules includes the following steps:

- Mixing of high-purity water (73 %Vol.) with glycerol (27 %Vol.) and Tween20 (surfactant, <0.0001 %Vol.),
- Adding highly concentrated (67 mg/ml) particle dispersion to the mixture (2 %Vol.) resulting in an overall concentration of 1.4 mg microcapsules per 1 ml water-glycerol mixture,
- Degassing of the dispersion with a heated ultra-sonic bath.

Adding glycerol results in a mixture density close to that of the microcapsules. Doing so, the microcapsules are prevented from sinking due to buoyancy effects. The added surfactant inhibits agglomeration of microcapsules and thus further stabilizes the dispersion. Preliminary investigations revealed that both measures are necessary to guarantee a homogeneous particle distribution in the liquid during the entire experimental procedure. Little alterations in the signal acquisition installation or the position of the measurement volume influence the absolute ratio. Consequently, an in-situ calibration has to be performed before or after each series of measurements. All parameters besides the temperature must be kept constant during calibration and measurement. Additionally, the temperature distribution in the

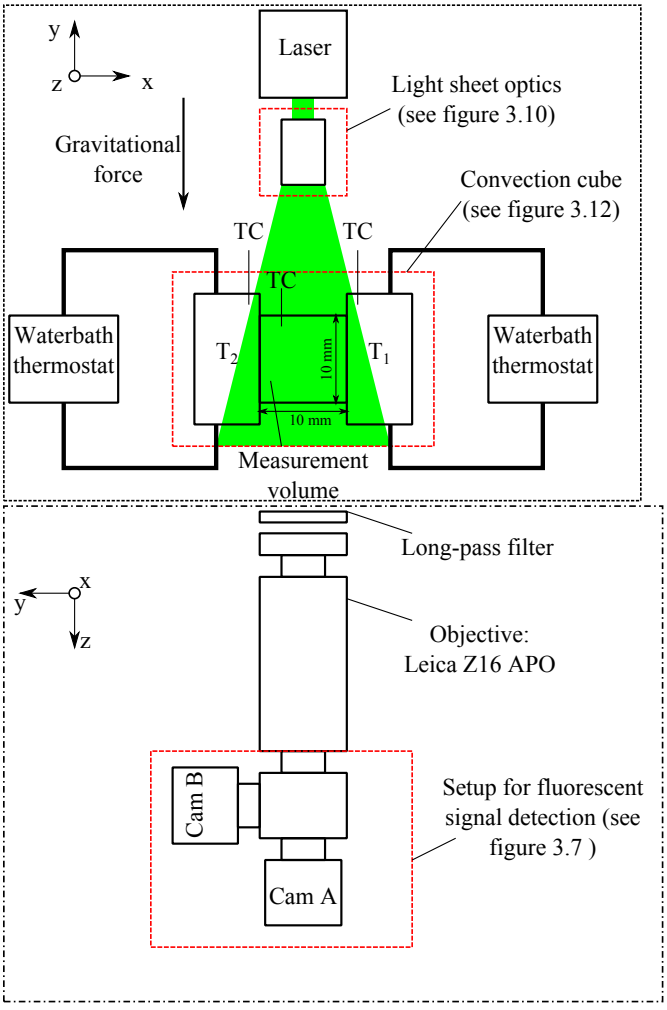

Figure 3.11: Schematic of the experimental setup used to excite and measure the temperature and velocity field of a flow driven by natural convection.

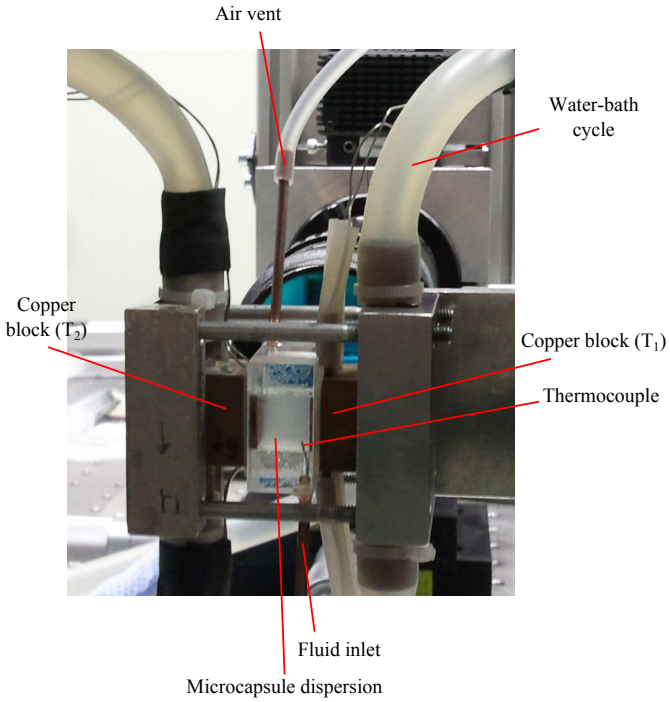

Figure 3.12: Picture of the Convection Cube, which is used to induce a characteristic temperature-and flow profile, driven by natural convection. In the background part of the signal detection setup (objective and camera) can be recognized.

measurement volume must be homogeneous. All necessary alignments are performed before the temperature is increased linearly using the temperature-controlled bath-thermostats. When a temperature rise of 1 K is detected by the thermocouple inside the measurement volume, a trigger-signal activates the laser and the camera acquisition simultaneously. A homogeneous temperature distribution is obtained by a slow heating rate (1 K/min) and a vortex that is driven by a slight temperature difference between the tempered side walls. For each calibration step, at least 50 images for each camera are taken and stored.

After the calibration procedure one side wall is heated to $T_1 = 50$ °C and the temperature of the other side wall is set to $T_2 = 20$ °C. This temperature difference leads to gradients of the specific density, which again induce a flow and cause a characteristic temperature profile. After stabilization of this convective flow, the actual measurements are performed. To enable temporal averaging during data processing, numerous measurement sequences with at least 50 images each are taken.

3.1.5 Capillary flow experiments using volume illumination

The applicability of the microcapsules in combination with volume illumination is investigated, because this type of illumination has to be used in most microscale applications. Therefore, an experimental setup is installed, which allows the creation of a three-dimensional temperature- and flow profile inside a capillary tube (inner diameter: 1.16 mm).

Setup

An schematic overview of this installation with its main components can be found in Figure 3.13. Figure 3.14 shows a cross-sectional view of the copper blocks used for tempering the capillary tube. They are thermally separated by a PTFE insulation and their temperature can be controlled independently

from each other by two water-bath thermostats. The capillary runs through a cavity in both blocks and is pushed through the PTFE insulation.

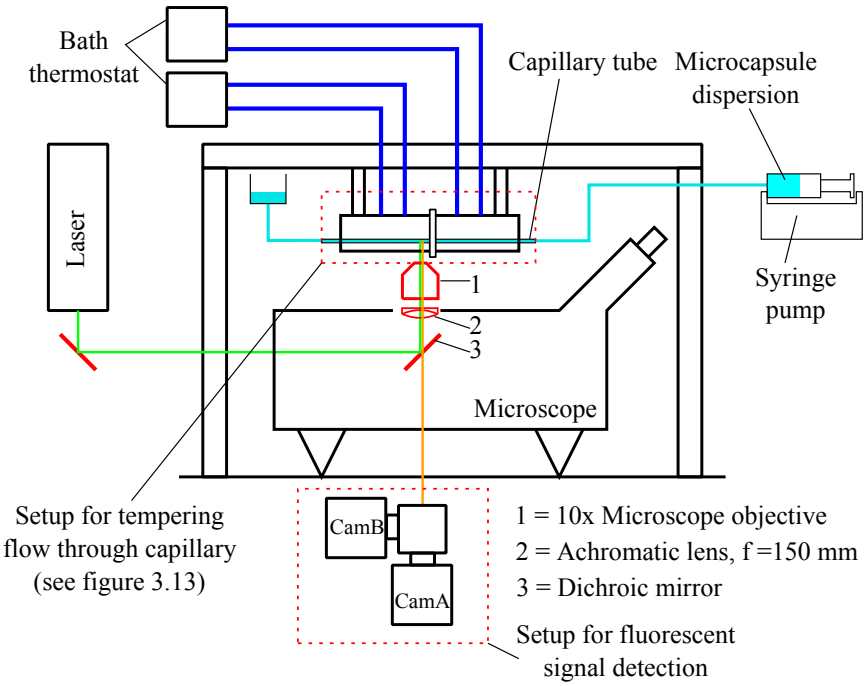

Figure 3.13: Sketch of entire measurement setup for experimental investigation of the flow in the capillary tube.

The gap between the tube and the copper walls is filled with glycerol which serves as a heat transfer medium and enables refractive index matching, because the refractive index of glycerol matches approximately that of the capillary material (borosilicate glass). Thus, refraction at the curved interfaces between the outer capillary wall and the surrounding glycerol is negligible. Using glycerol as the test fluid running through the capillary and carrying the microcapsules, enables refractive index matching at the inner capillary wall as well. This refractive index matching approach has also been used by Chamarthy et al. [12] who investigated the convection patterns near an evaporating meniscus by means of μPIV. They used methanol as the test fluid and water as outer fluid, so that fluorinated ethylene propylene (FEP) is used as wall material for the capillary tube, since methanol, water and FEP have similar refractive indices. Because the temperature cannot be measured directly in the tube, it is measured close to its outer wall, in the heat transfer medium (outer glycerol), by means of thermocouples. For each copper block the temperature is measured close to the PTFE insulation (TC_2 and TC_3) and close to the outer walls (TC_1 and TC_4). The inner glycerol (test fluid) is flowing from the right side to the left side due to a pressure gradient generated by the syringe pump. In Figure 3.14 the sealings that prevent the outer glycerol from leaking are not shown. They are implemented by silicon tubes and heat shrink tubes. The capillary tube is connected to the syringe on the right side and to the reservoir on the left side by flexible silicon tubes as well.

During the calibration procedure the temperature of both copper blocks is identical. The test fluid adapts to this temperature, while it is flowing through the capillary. Thus, the fluid temperature at the measurement position is assumed to be equal to the temperature measured in the heat transfer medium and having a homogeneous distribution. The maximum flow rate for which this assumption is valid, is evaluated for the calibration case, as this case shows the highest temperature difference between

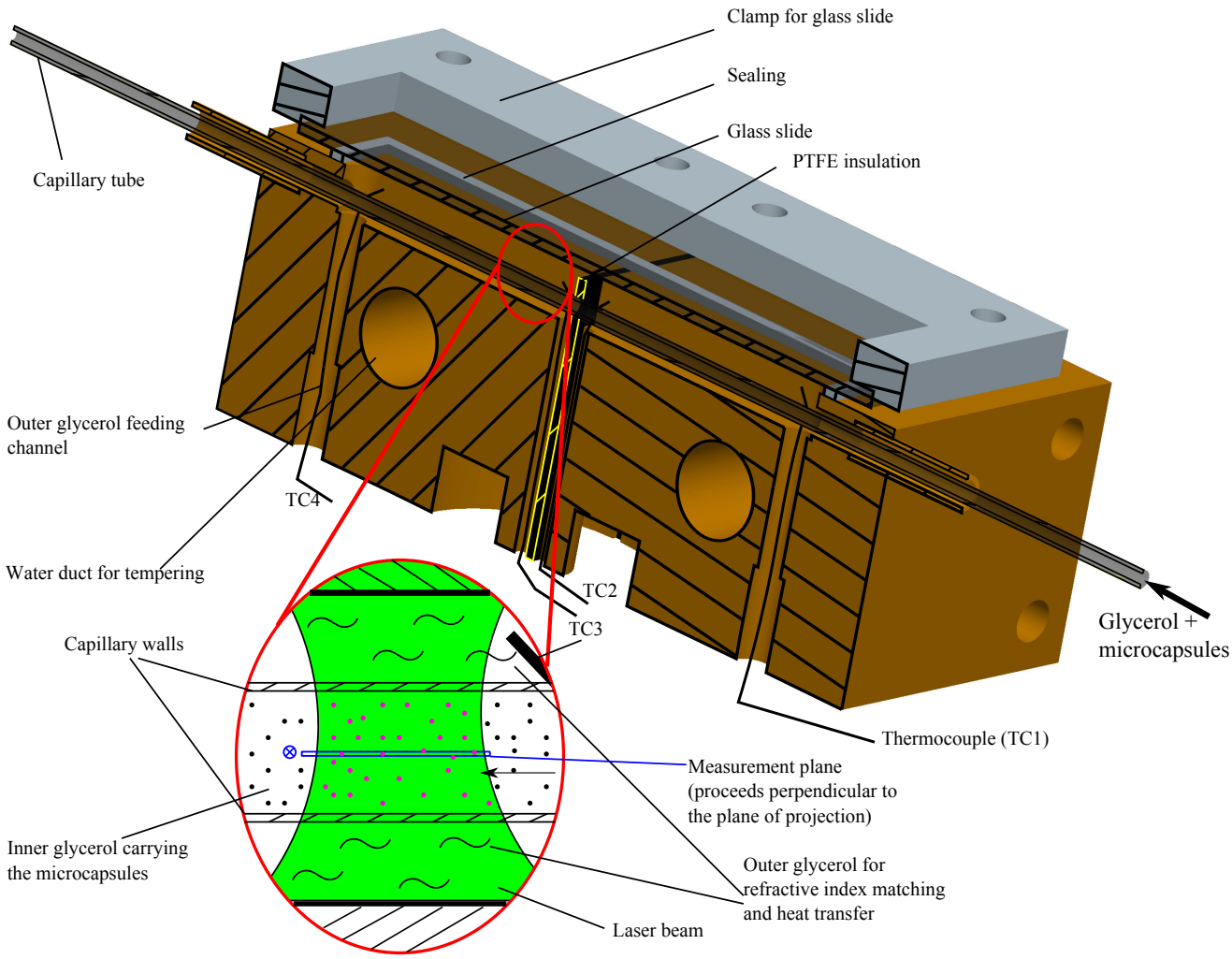

Figure 3.14: Cross-sectional view of the copper blocks used to create a distinctive temperature field in the capillary view.

the entry of the test fluid and the measurement position. Therefore, the solution of the unsteady heat conduction in a cylinder[7] is used. The Biot number is calculated according to

$$Bi = \frac{\chi \cdot L}{\kappa} \tag{3.9}$$

with the following assumptions. A fluid element entering the capillary at room temperature (23 °C) experiences a warming with an unsteady heat flux while it is flowing through the capillary. The far field temperature is that of the copper block and can be assumed as constant and is at maximum 50 °C. The heat transfer coefficient (χ) from the copper to the inner glycerol is determined by the conduction through the outer glycerol and the capillary wall. Hence χ is evaluated to be 130 W/(m^{2}K). Furthermore, κ represents the thermal conductivity of the inner glycerol. The length L is equivalent to the inner radius of the capillary (0.58 mm). Consequently, the Biot number results in $Bi = 0.25$. From the mentioned diagrams, the Fourier number for which the normalized temperature is close to zero for $Bi = 0.25$, is determined to be $Fo \approx 10$. Thus, the necessary residence time is calculated with equation 3.4 and the thermal diffusivity of glycerol, resulting in $t = 34$ s. During the calibration, the flow-rate is 2 ml/h, which results in a residence time of 52 s. Numerical simulations (see section 5.1.1) also showed that the flow adapts to the temperature of the copper blocks within the heated length of the capillary even at the highest flow rate of 8 ml/h.

For the measurements, different temperatures are applied to the right and the left copper block. On its way through the tube, the test fluid first adapts to the temperature of the right copper block. It is again assumed that the temperature distribution before the insulation is homogeneous and equal to the temperature measured in the heat transfer medium. Right after the insulation, the temperature of the outer glycerol changes rapidly and a heat flux in radial direction establishes due to this temperature gradient. This results in a three-dimensional temperature profile governed by a combination of heat conduction and forced convection. At a certain distance from the insulation the test fluid has again completely adapted to the temperature of the left copper block. Hence, the measurement position must be chosen carefully to measure the well-established temperature profile before the temperature difference vanishes again.

The microcapsules that are dispersed in the test fluid are illuminated by the previously described Nd:YAG-laser. A dichroic mirror (3) inside the microscope serves as a long-pass filter and separates the excitation light from the fluorescence signal. The 10x microscope objective (1) with a numerical aperture of 0.3 focuses the laser light on the measurement region and collects the signal. When the camera port of the microscope[8] is used, the cameras must be mounted at a certain distance from the microscope exit. However, this criterion can not be met, due to optical components in front of the cameras (see Figure 3.7). Hence, an achromatic lens (2) is placed in the light path, which reduces the divergence of the signal beam and therefore allows placing the detection unit at a larger distance.

Experimental procedure

A dispersion of microcapsules in glycerol is prepared by mixing 0.055 ml of the highly concentrated microcapsule dispersion in water (equivalent 3.7 mg microcapsules) and 10 ml of pure glycerol. This results in an overall concentration of 0.37 mg microcapsules per 1 ml glycerol. This concentration must be much lower than the one used in section 3.1.4, because volume illumination is applied. Because all microcapsules along the laser beam path are excited, the fluorescent signal from the particles in the focal plane (measurement plane) is superimposed by the signal of particles in front of and behind this plane. These out-of-focus particles are pictured as circles on the images, whereas in-focus particles appear as dots. To reduce the influence of the out-of-focus particles, the overall microcapsule concentration must be

[7] Figure 7, page Ec7 in [83]
[8] *Nikon TE2000*

chosen carefully. The number of particles must be high enough for spatially resolved measurements and it should be small enough that the dots are separable from the circles in the images (see also section 4.1).

The syringe pump guarantees a constant mass flow of the inner glycerol with particles through the capillary tube. The flow rate was kept constant during the calibration at 2 ml/h, while it was varied during the measurements from 0.25 ml/h to 8 ml/h. Here it has to be clarified that the actual flow rate is 1.8 times higher than the one stated here and in the results section, because the diameter of the syringe is different from the one used to calculate the flow rate of the syringe pump. However, this is considered for the input data of the numerical simulations, facilitating the direct comparison of measurement and simulation.

In the first step of the experiments, the focal plane of the imaging system is set to the middle of the capillary tube. Therefore, the object distance is adjusted such that the fastest particles appear as non-blurred dots. This is a very important step, as the temperature in the capillary, strongly depends on the radial position (r-axis). For the simulation axial symmetry about the rotational axis (z-axis) of the tube is assumed and a two-dimensional simulation is performed. Hence, comparability of measurement and simulation can only be provided, if the measurement plane (focal plane) coincidences with the rotational axis. In the next step the axial distance of the field of view from the insulation is set to approximately 6 mm. The measured temperature distribution depends on the flow rate and the axial position, as the temperature gradient decreases along the z-axis. Previous numerical simulations showed that at this position a distinctive temperature profile is observable for the specified flow rates.

After the measurement position is defined, no further changes on the experimental setup (besides alteration of temperature and flow rate) are allowed. An in-situ calibration is performed by applying the same temperature to both copper blocks and varying it in steps of 1.5 K from 20 °C to 50 °C. Between two steps a waiting time of at least 6 min is provided to ensure adjustment of the inner glycerol temperature to the preset one. When the calibration is finished, the temperature of the first (in flow direction) copper block is set to 25 °C, while the other one remains at 50 °C. Measurements are taken for different flow rates and the waiting time between each alteration is again at least 6 min to allow development of the flow and temperature profile. When the flow rate of the inner glycerol is set to 0 ml/h, a temperature difference of circa 3 K between TC_1 and TC_2 as well as between TC_3 and TC_4 establishes due to the heat transfer through the PTFE insulation between the two copper blocks. However, the difference between TC_1 and TC_2 diminishes for higher flow rates ($\approx$ 1.5 K at 8 ml/h) whereas the difference between TC_3 and TC_4 increases ($\approx$ 7.0 K at 8 ml/h) because of the heat transfered from the outer to the inner glycerol.

For calibration and measurements, a series of 500 image pairs is taken for each step. The image acquisition rate is set to 30 Hz. For this value, there is still a recognizable particle displacement between subsequent images at the minimum flow rate and for the maximum flow rate the same particle can still be seen in at least two images.

3.1.6 Homogeneous temperature distribution experiments

The setup named "Forced Convection Cube" and described in the following is used to generate a defined, homogeneous temperature distribution in the measurement volume. A comparison of the measured and the known temperature in the test section facilitates the characterization of the developed technique based on microcapsules.

Setup

Such a homogeneous temperature distribution could also be realized with the setup described in section 3.1.4, but its polycarbonate walls limit the maximum laser power density, because it gets carbonized locally when a very small (height $\approx$ 2 mm) light sheet is used. For that reason, glass windows are implemented in the Forced Convection Cube that can withstand much higher laser power densities.

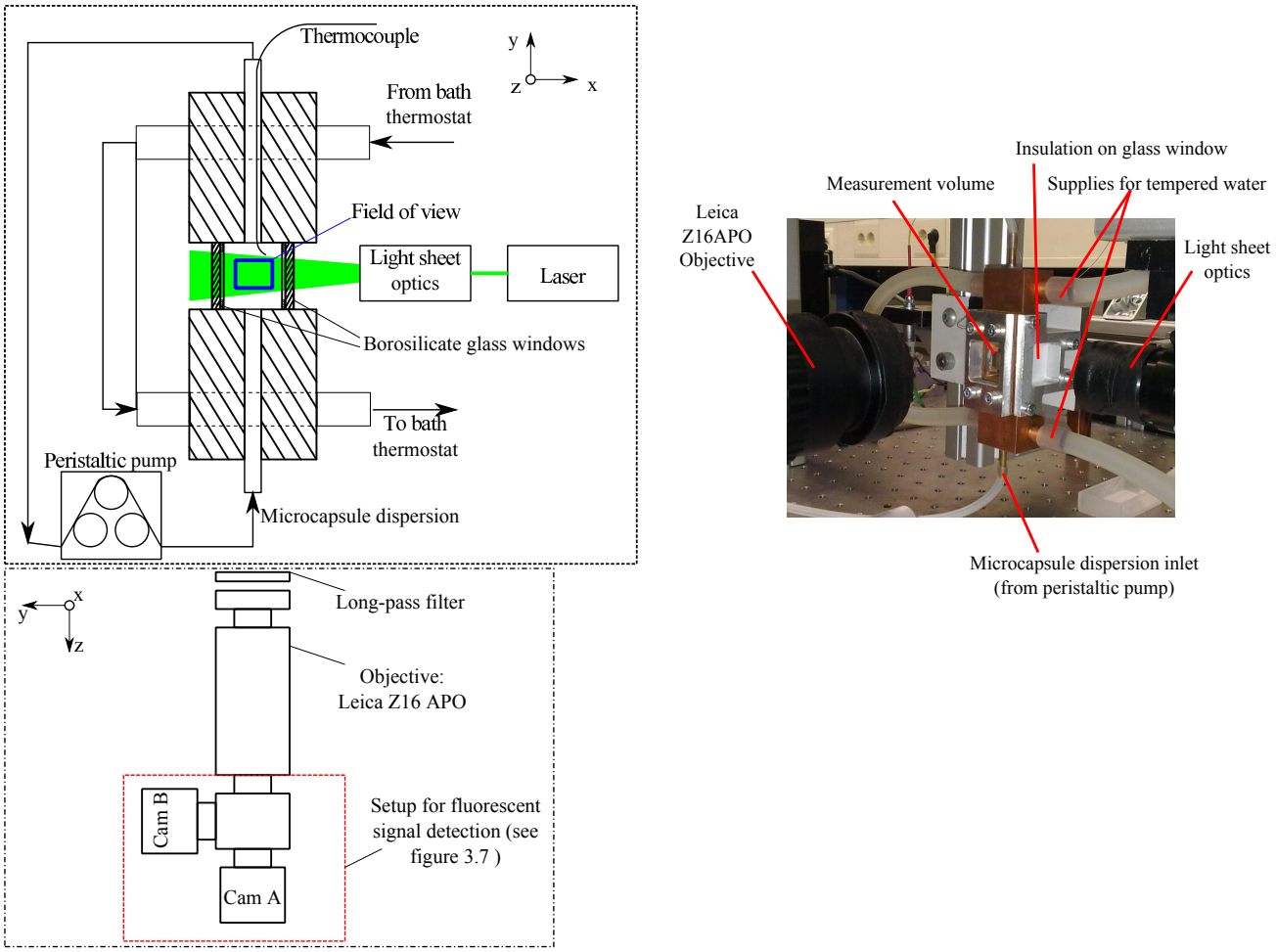

Figure 3.15: Schematic (a) and image (b) of the forced convection cube used to create a defined homogeneous temperature distribution and a uni-directional flow.

In Figure 3.15 a schematic (a) and a picture (b) of the Forced Convection Cube together with the peripheral devices is shown. The optics used for detection of the fluorescent signal are the same as for the Convection Cube. The temperature of the copper blocks is again controlled by means of a bath thermostat and the actual measurement region is located in the middle of the cavity in the copper block. When the microcapsule dispersion enters the copper block it flows through a drilled hole and adapts to the copper's temperature. The heat losses through the glass windows are minimized by putting an insulation on the outer sides of the glasses and leaving only small slits for illumination and signal detection. In Figure 3.15 (b) the insulation on the right side can be recognized, while it is missing on the front window for this case. The measurement volume can be regarded as adiabatic and a homogeneous distribution of temperature can be assumed.

Circulation of the measurement dispersion by the peristaltic pump is necessary for two reasons. Firstly, to prevent the particles from sinking due to buoyancy and secondly, a defined velocity field pointing in a defined direction is desired to characterize the measurement technique.

Experimental procedure

The experiments are carried out analogously to the measurements with the Convection Cube (section 3.1.4) and likewise include mixing of the particle dispersion followed by an in-situ calibration and the actual experiments. The goal is to investigate how different parameters influence the measurement accuracy. One of these parameters is the number of particles that is taken into account in the averaging process. For this investigation, a defined particle displacement between subsequent images and a defined mean particle distance in one image is necessary. For that reason, the concentration of the microcapsules in the test fluid and the flow velocity must be definite. Moreover, the Forced Convection Cube is used to study the effect of the particles' brightness and a varied laser power on the results. Therefore, measurements at different electrical input powers of the laser are performed.

3.2 Solid microparticles from dyed polymers

To incorporate fluorescing molecules into solid polymer particles the fluorescent dye and the polymer are dissolved in an appropriate solvent. When the solvent is extracted, the dye remains molecularly incorporated in the polymer matrix. This technique is used for the application of thin polymer films on a surface to measure its temperature, as described in section 2.2.2.

When the polymer solution is emulsified into small droplets, dyed polymer particles with a small size can be produced. Such an emulsion can be realized by adding the polymer solution to a stirred water bath. The solvent diffuses into the water and solid polymer particles are formed. The particles' size as well as the size distribution ranges from some µm to some mm and depends on many factors, such as the stirring velocity and the type and amount of the solvent. In Figure 3.16 the principle of the microparticles' fabrication is sketched (a) and some fluorescing particles produced in this manner and observed with a microscope are shown in (b).

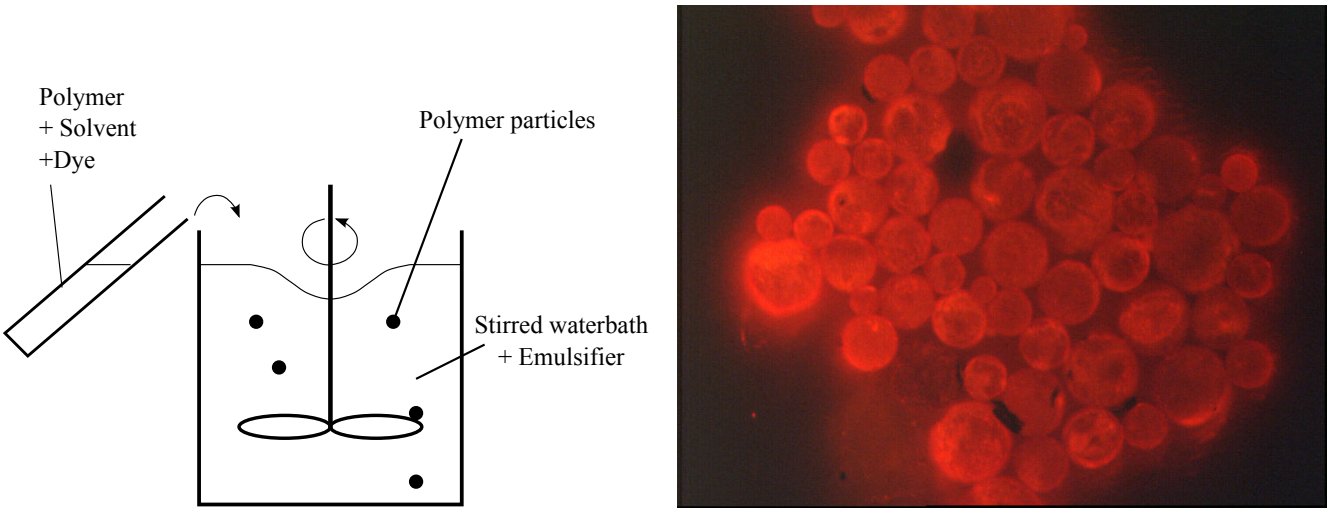

Figure 3.16: Schematic of the production procedure of dyed, solid polymer particles (a). In (b) particles fabricated in this way and observed by means of a fluorescence microscope are shown.

This process for the fabrication of micro particles is a well established method and generally called emulsification solvent evaporation technique. Detailed descriptions about this technique can be found in [52], [75] and [88].

3.2.1 Dyes excitable at 532 nm

The following experimental investigations, as well as the results presented in 5.2.1, were acquired in the context of a bachelor thesis. In the following only the most important tests and findings are considered. For a more detailed characterization it is referred to [57].

Selection of fluorescent dyes and polymers

In [45] several fluorescent dyes that are employed for the determination of temperature in polymer films (TSP) can be found. From that list, rhodamine B (RhB) shows a temperature sensitivity in polymers in the desired temperature range and is excitable at 532 nm by the available Nd:YAG-laser. Instead of RhB, sulforhodamine B (SRhB) is chosen because it exhibits very similar fluorescence characteristics with a

red-shift of the emission maximum ($\lambda_{em,max,RhB}$ = 580 nm, $\lambda_{em,max,SRhB}$ = 590 nm; measured in aqueous solution). Thus, a reference dye with an emission peak between the excitation wavelength (532 nm) and the maximum emission wavelength of SRhB can be applied.

According to Romano et al. [58], the glass transition temperature is an important criterion for the temperature sensitivity of a dye in a solid polymer matrix. From the theory of fluorescence this can be explained by the reduced rigidity of the polymer matrix, when the glass transition temperature is exceeded. Hence, the transfer of energy from an excited dye molecule to the surroundings becomes more efficient. Due to this finding, potential polymers for the fabrication of microparticles have been chosen with regard to their glass transition temperature. Furthermore, the producibility of particles from this polymer by means of the emulsification solvent evaporation technique must be granted. By testing, polybutylmethacrylate (PBMA) and polyvinylacetate (PVAc) with a glass transition temperature of 15 °C [70] respectively 27 °C [64] are chosen as the polymers fulfilling these criteria best.

The reference dye should exhibit the following characteristics:

- None or only minimal dependency on temperature in its emission intensity,
- Excitable at 532 nm (laser wavelength),
- Emission maximum between 532 nm and 590 nm (between laser wavelength and emission maximum of SRhB).

For most dyes, no fluorescence properties in polymers are available in literature. For that reason, rhodamine 6G (Rh6G) is chosen as reference dye from its fluorescence characteristics in water.

Fabrication of polymer films

For the examination of particles, two main problems arise. Firstly, during their production by means of the emulsification solvent evaporation technique, a portion of the used dyes can dissolve in the water bath, so that the amount of dye incorporated in the particles can vary strongly. Secondly, the particles cannot be fixed at a specific position. These problems are overcome when films are investigated.

The polymer films are produced by dissolving one dye (RhB) respectively two dyes (RhB + Rh6G) together with the polymer in methylene chloride. This mixture is then applied onto a microscope slide and the solvent is evaporated.

Experimental setup and procedure

The experimental setup used for the investigation of polymer films with regard to their temperature sensitivity without distinguishing between different wavelengths, is shown in Figure 3.17. A bath thermostat is used to pump tempered water through the holes drilled in the copper block and thus regulates the copper block temperature. A spacing is formed by the copper block, the sealing from silicone rubber and the glass slide. In this interspace the polymer film is located and surrounded by water that serves as heat transfer medium. The polymer film is observed using an inverted fluorescence microscope. Fluorescence excitation is realized by the Nd:YAG-Laser and the signal is collected by a CMOS camera[9]. The brightness of the resulting images are a measure for the intensity of the fluorescent emission in the entire wavelength range.

To investigate the suitability of dye combinations for temperature measurements following the 2-colour-LIF principle, the fluorescence signal is determined as a function of wavelength. Therefore, a spectrometer[10] is implemented in the installation illustrated in Figure 3.18. The dyed polymer film is

[9] *TSI*, Powerview HS650
[10] *Horiba*, Triax320

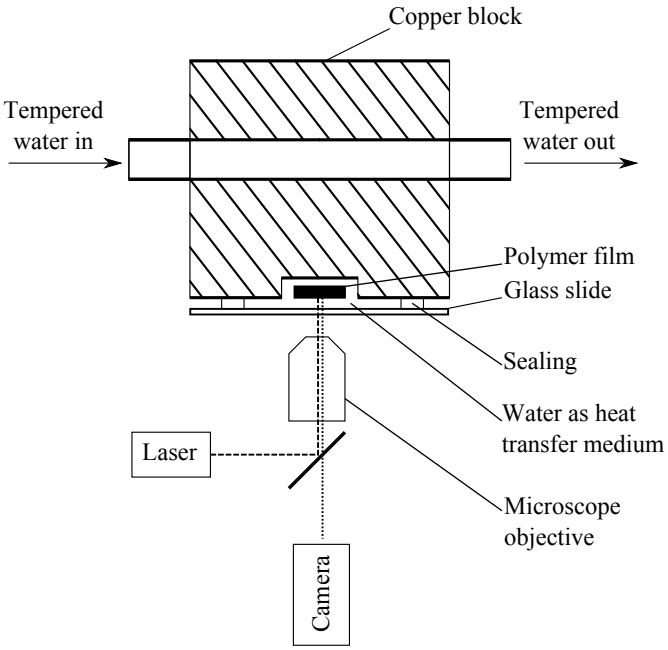

Figure 3.17: Schematic of the experimental setup used to investigate the fluorescence emission intensity of polymer films as a function of temperature.

fixed in a cube made from polycarbonate, by means of two adjunctive microscope slides. A water flow through the cube tempers the polymer film. The fluorescence signal is imaged on the entrance slit of the spectrometer.

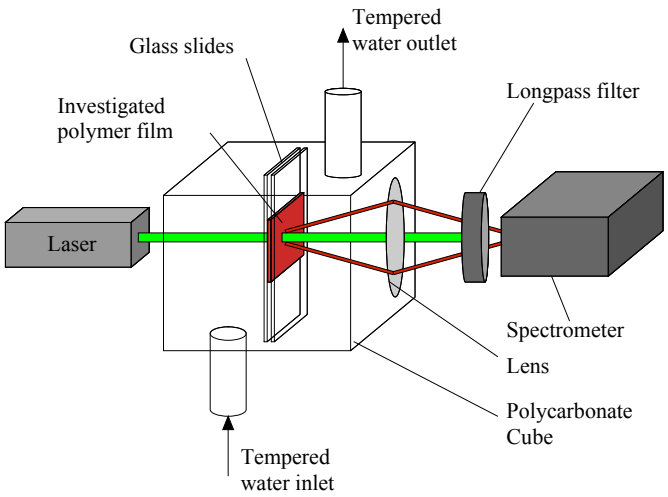

Figure 3.18: Schematic of the experimental setup used to investigate the emission spectra of polymer films as a function of temperature.

3.2.2 Dyes excitable with UV-light

EuTTA (see section 2.2.2) has been used as a temperature sensor on surfaces [31], [97] and also for combined measurements of temperature and velocity [72], [73] using both, luminescence decay-time (lifetime) based and intensity based approaches. The lifetime based technique used in [73] cannot be applied, as a pulsed laser with the appropriate wavelength (UV-region) is not available.

For intensity based methods, a reference dye must be used to compensate for the fluctuations in particle size, when particles instead of immobile polymer films are used. Basu and Venkatraman [4] used polystyrene films dyed with a combination of EuTTA and perylene for intensity based temperature measurements following the 2-colour-LIF method.

These dyes, however, cannot be excited with the available Nd:YAG-Laser, but need UV-light for excitation. Thus, an UV-LED with an emission maximum of approximately 365 nm is implemented as light source.

Fabrication of polymer films and particles

In [4] it was shown that temperature measurements are feasible using polystyrene dyed with EuTTA and perylene. The fabrication of spherical particles with a well-defined size is the problem to be solved. The above presented emulsification solvent evaporation technique has been tested as a method to produce spherical microsparticles. But this technique appears to be unsuitable, as part of the dyes diffuses out of the formed microdroplets together with the solvent. Hence, a consistent distribution of both dyes in the formed microparticles, which is prerequisite for temperature measurements, cannot be assured.

To overcome this problem, dyed polymer films are produced according to the procedure described in section 3.2.1. In practice 0.28 mg EuTTA and 0.12 mg perylene, both in form of powders, are added to a solution of 61 mg polystyrene in 1 ml methylene chloride. This mixture is then applied onto a glass slide. After drying these films for 24 hours, the solvent is completely evaporated and the dyes are homogeneously distributed in the polymer layer. In the next step, the films are mechanically pulverized by means of a pestle. The resulting particles do not show a spherical shape (flakes, as shown in Figure 5.27). Nevertheless, they are adequate to examine the applicability of polymers dyed with EuTTA and perylene for temperature measurements in liquids.

Investigation of polymer particles

A sketch of the setup used to inspect the polymer flakes can be seen in Figure 3.19. The particles are dispersed in water and filled in the cube described in section 3.1.6. Its temperature is controlled by means of a bath thermostat. The particles are illuminated by the mentioned UV-LED and the fluorescence signal is observed simultaneously by a spectrometer and a 3-CCD-colour camera[11]. Three CCD-sensors (each with 748 $\times$ 576 pixels) are installed in this camera. Each of them records an image in different wavelength bands that are stored in apart matrices for red, green and blue (blue image: 400 nm to 500 nm; green image: 475 nm to 600 nm; red image: 550 nm to 700 nm).

Thus, it is possible to distinguish between signals of different wavelength bands, facilitating a 2-colour-LIF approach without the need for a second camera, if the wavelengths of the measured signals differ sufficiently. For the mixture of EuTTA and perylene incorporated in polystyrene, this requirement is met very well.

[11] *Hitachi* HV20

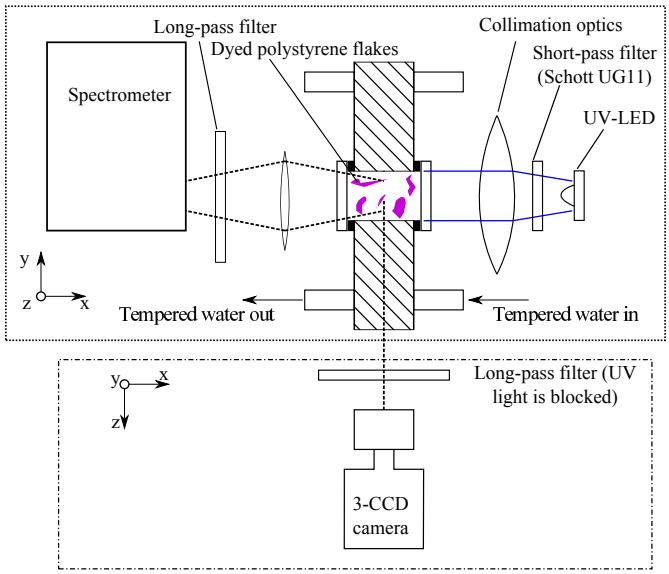

Figure 3.19: Schematic of the setup used to investigate the temperature-sensitivity of EuTTA-dyed polymer flakes. Excitation is performed by an UV-LED and the fluorescence signal is measured simultaneously by means of a CCD-colour-camera and a spectrometer.

3.3 LIF method with dissolved dyes

The measurement technique developed in this thesis is intended to be used for simultaneous measurements of temperature and velocity fields around a growing vapour bubble in future experimental investigations. A preliminary analysis with a common 2-colour-LIF method (with dye dissolved in the fluid) is performed, to study the feasibility of this less sophisticated laser-based measurement technique, for the determination of temperature fields in the fluid around the vapour bubble. Similar problems are expected for the LIF with dissolved dyes and the particle-based method. Since the former is a well-established technique that has been studied intensely, it is a benchmark for the applicability of other optical measurement methods, such as the particle-based method described in present thesis.

In the following, only the development and application of the optical measurement method is described. The experimental setup which is used to generate and observe single vapour bubbles is illustrated in [53]. Furthermore, additional information about the experimental procedure and theoretical aspects of nucleate boiling can be found there.

3.3.1 Fluorescent dyes for 2-colour LIF in acetone

In most publications dealing with 2-colour-LIF in liquids, a mixture of rhodamine B and rhodamine 110 is used as LIF tracer. These dyes are suited for the use in water, while they cannot be used in acetone. However, acetone was defined as the fluid for the nucleate boiling experiments to ensure comparability with measurements performed by Knauer et al. [34] using Raman spectroscopy.

To investigate the temperature sensitivity of different dyes in acetone, the temperable copper block with optical access from three sides, as described in section 3.1.6, is placed in front of the spectrometer. The copper block is equipped with windows made of fused silica which is chemically resistant against acetone. Fluorescence is excited by means of an Nd:YAG-laser (532 nm) formed to a light-sheet analogously to section 3.1.2 and the emission spectra of the investigated dyes are recorded for different temperatures.

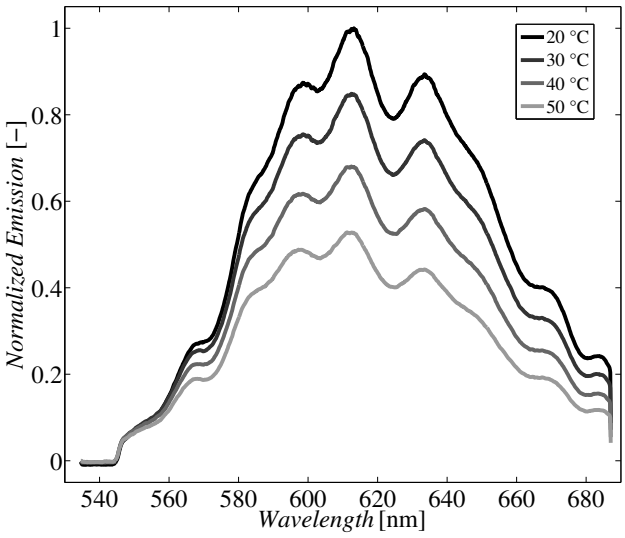

Figure 3.20: Emission spectra of DCM in acetone as a function of temperature.

Selection of temperature sensitive dye

As shown in [85] DCM[12] exhibits a temperature sensitivity in ethanol of -1.0 %/K. Based on this finding, DCM is dissolved in acetone and investigated with regard to its temperature sensitivity. From Figure 3.20 a clear temperature dependency can be recognized for the fluorescence of DCM in acetone. The emission peak of this solution is situated around 615 nm. The solution of DCM in ethanol, however, has an emission peak located around 570 nm. The increase of temperature sensitivity and the red-shift of emission when acetone instead of ethanol is used as a solvent can be attributed to the higher polarity of acetone leading to an elevated solvent relaxation.

Selection of reference dye

Rhodamine 19 (Rh19) was chosen as reference dye, because it is soluble in acetone and exhibits an emission peak that is recognizably shifted from that of DCM. The temperature sensitivity of Rh19 in acetone is small compared to that of DCM. The emission spectrum of Rh19 in acetone taken with the setup described above can be seen in Figure 3.21.

Fluorescence properties of the mixture of DCM and Rh19

The mixture of DCM and Rh19 in acetone ($C_{\mathrm{DCM}} = 1$ mg/l and $C_{\mathrm{Rh19}} = 1$ mg/l) exhibits an emission spectrum with a wavelength dependent temperature sensitivity, which can be observed in Figure 3.22. Two emission peaks can be recognized that can be assigned to the emission peaks of the respective single dye. The emission's dependency on temperature is small for shorter wavelengths and reaches its maximum at approximately 660 nm. Due to this characteristic spectrum, this mixture is well suited for the use in 2-colour-LIF measurements.

[12] 4-(Dicyanomethyl)-2-methyl-6-(4-dimethyl-amino-styryl)-4-H-pyran

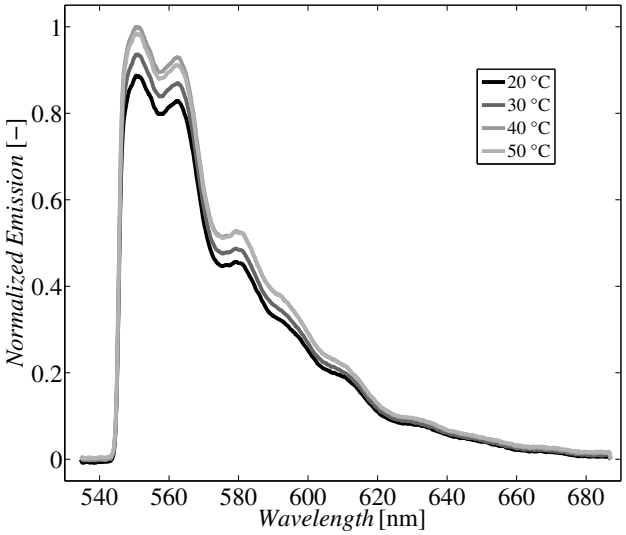

Figure 3.21: Emission spectra of Rh19 in acetone as a function of temperature.

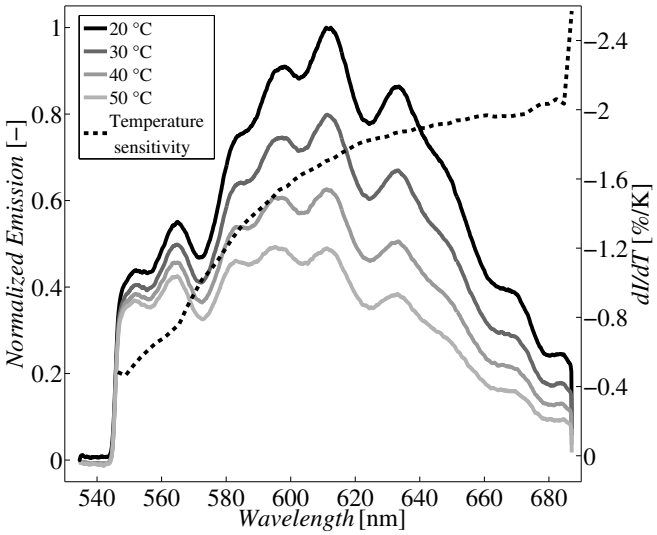

Figure 3.22: Emission spectra and the resulting wavelength-dependent temperature sensitivity for a mixture of DCM and Rh19 in acetone.

3.3.2 Optical setup

Due to the very similar emission spectra of the microcapsules (see section 3.1) and the mixture of DCM and Rh19 in acetone, the optical setup for fluorescence detection, as described in section 3.1.2, can be used without replacing the optical filters. As shown in Figure 3.23, the optical detection setup is mounted on one base plate that can be moved in all spatial directions by means of a translation stage and lifting screws. Hence, the field of view can be positioned exactly at the nucleation site. Additionally, the base plate can be inclined by means of the lifting screws, facilitating the regulation of the angle between the optical axis of the detection system and the heating foil. The dye mixture is excited using the Nd:YAG-laser with light sheet optics as described in section 3.1.3. The spherical convex lenses have an overall focal length of approximately 330 mm and the cylindrical concave lens has a focal length of −400 mm, which results in a height of the light sheet of approximately 8 mm. The laser beam is reflected towards the nucleation site by a mirror. Adjusting the mirror's inclination, the light sheet can be directed exactly at the growing vapour bubbles.

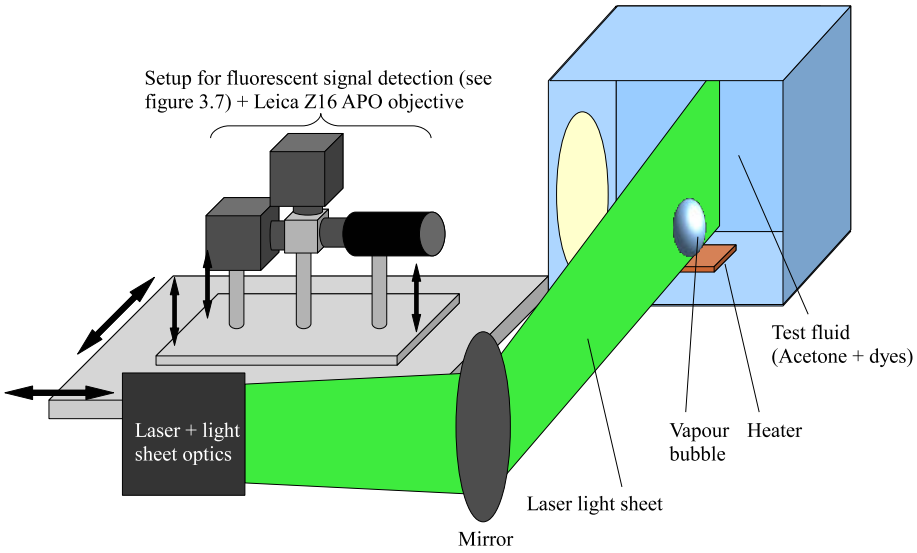

Figure 3.23: Schematic of the setup used for excitation and detection of fluorescence in acetone during nucleate boiling.

3.3.3 Experimental procedure

The concentration of DCM and Rh19 in acetone used for the nucleate boiling experiments is $C_{\mathrm{DCM}} = 6$ mg/l and $C_{\mathrm{Rh19}} = 13.8$ mg/l. Once nucleate boiling is activated at the designated position, the camera setup and the light sheet are adjusted such that the field of view matches the bubble position and the light sheet passes through the centre of the bubble that has a diameter of approximately 1.5 mm. In the following step, the inclination angle between the light sheet and the heater surface must be adapted carefully. On the one hand, the entire region around the bubble down to the bubble foot should be illuminated. On the other hand, the heat input on the heater surface by the laser must be kept minimal and so the incident angle must be chosen close to zero. If the heat input is too high, boiling is activated on the entire heater surface.

Due to the high frequency of bubble growth, an acquisition rate of 1000 Hz is needed, which is actually the maximum frequency that can be achieved with this measurement setup. After some image sequences

with some cycles of bubble growth in each sequence are successfully recorded, the heater is switched off and the in-situ calibration for this cycle is performed. The calibration has to be performed in-situ, since the ratio is influenced by many factors that might vary locally. During the calibration the temperature of the entire test cell is varied step-wise (2 K steps) and for each step a sequence of 50 image pairs is recorded. The calibration is performed after the measurements are finished, because once the heater is switched off, it is possible that the nucleate boiling cannot be re-activated at exactly the same position.

4 Data processing

The crucial measurand for all measurements presented in this thesis, is the fluorescence intensity in different wavelength bands. Because digital cameras serve as detectors, the data processing consists in large parts of image processing. Due to the big amount of measurement data (up to 50×10^3 pictures for one day of measurements), the computational time during data processing can increase dramatically, if the image processing algorithms are not programmed in an effective way. The reference temperature is detected by thermocouples, for which the data processing is not described here.

4.1 Image processing for microencapsulated fluorescent dyes

The main intention of described image processing procedure is the extraction of temperature information from the grayscale images of camera A and camera B. The variable containing the temperature signal is the ratio of fluorescent emission in the two spectral bands, as explained in 2.2.1. CamA detects the temperature-sensitive part of the emission spectrum, while CamB images the reference signal, to correct for variations of the absolute brightness. Due to the fact that temperature information is not available at all image positions, an exact correlation of congruent particles in ImageA and ImageB is fundamental. Otherwise the division of a section in ImageA in which a particle is present (high intensity) by a section in ImageB where no particle is present (low intensity) leads to a very high ratio and thus to an erroneous temperature. Figure 4.1 illustrates the process of the temperature and velocity fields evaluation.

The image processing procedure for temperature evaluation consists basically of the following steps:

- Matching of images from CamA and CamB,
- Evaluation of ratio-matrices from images,
- Temporal and spatial averaging of the ratio,
- Evaluation of calibration polynomials from steady-state temperatures,
- Evaluation of temperature fields from averaged ratio-matrices and calibration polynomials.

Depending on the particular setup and the actual images different possibilities for the determination of intensity information and calculation of the ratio are appropriate. For images with very high seeding density[1] the pixelwise division is applied, while for lower seeding densities particle detection is performed to derive the ratio-matrices from the images. For preliminary results further image processing methods that do not require the previous image matching, can be used. Each of the mentioned methods will be presented in more detail in the following sections.

It can be recognized from Figure 4.1 that the main effort is put in the evaluation of the temperature fields. This is due to the fact that the extraction of intensity information in ImageA and ImageB is much more complex than the determination of particles' displacement in subsequent images of the same camera. Nevertheless, the evaluation of velocity fields by means of PIV is explained in the last section.

[1] Seeding density in this context describes the quotient of pixels in the field of view showing a particle and those showing background.

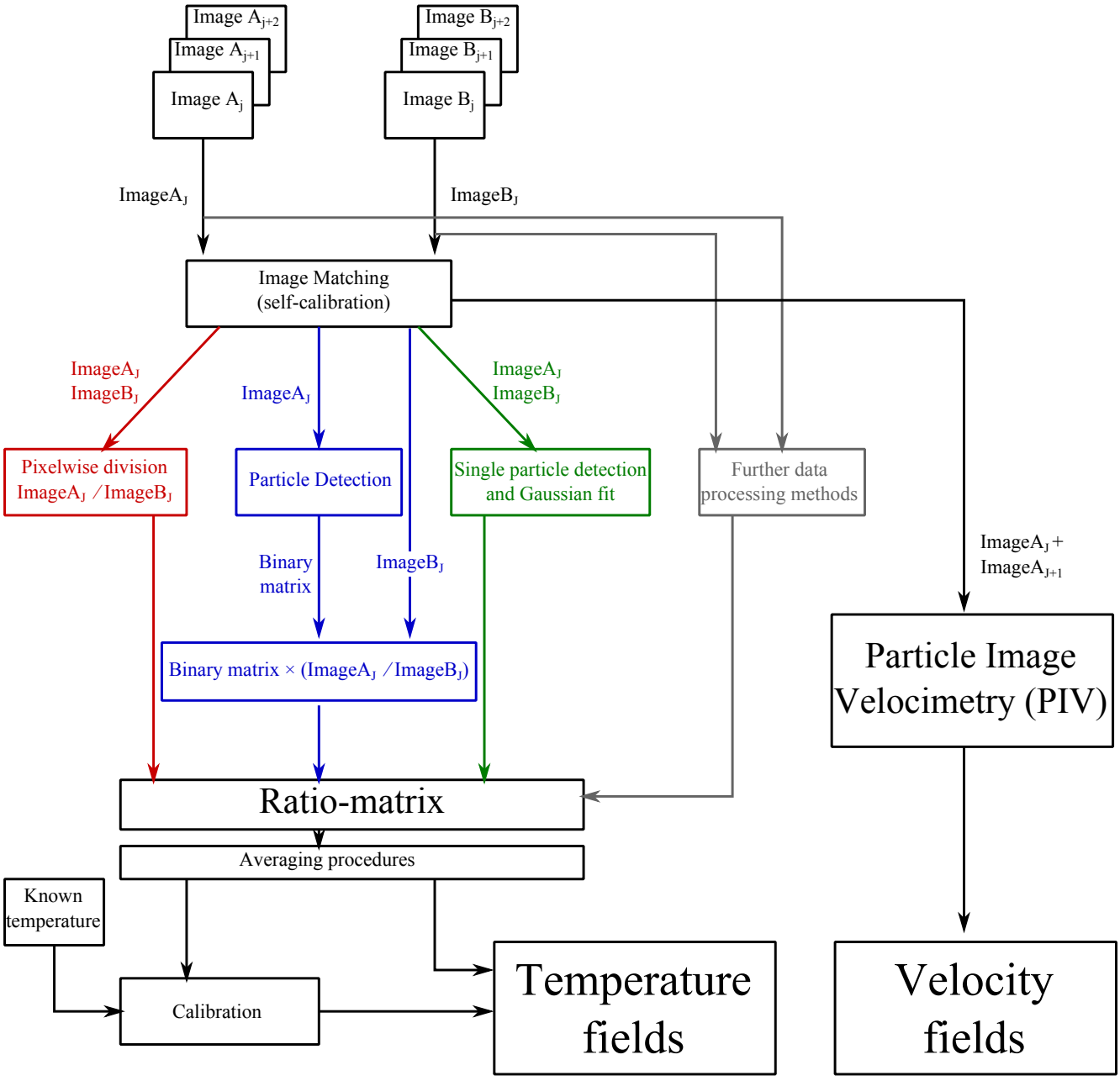

Figure 4.1: Schematic of the overall image processing procedure for the evaluation of 2-dimensional temperature and velocity information from the raw image data.

4.1.1 Image matching

It is essential that the pixel coordinates of each particle are the same for image A and image B. Otherwise, erroneous data will be generated for example when a bright pixel imaging a particle is divided by a dark pixel representing the background. Since the physical alignment of the cameras is insufficient, the images have to be matched in this post-processing step.

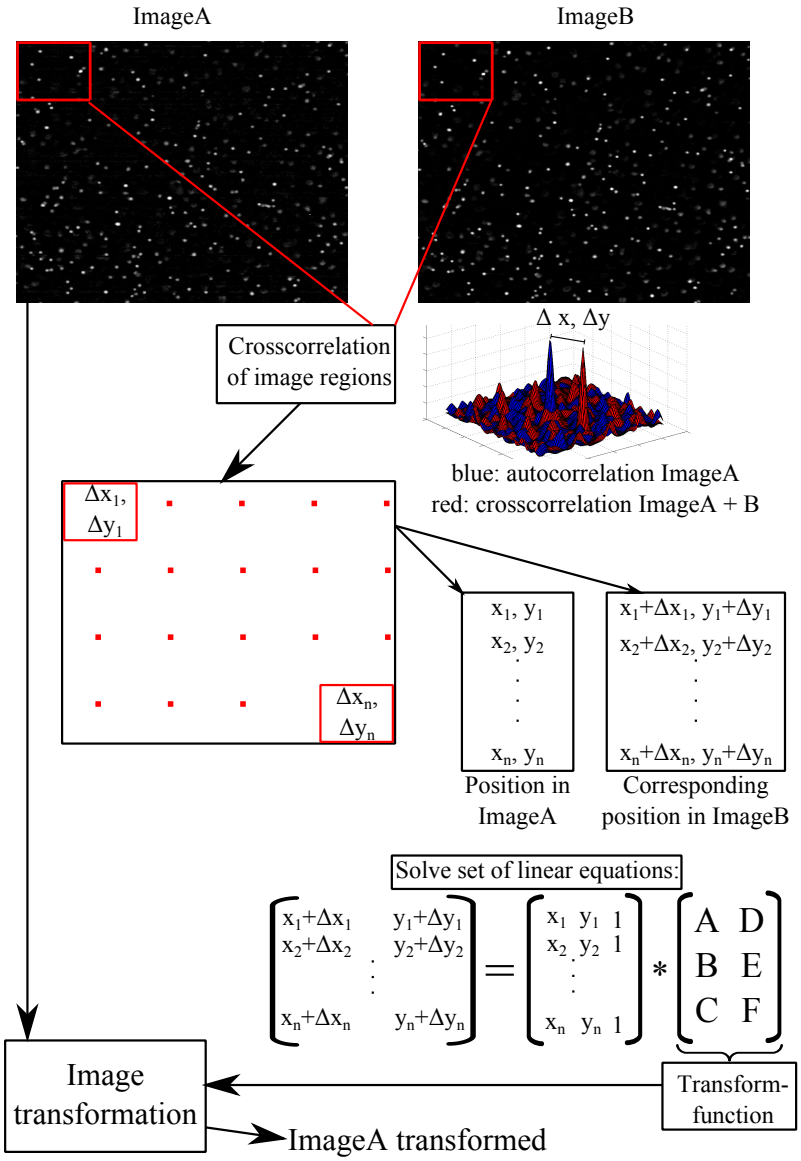

Figure 4.2: Schematic of the image matching procedure.

Image matching is performed according to a self-calibration approach, using the particle images themselves to identify the misalignment between the images of CamA and CamB. A similar approach is described by Wieneke et al. in [44] and [91]. They calculated the disparity between the two images of a stereoscopic PIV system, cross-correlating the particle images themselves. The resulting disparity map was used to correct possible differences between the position of the actual light-sheet plane and the calibration plate.

For the present case, the images of CamA and CamB taken at the same instant are also compared by cross-correlations. This happens, as displayed schematically in Figure 4.2 with the steps described in the following. First, the image is subdivided into regions (interrogation windows) such that each region

shows a distinctive particle pattern. Then, corresponding interrogation windows of ImageA and ImageB are cross-correlated and the displacement of the peak in the resulting cross-correlation matrix from the centre of this matrix is evaluated. This displacement represents the disparity of ImageA and ImageB in the particular region. The procedure of cross-correlation is the same as for the PIV-method which is described in section 2.3.

Actually the displacements are calculated using an open-source PIV-code (same as for the velocity determination, section 4.1.8) from simultaneous images of CamA and CamB, instead of subsequent images of a single camera. This procedure is repeated for all image regions resulting in a field that contains the displacement vectors for all regions. Thus, the positions of these regions in ImageA can be assigned to the corresponding positions of the same region in ImageB. This can be rewritten as a matrix operation as illustrated in Figure 4.2. Solving this equation results in the transform-function (matrix) that can be used to transform all images of CamA, so that they exactly match the images of CamB.

Since the displacement of ImageA and ImageB varies strongly in different image sections, the transform function is not calculated globally for the entire image as illustrated above. In fact, the image is again subdivided in triangles, each of them containing all points necessary to calculate a transform function. Thus, for each triangle a separate transform function is evaluated. The procedure of calculating the transform functions from a set of corresponding points in the images and the image transformation is implemented in the commercial software Matlab[2], which is used for data and image processing.

The displacement between the images depends, amongst others, on the optical magnification of the imaging optics. Furthermore, marginal changes in the optical setup cause a shift of the displacement. Thus, the transform-function must be evaluated for every series of measurements (measurement day) and additionally any time the magnification is changed. Of course, the image-transformation must be applied to every single image of CamA. Depending on the image quality, a background subtraction or other pre-processing steps might be necessary before the transform-function can be evaluated successfully.

Figure 4.3 displays the result of the previously described matching procedure. Both images show the contours of the particles detected in image B (red lines) superimposing image A. On the left side (before image matching, (a)) a significant displacement between the particles in image A and the superimposed contours of the particles in image B can be recognized. After the matching procedure this difference vanishes, as it can be recognized from Figure 4.3 (b).

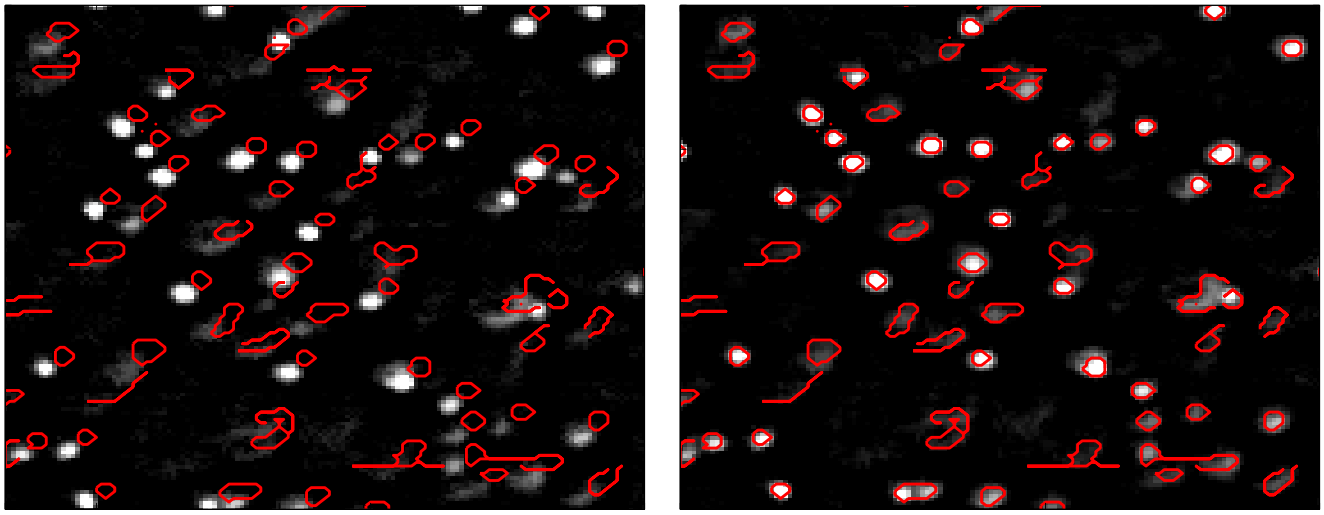

(a) (b)

Figure 4.3: Image A with superimposed contours of the particles detected in image B. Before (a) and after (b) the image matching procedure.

[2] *Mathworks Matlab v7.6.0*

The image matching procedure has to be performed as the first step of each image data processing. Depending on the particular application, different consecutive steps are realized as described in the following.

4.1.2 Pixelwise division

The pixelwise division of the images from CamB by the ones from CamA is probably the simplest way to obtain the temperature-sensitive ratio from the matched images. This procedure is applicable for images with a high seeding density of particles (low magnification, high concentration of particles in fluid) so that particles are very close to each other and the dark background is negligible.

In this procedure every single pixel in ImageB is divided by the corresponding pixel in ImageA. The resulting ratio is stored as one element of an array, corresponding to the respective pixel. This is repeated for all images of one sequence, resulting in an 3-dimensional array (see section 4.1.6). Consequently, such an array exists for every step of the calibration and for each measurement. This approach is applied to the measurements presented in section 5.1.4 and yields good results. In Figure 4.4 the effect of the pixelwise division can be recognized. While in (a) the particles can be clearly recognized as brighter pixels, the ratio in (b) shows a more homogeneous distribution and only some outstanding points can be identified in both images. It can be concluded that the image matching procedure described in section 4.1.1 works well and that the pixelwise division is an appropriate possibility to create the ratio. However, this procedure can only be used for images with a high seeding density. The next processing step is the averaging of the obtained data as described in section 4.1.6.

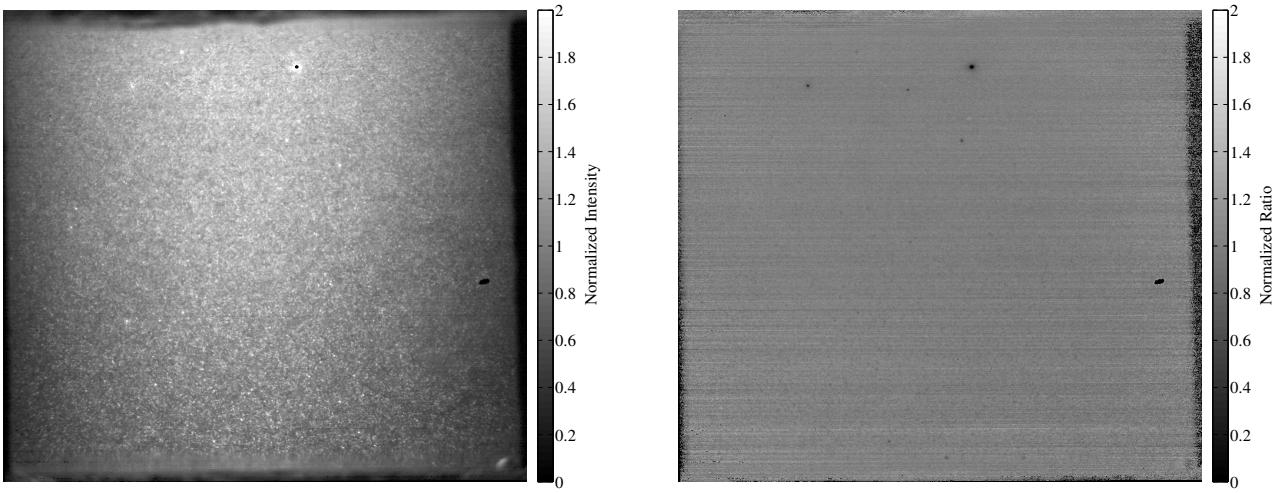

(a) (b)

Figure 4.4: Single image of CamA (a) and ratio matrix (b) calculated by pixelwise division of ImageB by ImageA. Since both images are normalized by the mean value of all pixels, the same scale is used to display them.

4.1.3 Particle detection

Since only the particle contain proper temperature information, it is necessary to separate the particles from the background. If the seeding density is low, more pixels displaying the background exist than pixels representing particles. This is relevant for high magnifications or low concentrations of particles

in the test fluid. It must be decided in the individual case, based on the respective images, whether the particle detection is necessary or not. Particle detection can be used to detect single particles as well as big, connected clusters of particles and is therefore very flexible in terms of applicability for different seeding densities. However, for some cases other methods of analysis, as described in section 4.1.2 and section 4.1.4, might yield better results.

For the present work, particle detection as described in this section is used for the measurements performed with the setup explained in section 3.1.6. In Figure 4.5 the process of particle detection is sketched.

The first step ((a) → (b)) is the background subtraction in the matched image of CamA. This step influences the overall intensity in the image. However, the ratio is not influenced by this step, as the ratio is calculated from the original, matched images of CamA and CamB. The background subtraction is necessary to get a more homogeneously illuminated image background which is prerequisite for the threshold filtering. Due to fluorescent light that is emitted outside of the focal plane, the background is not completely dark. On the one hand, this results from the thickness of the light sheet, which exceeds the depth of field of the used optics, causing out-of-focus particles to fluoresce. On the other hand, there are scattering and fluorescing (due to re-emission) particles along the optical path of the signal which causes diffuse light to reach the camera sensors. This results in local differences of the background intensity which hinders particle detection by means of a threshold filter. The background subtraction algorithm subdivides the image into sections that exceed the average particle diameter. The mean intensity of these sections represents the brightness of the background and is subtracted from the original image, offering a more homogeneous intensity distribution.

In the next step ((b) → (c)) a threshold filter is used to generate a binary matrix from the particle image. Therefore, a threshold value is defined from the mean intensity in the image. All pixels that show a value above this threshold are set equal to one and all other pixels are set equal to zero. Besides that, all objects in the binary image that are smaller in size than the average particle are removed. By this means, dark and blurred particles that are represented only by single pixels exceeding the threshold value are excluded.

The resulting binary matrix is used as template to create a matrix containing the ratio at particle positions and zero at all other positions, as shown in Figure 4.5 (f). Therefore the ratio-matrix (e) is generated by pixelwise division of the matched images of CamA and CamB. Every element of this matrix is then multiplied with the respective element of the binary matrix (either one or zero). From Figure 4.5 (e) it can also be seen that the ratio at background positions deviates strongly, while the ratio at particle positions shows less fluctuations. Hence, the necessity of particle detection for the processing of these measurements becomes clear.

This procedure is repeated for all image pairs of one sequence resulting in a 3-dimensional array. In the subsequent averaging procedure according to section 4.1.6 all elements containing zeros are neglected.

4.1.4 Single particle detection and gaussian fit

The single particle detection in combination with a gaussian fitting is used for images that show a very low seeding density. Every particle must be detected separately to allow the gaussian fitting. This requirement is met very well by the measurements described in section 3.1.5 and the results shown in section 5.1.5 are obtained with this method.

The entire procedure is shown in Figure 4.6. The image background displays fluorescence from particles behind and in front of the focal plane, which are illuminated by the laser beam. Background subtraction ((a)→ (b)) is performed by subtracting the subsequent image from each image. Doing so, the contributions from out-of-focus particles that can be seen as rings in (a) and (d) can be removed in large parts. This is due to the fact that the out-of-focus particles move comparatively slow, because the axial veloctiy decreases in radial direction in this setup. Thus, the displacement between subse-

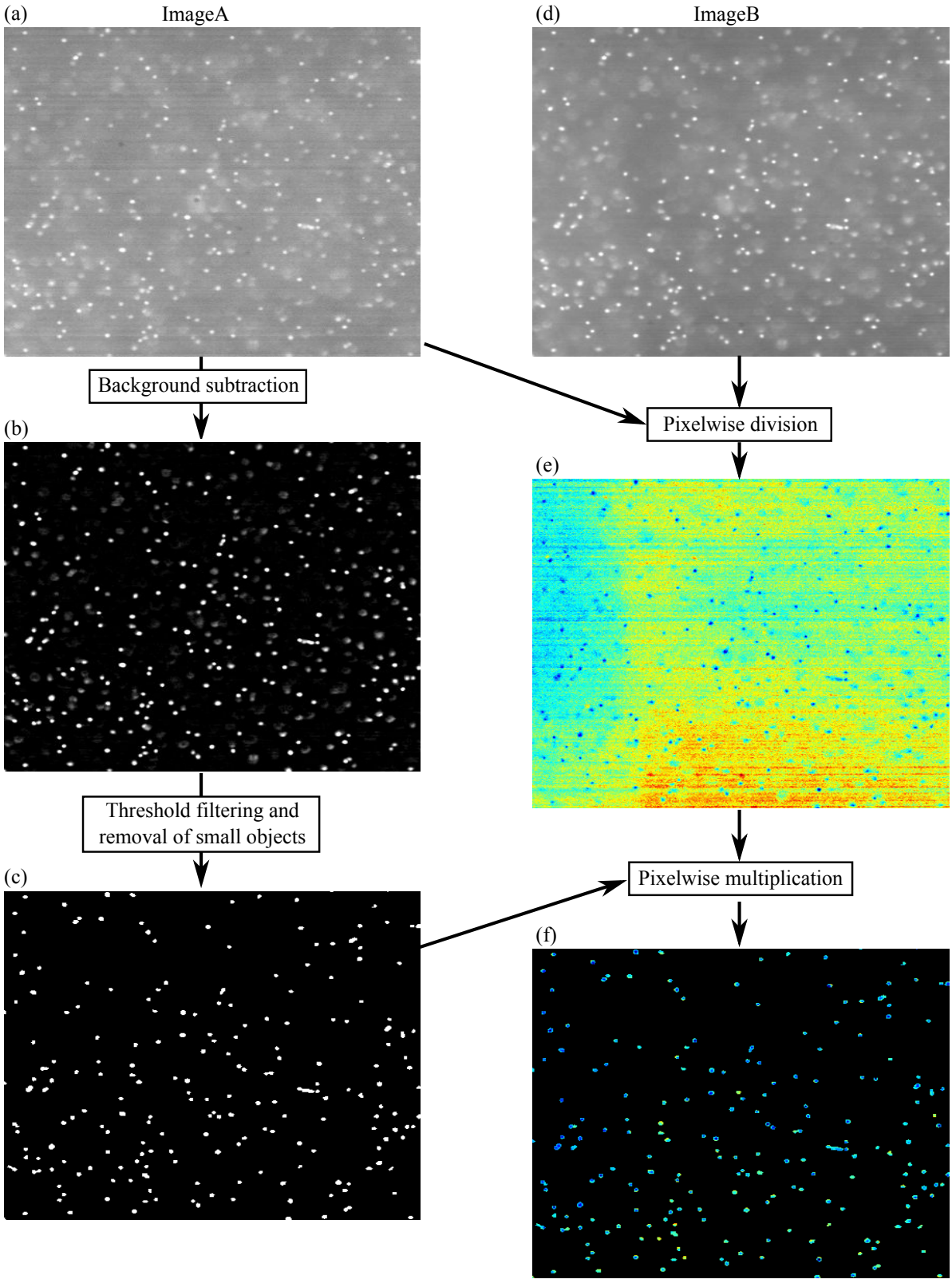

Figure 4.5: Procedure of particle detection. The matched image of CamA (a) is processed to create a binary matrix (c) containing ones at positions with detected particles and zeros at all other positions. This is used as template to create the matrix displayed in (f) containing zeros for the background and the ratio of ImageA and ImageB at particle positions (displayed in colour). The ratio for the entire image calculated by pixelwise division is shown in (e).

quent images is high for the in-focus particles and small for the out-of-focus particles. Other methods of background subtraction are also applicable.

In the next step ((b) → (c)) a threshold filter is used in combination with a geometrical filter (excluding objects that do not show form and size of a typical particle) to detect particles in the image. Then the position of the particle centers is extracted. To generate the binary image, an area of 6×6 pixels around the particles' centres is set to 1, while the rest of the matrix is 0. Analogously to the procedure in section 4.1.3, the binary matrix again serves as template. The matrices (e) and (f) in Figure 4.6 result from pixelwise multiplication of the binary matrix (c) with the images (a) and (d) respectively. Then a gaussian fit is applied to the single particles of these images. This fitting corresponds to an averaging procedure in the area, but additionally it takes advantage from the knowledge that the ideal image of a single particle is gaussianly distributed. The ratio of a single particle is calculated by dividing the fitted intensities of this particle. Applying the last two steps to all detected particles results in the ratio-matrix (g).

4.1.5 Further image processing methods without camera matching

Besides the above described methods that all need well matched images, there are further possibilities to extract the intensity information from the particle images without a previous image matching as illustrated in section 4.1.1. These procedures are based on subdividing the images into interrogation areas. The ratio is then evaluated either from the maximum values or the mean values of the respective areas in image A and B. Due to the displacement of the images that is not corrected, an error will be imposed. However, the effort for the processing is small compared to the methods described above and offers sufficient accuracy for preliminary results in most cases.

The methods are described in more detail in [43]. There they are also characterized in terms of accuracy and applicability.

4.1.6 Data averaging

Averaging procedures are applied to the sequences of ratio-matrices resulting from above steps. Temporal averaging takes into account mulitple (N) image pairs of one image sequence, while spatial averaging combines the ratio values in an area of $M \times M$ pixels to one single value. These averaging procedures are outlined in Figure 4.7. Their application reduces the spatial and temporal resolution of the measurement method, but enhances its precision. For that reason, it must be checked for each application, whether a higher degree of temporal averaging (e.g. for stationary measurements) or a higher degree of spatial averaging is more suitable.

In the first step of the averaging, the image is subdivided into interrogation windows. The arithmetic mean of all matrix elements in one interrogation window is taken as its value. However, matrix elements that are zero (no particle present) are not taken into account for the calculation of the mean value. In the next step temporal averaging is performed, taking the arithmetic mean of N interrogation windows at the same position of subsequent matrizes. The resulting mean values are written into the respective locally and temporally averaged matrix at the proper position. This step is repeated for all interrogation windows.

The averaging procedure itself is the same independent of the method used to evaluate the ratio-matrices and the application. However, as mentioned above, the parameters N and M are adapted to the actual measurements.

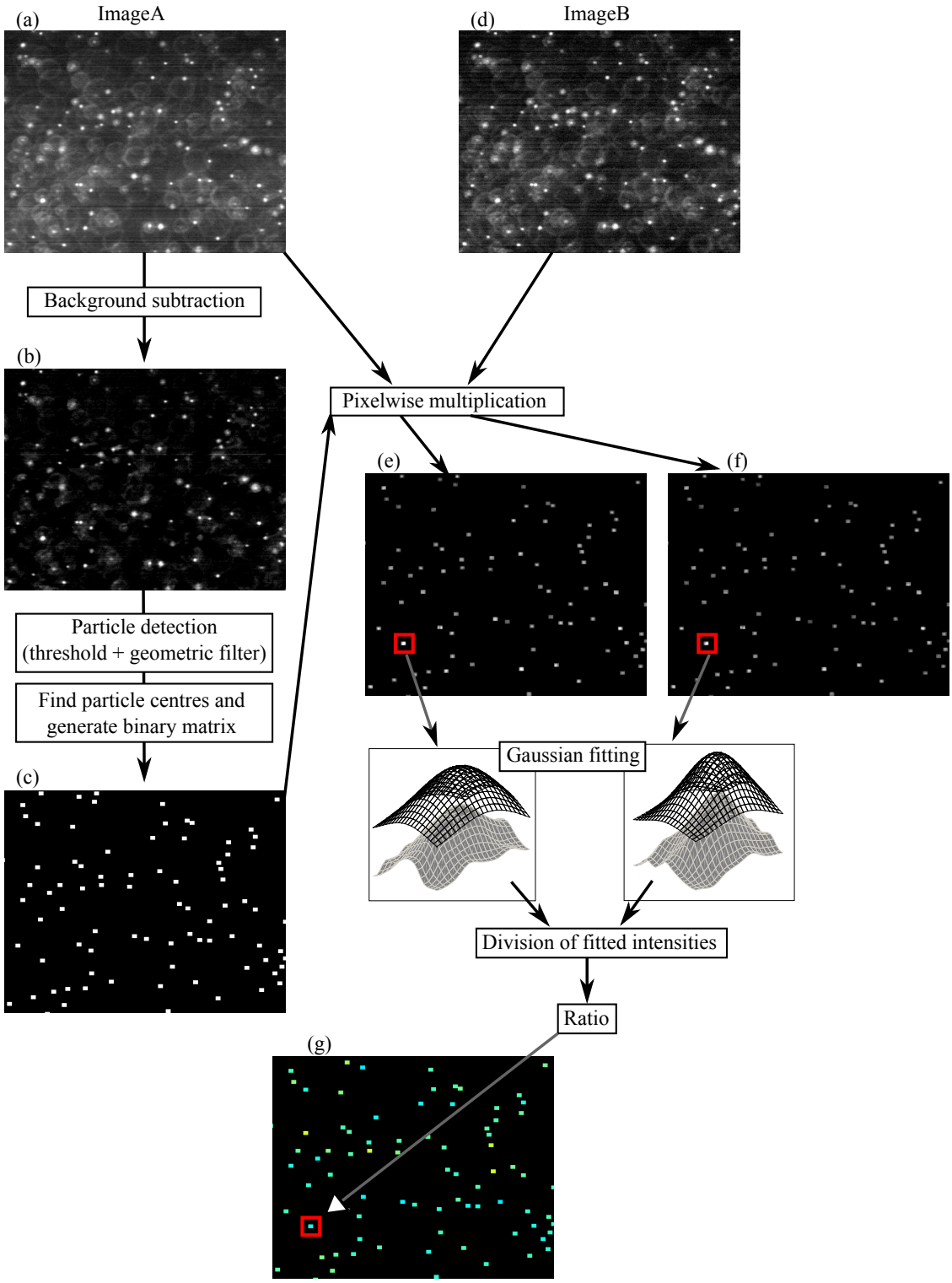

Figure 4.6: Procedure of image processing with particle detection and gaussian fitting. First a background subtraction is performed to remove out-of-focus particles (a)→ (b). Then a threshold filter in combination with a geometrical filter is used to detect the particles and generate a binary matrix (c) with ones at a 6 × 6 pixels area around the particles' centres. The binary matrix serves as template that is applied to (a) and (d) resulting in (e) and (f) showing only information at particle positions. A gaussian fitting is applied to every particle and its ratio is calculated and stored in the ratio-matrix (g).

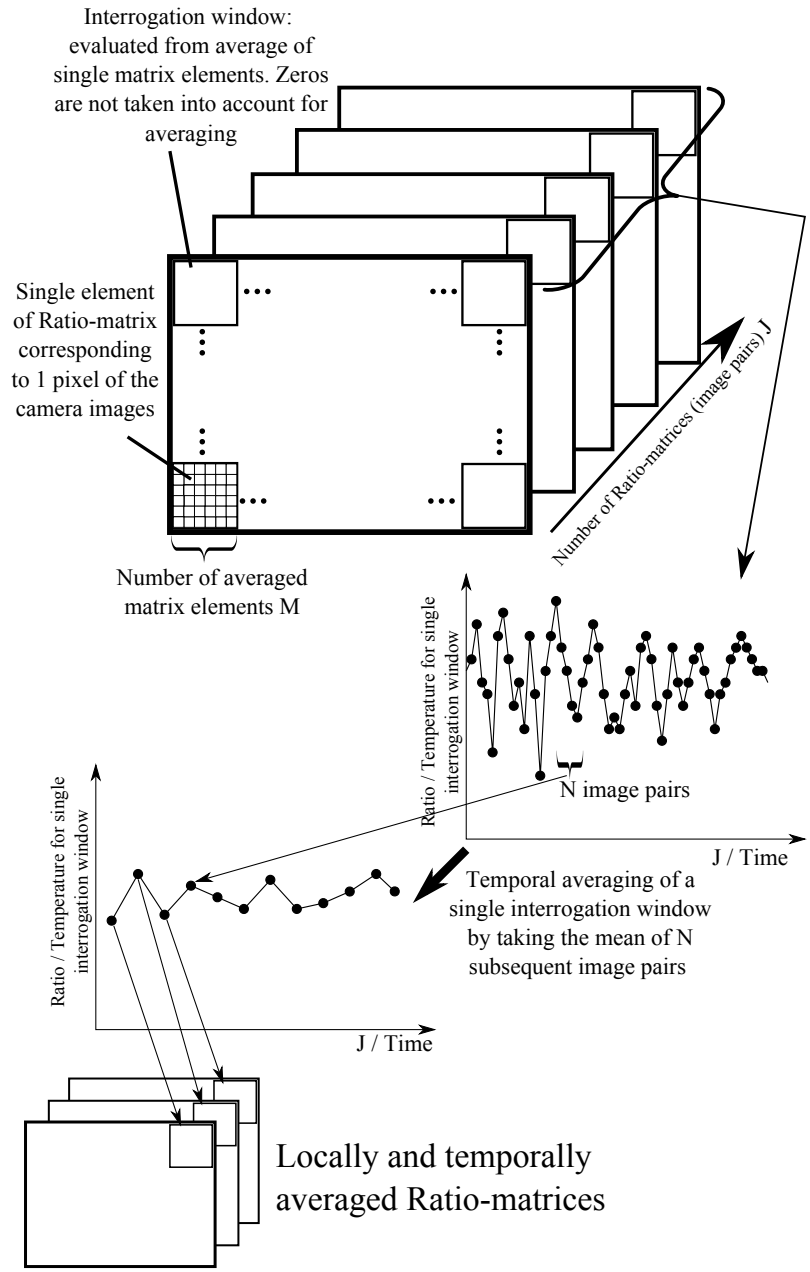

Figure 4.7: Illustration of the temporal and spatial averaging procedure for ratio-matrices obtained from previous image processing steps.

4.1.7 Calibration procedure

In the last step of the data processing, the 2-dimensional temperature distribution is derived from the averaged ratio-matrices and the respective calibration polynomials. An in-situ calibration is performed for all measurements presented in this thesis. That means that a calibration with homogeneous, known temperatures must be performed before or after the actual measurements and no modifications of the setup are allowed between calibration and the respective experiments. The in-situ calibration is necessary due to local differences of the ratio existing due to wavelength dependent optical effects (absorption, refraction) caused by optical elements along the path of the fluorescence signal. Also temporal effects like shown in Figure 5.22 can occur and must be taken into account during the calibration.

Before the evaluation of calibration polynomials, the images from the calibration measurements are also processed with the procedures described above. Since the temperatures during the calibration are stationary, a high degree of temporal averaging for the image sequences at each temperature step is intended. For the measurements described in section 3.1.5 500 images and for all other experiments 50 images were taken at each temperature step of the calibration. The same local averaging during the preparation of the ratio-matrices is applied to the calibration images and the images of the actual measurements.

Two possibilities exist for the calibration. A global calibration with a single calibration polynomial valid for all ratio-matrices and the local calibration with a specific polynomial for each interrogation window.

Although an exponential correlation between the ratio and the temperature results from the physical principle of LIF (see equation 2.6) which is used by other authors [10], [19], [42], first order polynomials are used for the calibration in this thesis. No systematic deviation of the measured temperatures from the linear approximation can be recognized, which is assumed to be due to the small temperature range.

Global calibration

In the global calibration procedure, one single calibration polynomial is evaluated and applied to all interrogation windows of the ratio-matrices.

In Figure 4.8 the process of global calibration starting from the ratio-matrices is shown in more detail. Local, stationary differences of the ratio are considered by a normalization. Therefore temporal averaging is performed using all ratio-matrices available from the calibration measurements and the resulting mean matrix is used for the subsequent element-wise division (normalization) of all ratio-matrices (from calibration and actual measurements). In the next step, a local averaging including all elements of the calibration matrices is performed for each temperature step resulting in a single correlation between ratio and temperature. This correlation is approximated by a linear fit. This polynomial is finally used for the calculation of temperature fields from the ratio-matrices of the actual measurements.

Local calibration

The local calibration procedure evaluates a particular calibration polynomial for each interrogation window of the ratio-matrices. The principle of the local calibration is sketched in Figure 4.9. For all ratio-matrices resulting from the calibration images, a separate correlation between ratio and temperature is evaluated and approximated by a linear fit. The polynomial coefficients for each interrogation window are stored in a calibration matrix, which is used to calculate the temperature fields from the ratio-matrices of the actual measurements.

As explained in section 5.1.6 ("error sources"), the temperature sensitivity can be smaller for very dark regions in the image, than for other areas. Such effects of locally different temperature sensitivities can

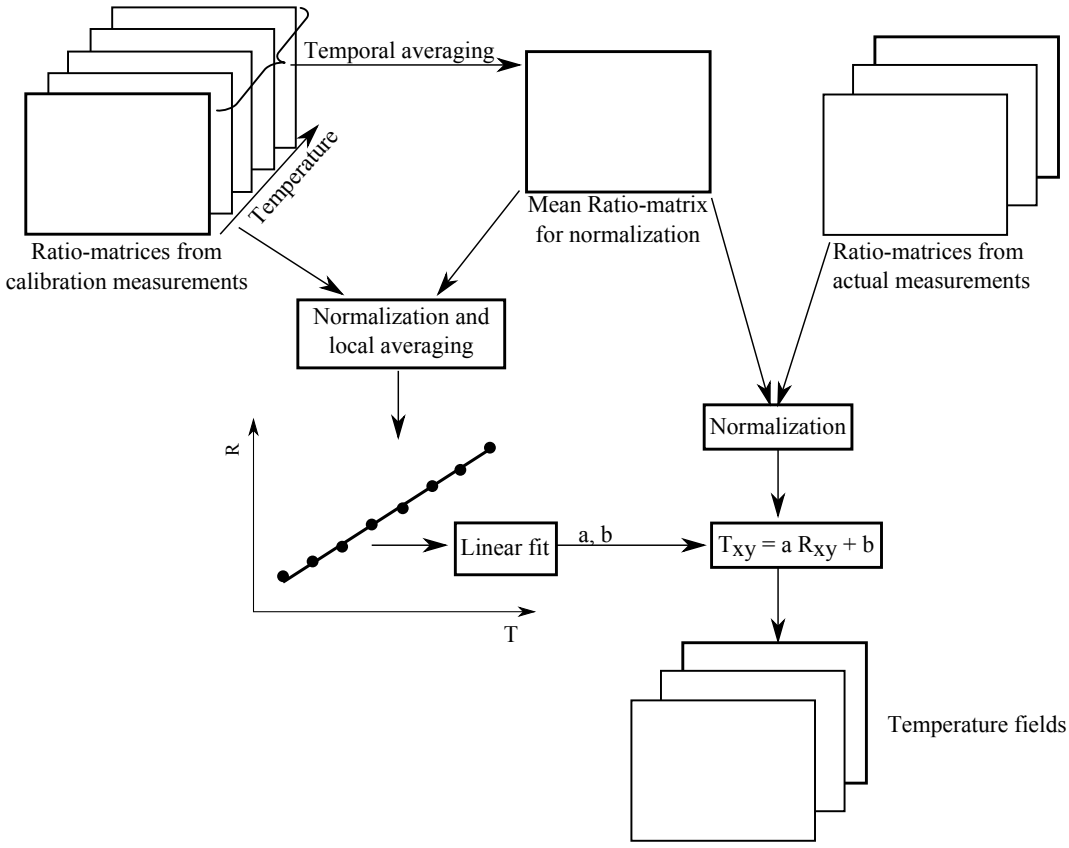

Figure 4.8: Schematic of the global calibration procedure. A mean ratio-matrix is evaluated from the calibration measurements and used for normalization of measurement and calibration ratio-matrices. The local mean value of the calibrations is used to derive a single, linear calibration polynomial. With this, measured ratio values are assigned to the appropriate temperature values resulting in the temperature fields.

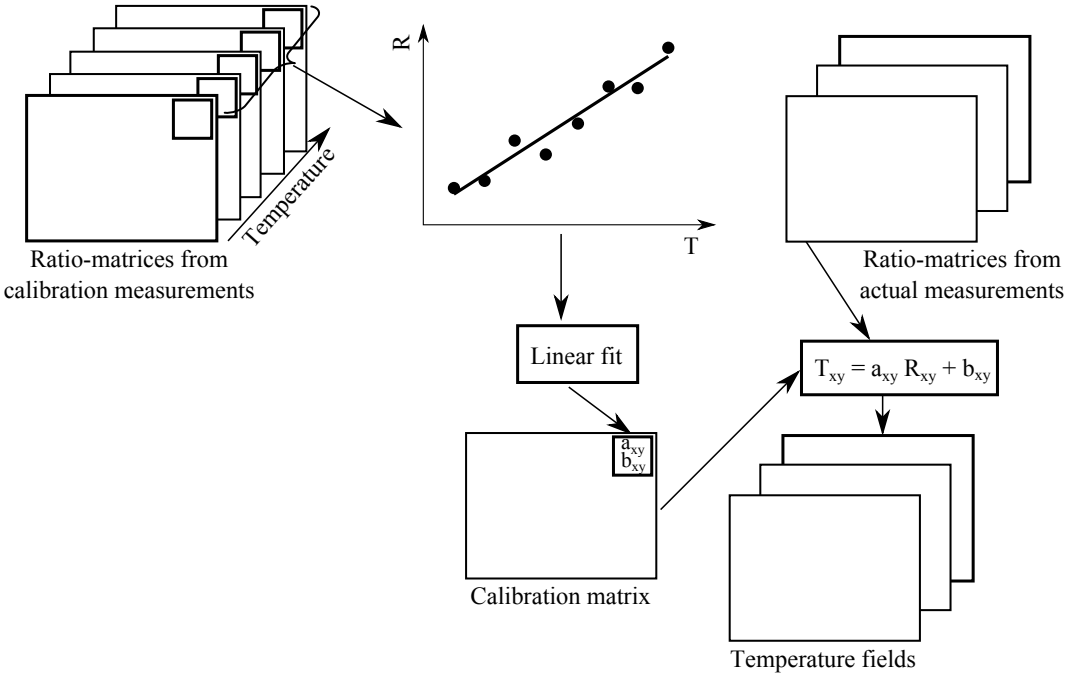

Figure 4.9: Schematic of the local calibration procedure. In contrast to the global calibration, this procedure does not include a normalization step. Local variations of the ratio are considered by evaluating a local calibration polynomial for each interrogation window and calculating the temperature for every interrogation window accordingly.

only be taken into account with a local calibration (provided that the local intensity distribution in the images remains constant during calibration and actual measurements).

Comparison of local and global calibration

Both calibration methods were exemplarily applied to all presented measurements and the results did not show a significant difference. For the result presented in Figure 5.12 with remarkable differences between measurement and simulation at the edges and a low signal-to-noise ratio (SNR), an increased accuracy at these positions is expected for the local calibration. However, the local calibration does not yield better results, even for this case. The high variance of the ratio at these positions, leads to errors during the polynomial fit for the single interrogation windows.

The global calibration offers a reduced computational effort compared to the local calibration, for which numerous polynomial fits must be performed. For that reason all results presented in this thesis were evaluated using a global calibration procedure.

4.1.8 Determination of velocity distributions

For the determination of velocity fields open-source PIV-software[3] is used. This program is based on Matlab and uses the cross-correlation method described in section 2.3. Some additional features are available in this program, such as "window-shifting" to enhance the accuracy of the velocity determination.

[3] MatPIV, Version 1.61

4.2 Image processing for dyed polymers

For the processing of the images resulting from the measurements described in section 3.2.1 no particular procedure is necessary. Some of the algorithms presented in the previous section are used. The methods used for the respective measurements are described together with the results in section 5.2.

4.3 Image processing for LIF with dissolved dyes

Image processing for the measurements using 2-colour-LIF with dissolved dyes (see section 3.3 and 5.3) is performed analogously to the image processing for microcapsule measurements (see section 4.1).

The image matching (analogously to section 4.1.1) for this case must be performed with separate images of a structured test array, since the images of the actual measurements do not exhibit particle patterns. These images must be taken after the experimental series are completed. The image processing must be performed separately for each series of experiments, since the evaluated transform function is only valid as long as the optical setup remains unchanged, which is not the case for different series of measurements. For the presented experiments a pattern with randomly distributed black and white spots, plotted on paper, is used as a test array.

The temperature-dependent ratio is calculated using the pixelwise division as described in section 4.1.2. The resulting ratio-matrices can only be locally averaged, since the frequency of bubble growth is such high that a whole cycle can only be resolved with approximately 15 images. Although 1000 images per second are acquired, the measurement frequency leaves no buffer for additional temporal averaging.

For the assignment of temperatures to the respective ratio, a global calibration analogously to that described in section 4.1.7 is performed.

5 Results

5.1 Microencapsulated fluorescent dyes for temperature measurements

This section presents the results from temperature and velocity field measurements that have been obtained using microencapsulated fluorescent dyes. Their development and characteristics are described in detail in section 3.1. It is also shown that these microcapsules are applicable for 2-dimensional temperature and velocity measurements using different setups. Moreover, the method is characterized and compared to other measurement techniques.

5.1.1 Numerical simulations

Measured results in the following sections are compared to numerical simulations, for both, the flow driven by natural convection (section 3.1.4, called "convective flow" in the following) and the flow inside the heated capillary tube (section 3.1.5, called "capillary flow" in the following). Both phenomena are steady-state, laminar, incompressible and show no phase-change. Since the flows are stationary and laminar, no time-resolved simulations have to be performed and no turbulence-model is needed. Commercial software[1] is used for modeling, meshing and solving in the numerical analysis. All equations needed to solve this problem are implemented in this software [14].

The software uses the following equation:

- Heat transfer in fluid for steady state problem without heat source/sink (Energy conservation):

$$\rho c_p \vec{u} \nabla T = \nabla \cdot (\kappa \nabla T)$$

- Conservation of mass for steady state problem:

$$\nabla \cdot (\rho \vec{u}) = 0$$

- Conservation of momentum for steady state problem, compressible flow, gravitational forces and Newtonian-Fluid:

$$\rho(\vec{u} \cdot \nabla)\vec{u} = \nabla \cdot \left[-pI + \mu(\nabla \vec{u} + (\nabla \vec{u})^T) - 2/3\mu(\nabla \cdot \vec{u})I \right] + \rho g$$

All material properties are provided by an internal data base in the software. There the density ρ, the dynamic viscosity μ, the thermal conductivity κ and the heat capacity c_p are available as a function of temperature. As the natural convection is provoked by a temperature induced density gradient, this is prerequisite for the simulation of the convective flow. For the capillary flow, pure glycerol has been used as fluid, so μ, ρ, κ, c_p can be directly taken from the database values of glycerin. Experiments for the natural convection are conducted with a mixture of glycerin and water. Hence, material properties for this mixture have to be applied. Experimental data for a 30.5 % weight Glycerin/water mixture at 20 °C, 30 °C and 40 °C are taken from [83] and linearly interpolated for temperature and the exact mass ratio.

[1] Comsol Multiphysics v4.2

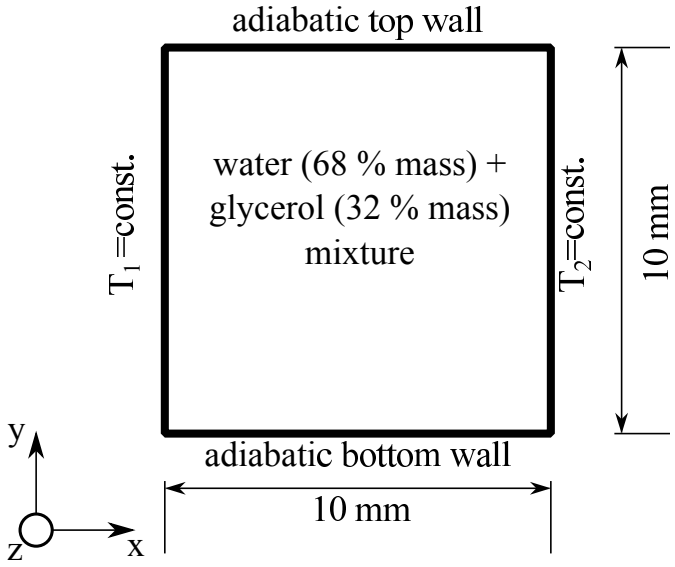

Figure 5.1: Geometry and boundary conditions for simulation of convective flow.

5.1.2 Numerical simulation of natural convection

For the measurements it is assumed that the temperature gradients along the z-direction can be neglected and thus a 2-dimensional simulation can be used to model the experiments. The geometry and the boundary conditions applied to the model are illustrated in Figure 5.1. The constant temperatures applied to the side walls (T_1, T_2) correspond to the measured temperatures (measured by thermocouple soldered in the tempered copper block) during the respective experiments.

5.1.3 Numerical simulation of capillary flow

The capillary flow is simulated by a 2-dimensional, rotationally symmetric model that is shown in Figure 5.2. Only the second copper block (in flow direction after the PTFE insulation) is modeled and the temperature profile at the inlet is assumed to be homogeneous and equal to the temperature measured by TC_2. This is a valid assumption, as theoretical considerations (see also section 3.1.5) and preliminary numerical simulations (for different flow-rates and outer glycerol temperatures) showed.

The Reynolds number Re for the flow in the capillary is calculated to be below $Re = 0.024$. Thus, the flow is laminar in any case and a Hagen-Poiseuille flow profile establishes. According to the law of Hagen-Poiseuille [76], the pressure difference Δp along the length of the capillary tube l can be expressed by

$$\frac{\Delta p}{l} = \frac{8\mu\dot{V}}{\pi R^4} \tag{5.1}$$

with the dynamic viscosity μ, the flow rate $\dot{V}$ and the radius of the capillary R. The force F_p on a fluid element with length L caused by the pressure difference along the capillary is

$$F_p = \frac{\Delta p}{l} L^3$$

The force F_b on the same fluid element caused by buoyancy (gravitational acceleration g) is

$$F_\mathrm{b} = \Delta\rho \cdot g L^3$$

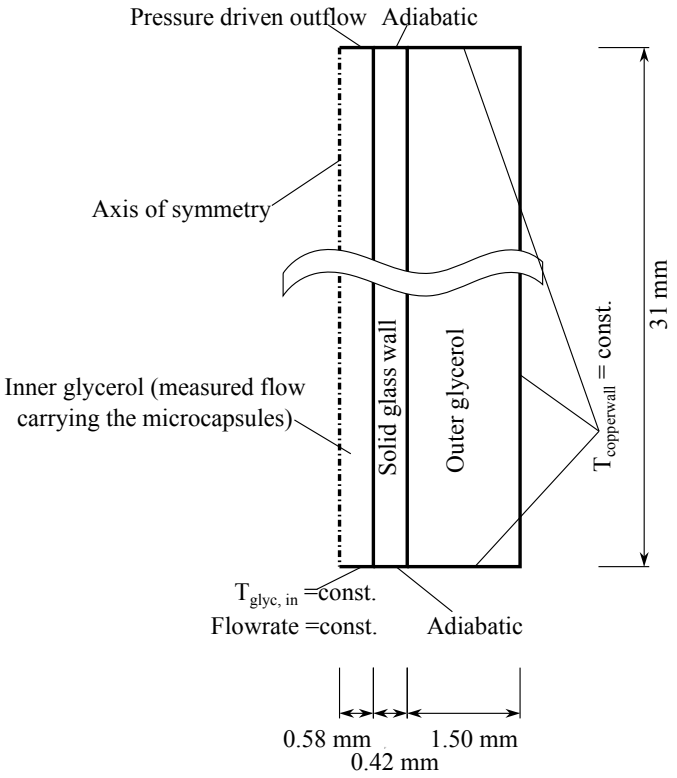

Figure 5.2: Geometry and boundary conditions for simulation of capillary flow.

The quotient of F_b divided by F_p is calculated to be 0.018 at maximum and therefore buoyancy forces can be neglected and the assumption of symmetry along the rotational axis of the capillary tube is valid.

Strictly speaking, this model is only valid, if the outer glycerol is contained in a second concentric tube with a constant wall temperature. For the experimental setup used, this is not the case, because the cavity that contains the outer glycerol has a rectangular shape and the glass slide surely has a different temperature than the copper block. Nevertheless, a good agreement can be found between the temperatures measured by TC_2 and the simulated temperatures at the corresponding position. This result is illustrated in Figure 5.3. From the maximum deviation between measured and simulated temperature in the outer glycerol of 0.8 K, it can be stated that the error resulting from the simplified model is of minor relevance for the comparison of simulation and measurement (measurement and simulation have a mean deviation ranging from 0.2 K to 1.6 K (see table 5.2) anyway).

The inlet temperature of the glycerol flow $T_{glyc,in}$ is taken from the measurements of the thermocouple TC_2 (as shown in Figure 3.14). The temperature of the copperblock ($T_{copperwall}$) is equal to the temperature of the water coming from the bath thermostat. The flowrate at which the glycerol enters is calculated from the volumetric flow that can be set at the syringe pump.

5.1.4 Results of natural convection experiments using light sheet illumination

The results presented in the following are obtained from measurements using the setup described in section 3.1.4 by means of the image processing described in section 4.1 using the approach of pixelwise division of the images from CamA by the ones of CamB. These experiments are performed to demonstrate the applicability of microcapsules for temperature and velocity measurements with light sheet illumination perpendicular to the viewing axis. To prove the correctness of the measured data, a numerical simulation (section 5.1.1) is performed and compared to the experimental results.

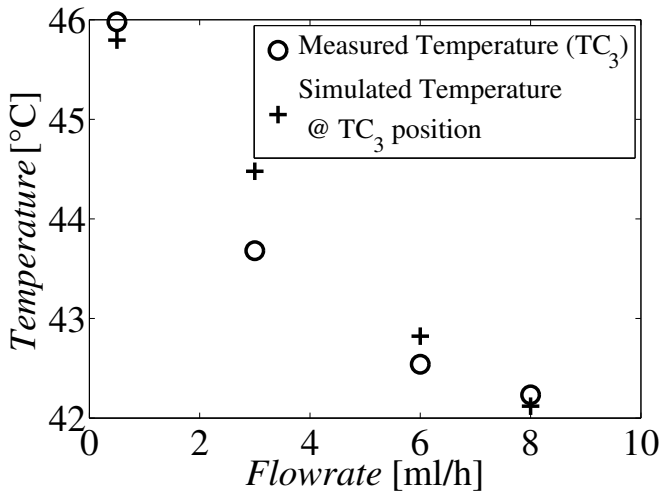

Figure 5.3: Comparison of temperature measured by one thermocouple in the outer glycerol and the simulated temperature at the position where the thermocouple is located.

Images illuminated with multiple laser pulses

The results presented in this section are obtained from images that are illuminated with multiple laser pulses. This means that the displacement of one particle in the time between two laser pulses must be significantly smaller than 1 pixel. The multiple illumination is a reasonable possibility of increasing the brightness of the particles appearing in one image and thus improving the SNR.

In Figure 5.4 ($N = 1$) the temperature profile evaluated from a single image pair can be seen. The local temperature deviations are quite high. As the observed flow is steady-state, temporal averaging can be performed by taking the mean of the ratio at one position in a sequence of image pairs (N = number of image pairs in the sequence). In Figure 5.4 it is illustrated that the local deviations in the temperature field reduce with increasing number of image pairs N.

Further reduction of temperature deviations can be achieved by local averaging. This is performed for the data presented in Figure 5.5, while no temporal averaging is performed ($N = 1$). The increase of M results in a decrease of temperature deviations and thus a higher precision of the measurements.

A more detailed description of the spatial and temporal averaging procedure can be found in section 4.1.6.

For each interrogation window a vector is build according to the procedure illustrated in Figure 4.7 that contains the temperature of the corresponding region for all considered image pairs. To quantify the influences of temporal and spatial averaging on the measurement accuracy, the standard deviation σ for each of these vectors is calculated. The standard deviation represents the mean deviation of the single measurement points from the average of all points. Thus, it is a measure for the precision of the measurement technique. In Figure 5.6 the resulting σ is shown for different sizes of the interrogation windows (M), over the number of subsequent image pairs (N) that were taken into account for the temporal averaging. The standard deviation presented here is calculated as the average σ of all interrogation windows. It can be seen from Figure 5.6 that the standard deviation decreases with increasing spatial and temporal averaging.

Additionally, the expected diminution of σ_{expected} for temporal averaged data, in the case of $M = 1$, is printed as a broken line. This characteristic is calculated from $\sigma_{\text{expected}} = \sigma(M = 1, N = 1)/\sqrt{N}$, which would be valid if the images in a sequence were statistically uncorrelated. As the actual curve is

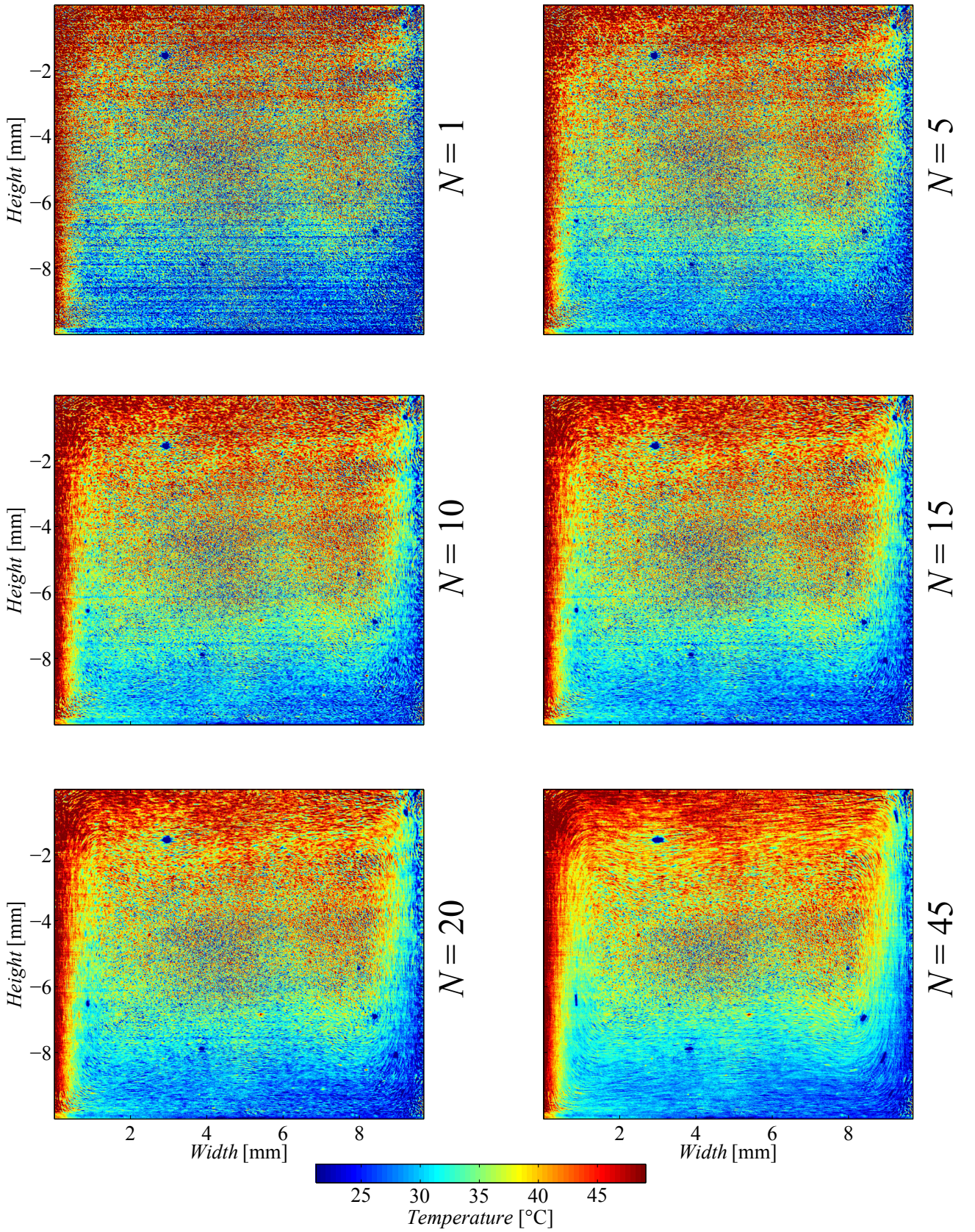

Figure 5.4: Temperatures fields from measurements of convectice flow for different degrees of temporal averaging and constant local averaging.

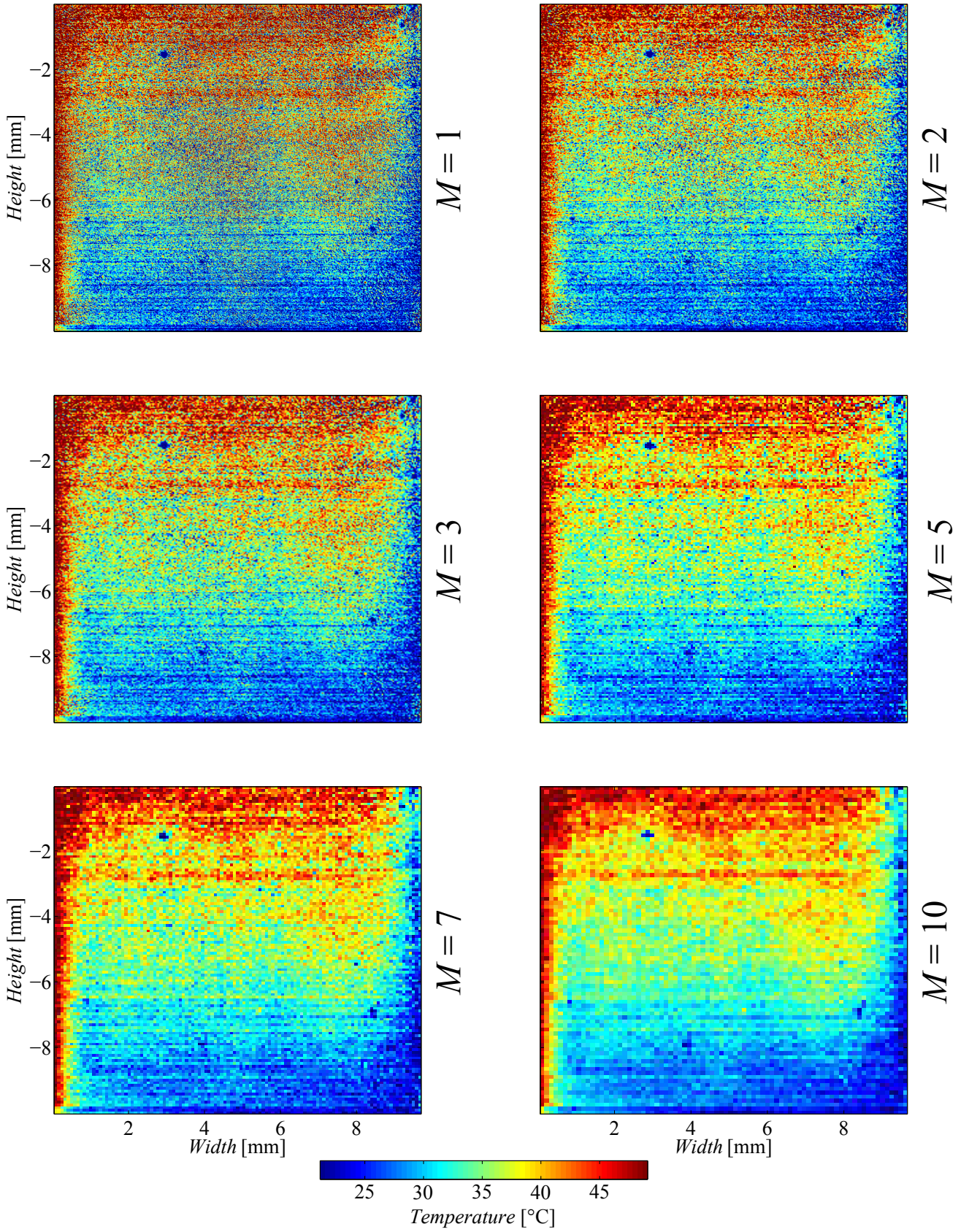

Figure 5.5: Influence of the local averaging ($M \times M$ pixels) on the measurement precision. The measurement precision increases for bigger interrogation areas, while the spatial resolution decreases. Presented data is evaluated from one single image pair (no temporal averaging is performed).

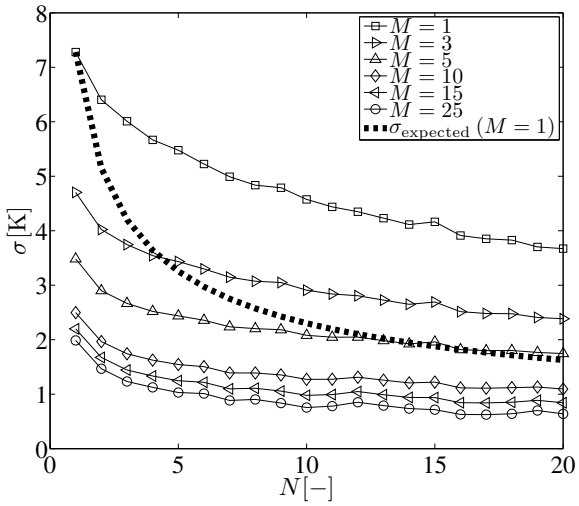

Figure 5.6: Influence of temporal and spatial averaging on the standard deviation of evaluated temperatures.

remarkable different from the expected one, this suggests that the images are correlated. This will be analyzed in more detail in section 5.1.6.

From Figure 5.6 a local averaging of 5 pixels ($M = 5$) and a spatial averaging of 5 image pairs ($N = 5$) appears to be a good compromise between precision and resolution. Applying these averaging procedures results in a temporal resolution of 33 ms and one point in the resulting temperature field corresponds to an area of 60 × 60 μm^2 in the measurement plane.

The temperature field displayed in Figure 5.7 (a) is evaluated that way and compared to the results of a numerical calculation (Figure 5.7 (b)). The velocity fields for both cases are displayed as arrows. Their lengths indicate the absolute value of the velocity. A more detailed comparison of the velocity fields can be found in Figure 5.11.

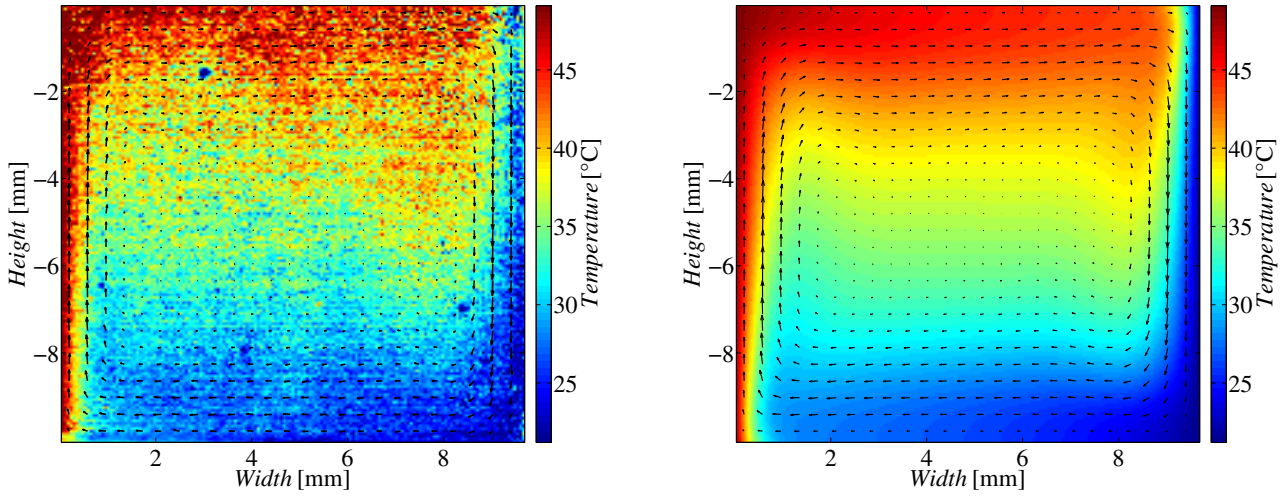

(a) Measurement (b) Simulation

Figure 5.7: Comparison of measured (a) and simulated (b) temperature and velocity fields for a flow driven by natural convection.

Qualitatively, the temperature fields shown in Figure 5.7 are in good agreement. To quantify their accordance, the number of data points of the numerical result is adapted to be congruent with the experimental data and the resulting matrix is subtracted from that containing the experimentally evaluated temperatures. The difference between measurement and numerics calculated in that way can be seen in Figure 5.8.

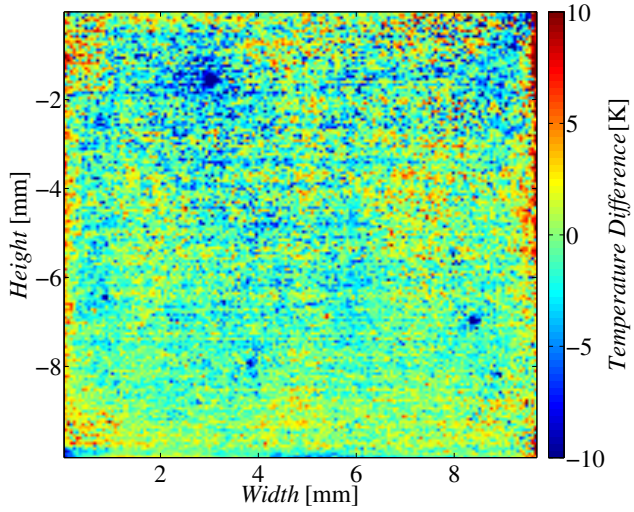

Figure 5.8: Difference between measured and simulated temperature fields for the convective flow.

In the bulk of this array the residual is equally distributed, suggesting that the developed measurement technique is capable of measuring temperature fields in fluids and the deviations arise basically from statistical fluctuations. Even though steep temperature gradients are present at the right and the left edge of the natural convective flow, the deviation is only slightly higher.

From the data presented in Figure 5.8, the 95 %-confidence interval, that characterizes the absolute measurement uncertainty for this case, is calculated. The 95 %-confidence interval must be chosen such that 95 % of all measured values show an absolute deviation from the numerical solution smaller than the half-width of this interval. An average 95 % confidence interval of ±6.0 K is determined by the calculation of residuals for multiple image sequences of different measurements.

The mean deviation of temperature and simulation for one whole field measurement is calculated by taking the arithmetic average of all points in the temperature difference array shown in Figure 5.8. This average value is computed for many different image sequences of different measurements that are equally processed ($M=5$, $N=5$). From Figure 5.9 it becomes clear that the mean deviation is also fluctuating around zero. This indicates that the mean deviation arises mainly from statistical errors. Thus, it can be concluded that bias errors are insignificant for this series of measurements.

Figure 5.10 displays the temperature profiles in vertical and horizontal direction for the measurement and the simulation shown as a temperature fields in Figure 5.7. A good agreement can be found for all horizontal temperature profiles at different vertical positions of the test cell (a) and for the temperature profile along the vertical axis (b). Thus, it is again confirmed that the simulation results can be reproduced well by the measurements. The statistical error, however, is quite high.

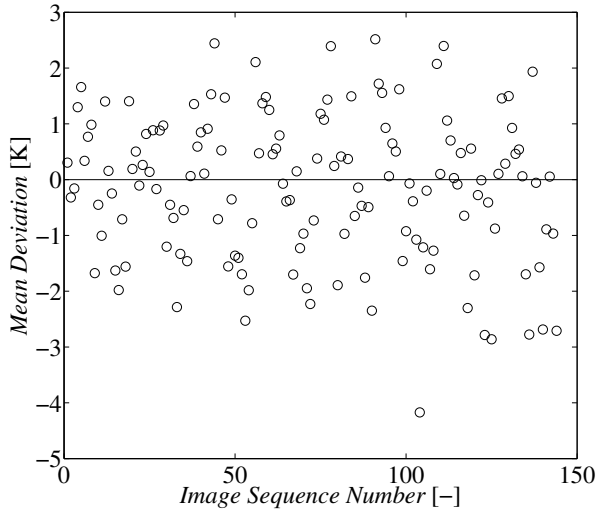

Figure 5.9: Mean deviation between simulation and measurement for different image sequences. Each point is evaluated from the average value of the respective temperature difference field, as shown in Figure 5.8.

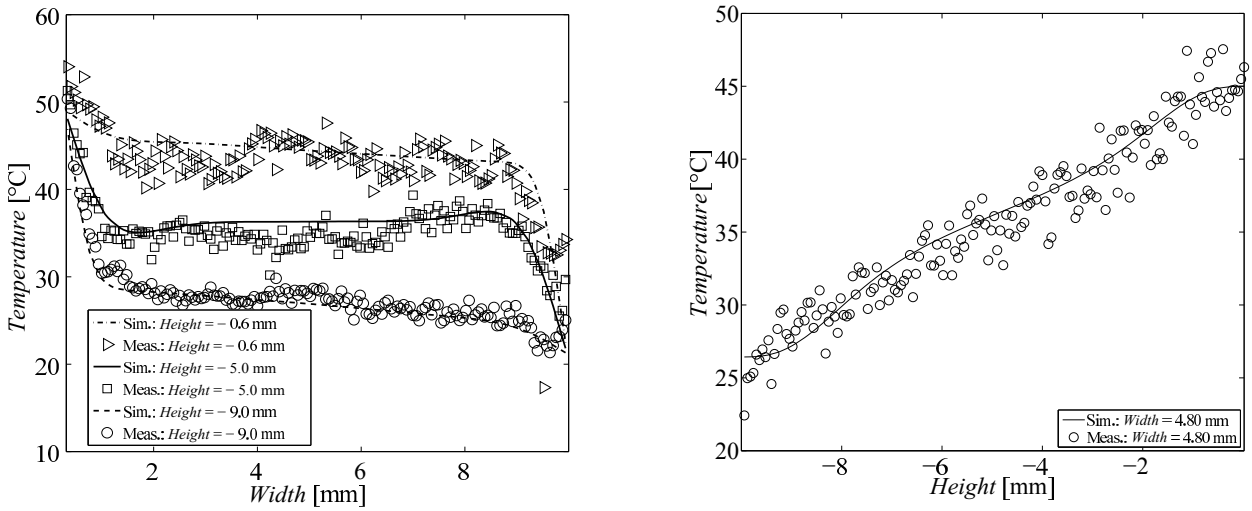

Figure 5.10: Comparison of measured and simulated temperature profiles for a flow driven by natural convection. In (a) the temperature profile in horizontal direction is shown for $Height = -0.6$ mm, $Height = -5.0$ mm, $Height = -9.0$ mm. In (b) the temperature profile in vertical direction is shown for $Width = 4.80$ mm. Data is evaluated for M=5, N=5 with additional averaging over 5 interrogation windows in vertical direction (a) and horizontal direction (b).

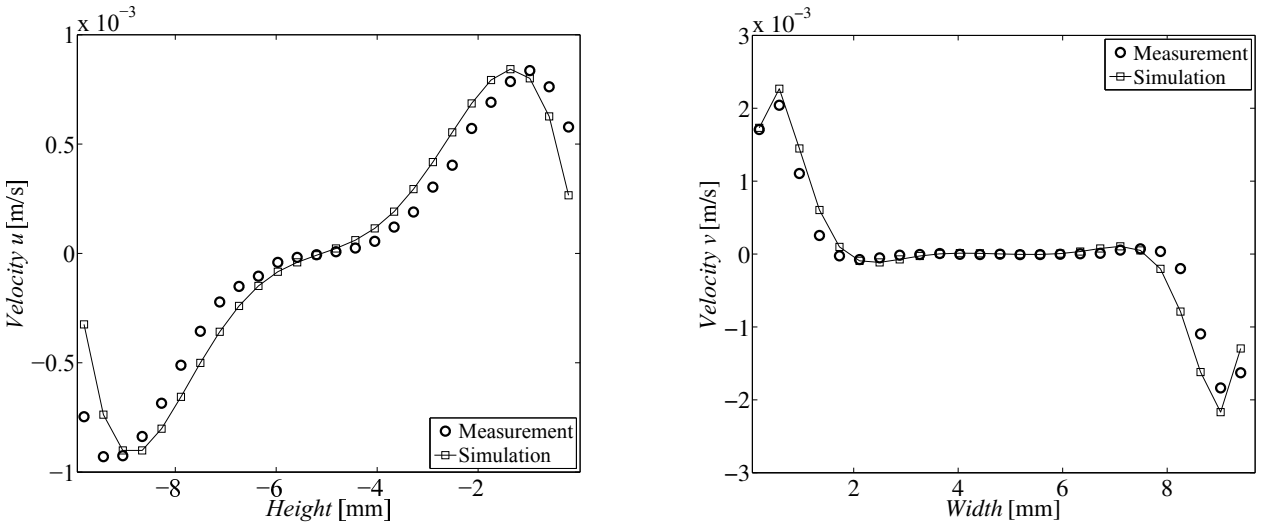

Figure 5.11: Comparison of measured and simulated velocity profiles for a flow driven by natural convection. In (a) the profile of the velocity in horizontal direction u is shown for $Width = 4.8$ mm. In (b) the profile of the velocity in vertical direction v is shown for $Height = -4.8$ mm.

Comparison of velocity profiles

For a quantitative comparison of measured and simulated velocities, the profiles for the horizontal u and the vertical velocity v are plotted in 5.11. Both profiles are plotted approximately at the middle of the test cell along the vertical axis (a) and the horizontal axis (b). Good agreement with the simulation can be found. While the measured velocity v shows a smaller relative deviation from simulated velocities than u, the absolute deviation is higher for v ($|v| \leq 6{\times}10^{-4}$ m/s) than for u ($|u| \leq 4{\times}10^{-4}$ m/s).

Images illuminated with a single laser pulse

The results presented previously are derived from images that were illuminated with multiple laser pulses (5 pulses/image pair). Measuring flows with higher velocities, however, requires single pulse illumination. The duration of a single laser pulse is such short ($\approx$ 100 ns) that particles do not appear distorted in one image even at very high flow speeds. For the optical setup used, the velocity would have to exceed 120 m/s in order that a displacement during the pulse length could be recognized. On the contrary, since the time interval between subsequent pulses is long ($\geq$ 1 ms), particles move significantly in this time and are pictured multiple times (at different positions) in one image.

The experimental setup used, allows exposing the camera images to a single laser pulse. But, their signal to noise ratio is much lower than for the images that are illuminated with multiple pulses. In Figure 5.12 the result of the temperature measurement (a), illuminated with only one laser pulse and its deviation from the numerical solution (b) is presented. The data processing is done using the same parameters as for evaluation of data shown in Figure 5.7 ($M = 5$, N=5).

While the measured temperature field in the bulk is also in good agreement with the simulation, the deviation gets significant at the edges, where steep temperature gradients are present. A possible reason for that is the particular low signal to noise ratio at the edges ($\mathrm{SNR}_{\mathrm{edges}} = 18$),provoking a reduced dependency on temperature for the ratio at these positions. Hence, temperatures are evaluated too

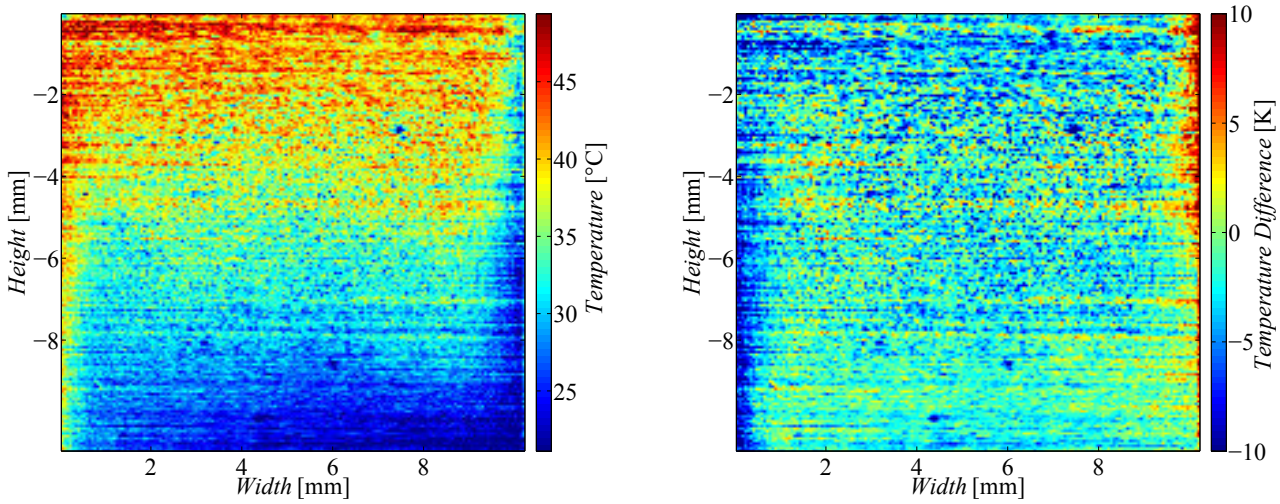

Figure 5.12: Measured temperature field for a flow driven by natural convection (a) and the resulting deviation from simulation results (b). Deviation array is calculated analogously to that in Figure 5.8.

high for the upper measurement range and to low for the lower temperature range, because a global calibration polynomial is used.

In general the SNR has minor influence on the measurement precision as explained in the following and in section 5.1.6. Nevertheless, the high deviations between measurement and simulation at the edges in Figure 5.12 can be attributed to the low SNR at these positions.

Mean SNR for both images [-]	Number of pulses per image [-]	95 % confidence interval whole temperature field [K]	95 % confidence interval temperature field without edges [K]
78	5	±6.0	±5.5
32	1	±6.4	±5.5

Table 5.1: Comparison of measurements with images illuminated by a single laser pulse to measurements with images illuminated by five laser pulses with regard to SNR and measurement precision.

In table 5.1 the 95 % confidence intervals for single and multiple pulse illumination are shown. The SNR is evaluated according to section 5.1.6. It can be seen that the accuracy of the measurement shows no considerable dependency on the SNR of the particle images. For the whole temperature field the 95 % confidence interval is only slightly broader and remains constant if the edges, where the deviation for the single pulse illumination is particularly high, are neglected. Thus, it can be concluded that measurements can be performed with only one laser pulse per image, without an important loss of measurement precision.

Into the bargain, multiple pulse illumination needs careful adaption of the acquisition rate to the flow velocity, while the frame rate of the cameras can be chosen freely when images are illuminated with a single pulse. The latter facilitates recording of images that are less statistically correlated, due to a tunable displacement of the particles between subsequent images.

5.1.5 Results of capillary flow experiments using volume illumination

The presented measurement technique is also intended to be used for applications in the mini- and microscale. Since for these cases there is often only one optical access available, volume illumination has to be applied. The applicability for microscale is proven using the setup described in section 3.1.5. For these measurements the images are illuminated with a single laser pulse, because the flow velocity inside the capillary is comparatively high.

The images show only a little number of particles with a rather high distance between two particles (see examples of images in Figure 4.6). This results from the low seeding density, which is necessary to reduce the contribution from out-of-focus particles to the signal. Due to the low seeding density, data processing with single particle detection and gaussian fitting according to section 4.1.4 is necessary.

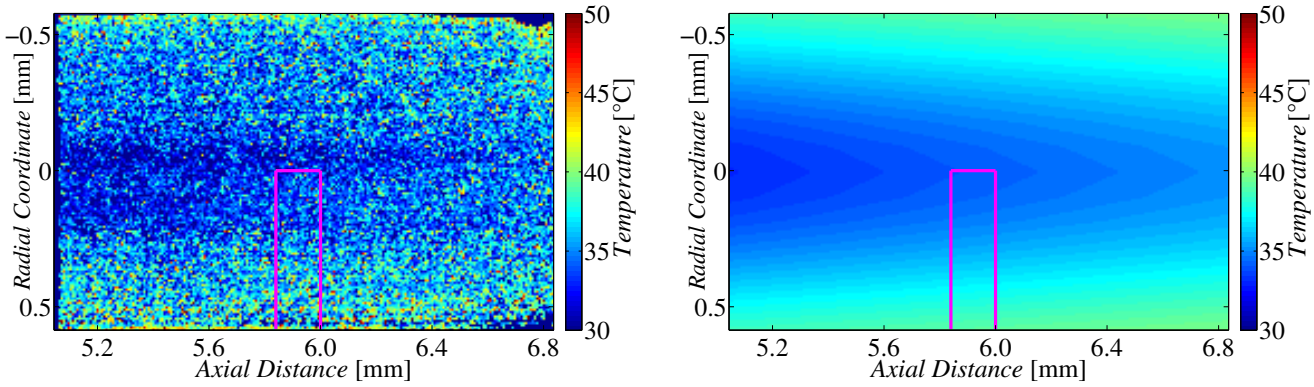

Figure 5.13: Comparison of measured (a) and simulated (b) temperature field for the laminar glycerol flow proceeding in horizontal direction inside the capillary tube. The temperature distribution is induced by a heat flux in radial direction towards the center of the tube. The axial distance represents the distance between the measurement point and the position where the heating of the flow sets in. The mark indicates the region from which the temperature profiles in Figure 5.15 are derived.

In Figure 5.13 the measured temperature field is compared to the results of a simulation of the flow inside the capillary with corresponding boundary conditions. Measurement data is processed using an interrogation window size of 4 × 4 pixels ($M = 4$), corresponding to an area of 8 × 8 µm^2 in the measurement plane. A temporal averaging over 500 image pairs ($N = 500$) is performed. Although the uncertainty for the measurement is quite high, a good qualitative agreement with the simulation can be found. The accordance is quantified by subtraction of both temperature arrays. For that purpose the simulation is adapted such that one data point can be directly related to a measurement point at the same global position. Both, measurement and simulation, are therefore referenced to the point where heating sets in (axial distance = 0 mm) and the size of the simulations' data points is matched to the measurement. This results in the array shown in Figure 5.14. No biased deviation can be recognized in this comparison. The stochastic error is quite high and can be quantified by calculating the 95 %-confidence interval analogously to section 5.1.4.

This procedure is applied to measurements at different flow rates, resulting in the 95 %-confidence intervals listed in table 5.2. The mean deviation indicated in this table is calculated as the average value of all points in the residual array (Figure 5.14).

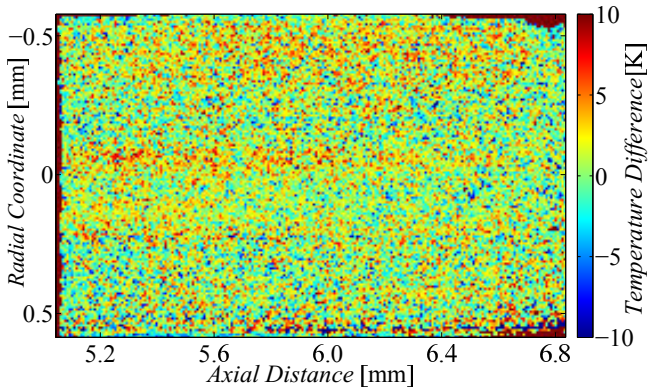

Figure 5.14: Difference between measured and simulated temperature fields for the capillary flow.

Flow rate [ml/h]	95 % confidence interval [K]	Mean deviation [K]
0.5	±8.6	1.3
3	±7.6	1.6
6	±7.2	0.2
8	±6.9	0.8

Table 5.2: 95 % confidence interval and mean deviation between measurement and simulation for different flow rates. An increase of measurement precision can be observed for increasing flow rates.

Although an extensive temporal averaging is performed, the measurement technique is still quite imprecise, while the mean error is comparatively small. This can also be recognized in the temperature profiles illustrated in Figure 5.15

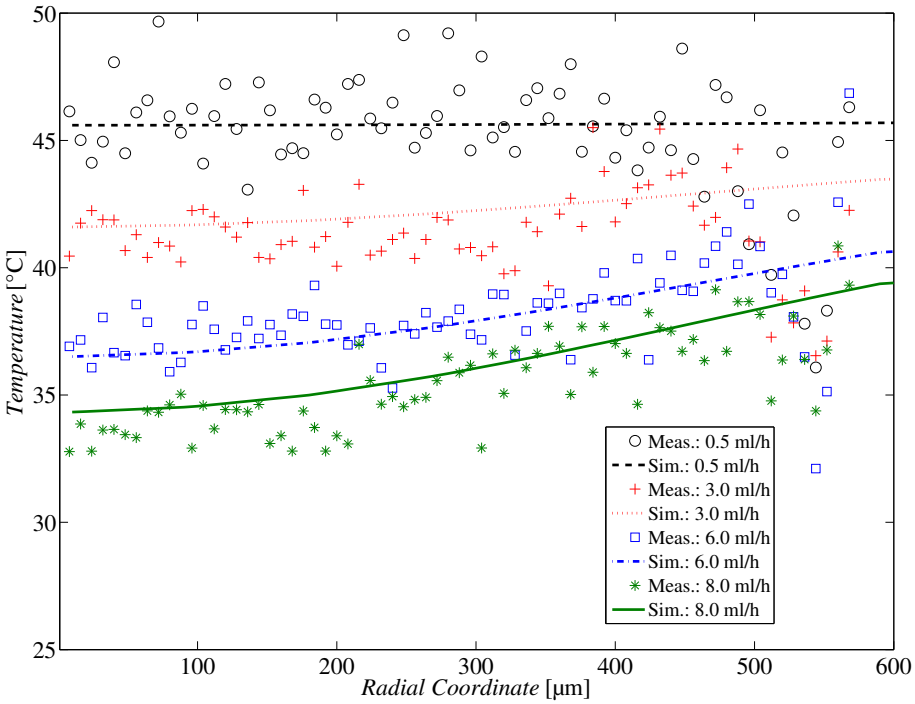

Figure 5.15: Temperature profiles along the radial coordinate for different flow rates. Measurement points are evaluated for the region marked in magenta in Figure 5.13 and compared to the respective temperature gradient from the numerical simulations.

The sections presented are calculated from the region marked in magenta in Figure 5.13, with an averaging in axial direction over all 20 interrogation windows. This is repeated for measurements at different flow rates, without altering the position of the labeled area. The precision is quite low due to the small number of particles that pass one interrogation window in the sequence of 500 images (in the mean 2.7 particles per interrogation window). Especially near the wall of the capillary tube (radial coordinate > 500 µm), the number of particles and their velocity is so small that for many interrogation windows only a single particle is present during a sequence of 500 images. Moreover, the precision increases with the flow rate which can be explained by the elevated number of dissimilar particles passing the field of view in the same time interval. This leads to a reduced correlation of subsequent particle images. As demonstrated and clarified in section 5.1.6, the fluctuations can be attributed to an alternating intrinsic particle property. Hence, the precision is increased by averaging over numerous different particles.

Velocity profiles are evaluated for the marked area in Figure 5.13 and plotted against the radial position in the tube for different flow rates (Figure 5.16). A good agreement between measurement and simulation can be observed. Due to the low seeding density and a large particle displacement between subsequent images, the sizes of the correlation windows in the PIV-algorithm have to be chosen very large. This leads to erroneous results near the wall, where steep gradients are present that cannot be resolved. In Figure 5.16 this error can be seen for the measurement data at a flow rate of 6 ml/h and a radial distance from the center exceeding 450 µm. For a flow rate of 8 ml/h, the particle dis-

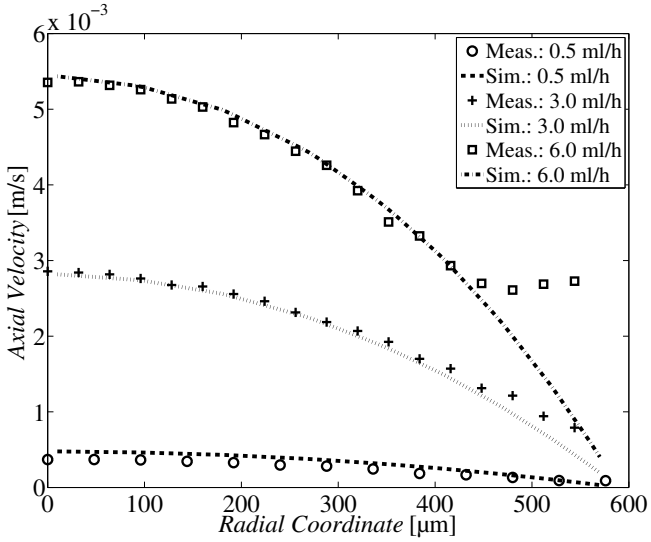

Figure 5.16: Comparison of velocity profiles evaluated from subsequent particle images by means of PIV and velocity profiles from the numerical simulations.

placement between two images is too big (ca.120 Pixel) to be processed by a PIV-algorithm for velocity determination.

Concluding it can be said that a simultaneous measurement of temperature and velocity fields is possible, even if volume illumination is applied and temperature gradients along the optical axis are present. For this purpose, however, the seeding density has to be chosen very carefully so that mainly particles moving in the focal plane are included for the determination of temperature. The small number of microcapsules in the images makes temporal averaging over many subsequent images necessary and limits the applicability of this technique to stationary flows.

5.1.6 Characterization of measurement technique at homogeneous temperature

Measurement precision and accuracy

As the previous sections showed, there is no measurement uncertainty associated with this measurement technique that is generally valid. In fact, the uncertainty is depending on many factors determined by the measurement setup and the data processing. Nevertheless, the microcapsules are identified as the main error source, which will be explained in the following. Consequently, the precision of the temperature measurement is especially affected by the number of differing microcapsules taken into account in the averaging procedures. A correlation between the number of averaged particles and the resulting precision is developed in this section, to provide an estimation for the measurement certainty in future applications.

Due to the fact that in one image sequence basically the same particles are shown, it is supposed in section 5.1.4 and 5.1.5 that subsequent images are statistically correlated. In Figure 5.17 the results for averaging in flow direction (b), respectively perpendicular to it (a), are illustrated. These data are evaluated from measurements with a homogeneous temperature distribution in the field of view and an inherent flow in one direction. The same setup and data processing as for the application presented in 5.1.5 is used.

Averaging perpendicular to the flow appears to be significantly more effective than averaging in flow direction. This can be explained by the correlation of the single interrogation windows. All interrogation windows along an axis perpendicular to the flow cannot contain the same particle and are thus statisti-

cally uncorrelated. On the contrary, one particle can be seen in different interrogation windows along an axis coaxial to the flow direction, making them statistically correlated. These findings imply that temperature variations are at least partly attributed to varying intrinsic properties of the microcapsules, which causes the ratio to deviate from particle to particle. For this reason, many different particles must be taken into account for an effective averaging.

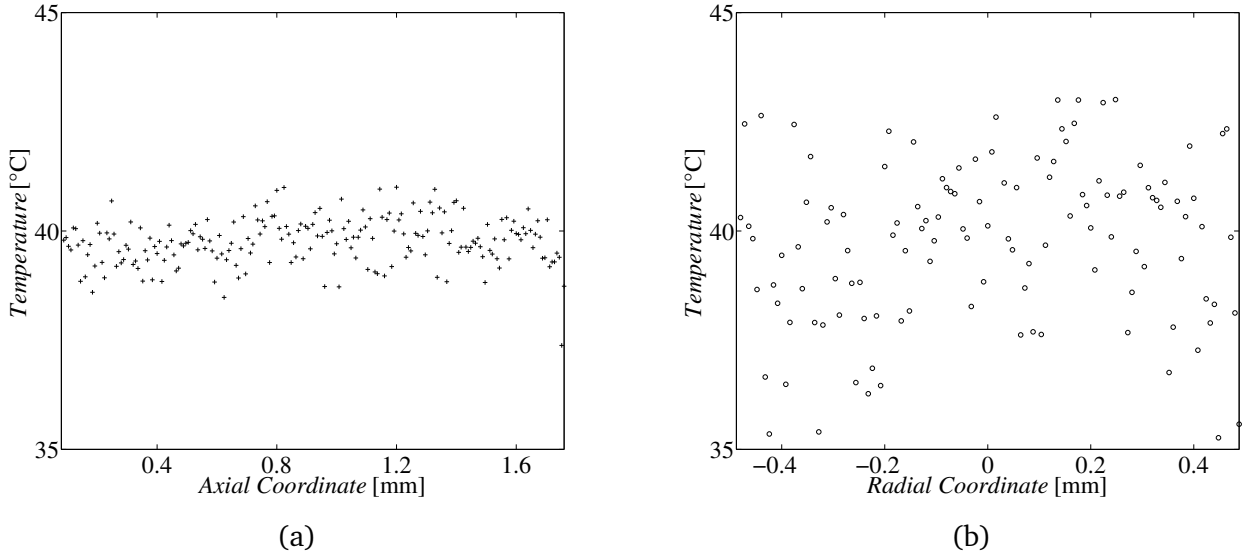

Figure 5.17: Resulting temperatures for different averaging procedures for measurements with a homogeneous temperature distribution. In (a) the data was averaged along the radial coordinate (perpendicular to the flow direction) compared to an averaging along the axial coordinate (b) (coaxial to the flow direction).

The number of particles that are necessary to achieve a specific measurement precision is identified in the following. For this purpose, the installation described in 3.1.6 is employed, facilitating to set a homogeneous temperature distribution in the fluid. The resulting image sequences exhibit an almost unidirectional flow with an uniform velocity distribution, as illustrated in Figure 5.18 (a). Data are processed using the algorithms described in 4.1.3 with a local averaging of 5 pixel ($M = 5$) and without temporal averaging ($N = 1$). The mean distance between two particles is 13 pixel and thus broader than the size of one interrogation area. The particles' displacement between subsequent images (Figure 5.18 (b)) is approximately 40 pixel. Correspondingly, one interrogation window represents the temperature measured by one single particle. Thus, calculating the vectors according to Figure 4.7 for every interrogation window provides statistically uncorrelated data points.

By this means, the fluctuation of the particles' ratios causing the strong deviations in temperature measurement can be estimated. In 5.19 the standard deviation of the measured temperature, which is evaluated by taking the mean σ of 3000 vectors, is plotted for different numbers of averaged image pairs N.

In the case of $N = 1$, σ represents the precision that can be achieved, if each measurement point is evaluated from the ratio of one single particle. If the number of particles used for the determination of temperature increases, the precision rises as well. It is not relevant, whether particles of the same image pair (spatial averaging) or of subsequent image pairs (temporal averaging as in Figure 5.19) are considered, as long as they are statistically uncorrelated. In general, the precision of a measurement increases with the number of repetitions n according to

$$\sigma_n = \sigma_{\text{single}}/\sqrt{n} \tag{5.2}$$

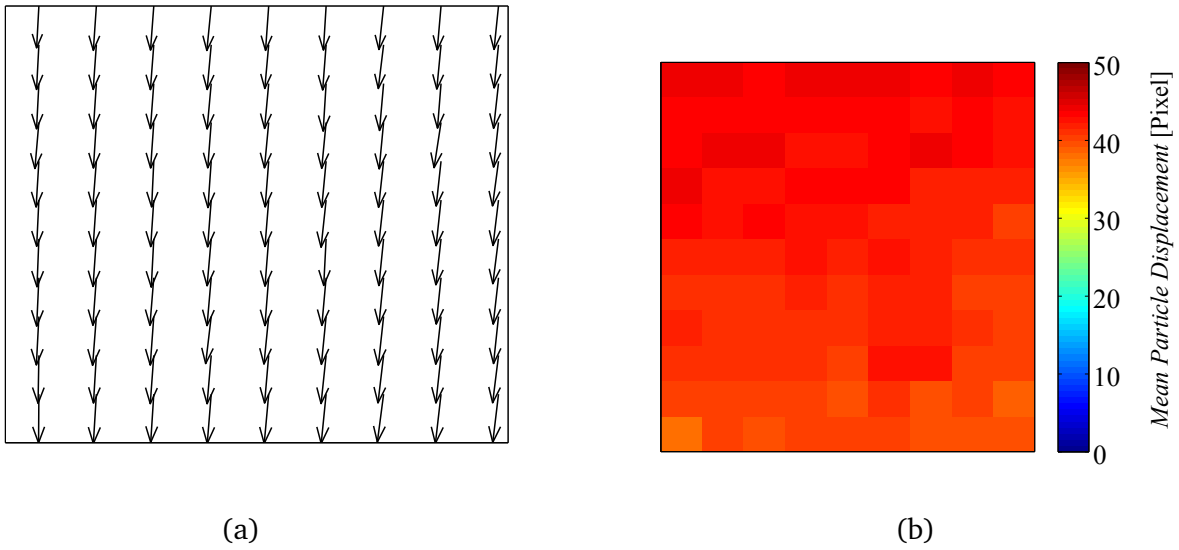

(a) (b)

Figure 5.18: Vectors of particle displacement between subsequent images (a) and the corresponding magnitudes (b) for the considered image section.

For the present case σ_{single} is the standard deviation for single particles, without averaging and the development of the corresponding σ_n is plotted as circles in Figure 5.19. As the standard deviation from measured data and the calculation according to equation 5.2 are in good agreement, the aforementioned estimation that all data points in the vectors are uncorrelated is confirmed.

It is worth noting that the standard deviation presented in Figure 5.19 is still composed of deviations attributed to intrinsic differences of the microcapsules' properties and the ratio deviations resulting from the cameras' noise. The approximate portion of camera noise and intrinsic particle ratio deviation is estimated later in this section.

In Figure 5.19 the histogram of measured temperatures computed from all data points of the above-quoted vectors (from which the standard deviations are estimated) is plotted. A gaussian distribution can be recognized for this set of data, suggesting that the measured variable (the ratio R) shows this characteristic as well. The mean value and the standard deviation is indicated by a solid line at 24.5 °C and two dashed lines at 12.2 °C and 37.8 °C, respectively.

The accuracy of the measurement technique is mainly effected by the quality of the required in-situ calibration procedure (see section 4.1.7). As clarified in section 5.1.4 and 5.1.5 no significant bias error can be recognized for the presented results. Moreover the measurement certainty is dominated by its precision due to the high standard deviation of the resulting temperature data.

However, influencing factors, such as a temporal drift of the ratio that might cause bias errors, are identified and presented later in the following paragraph.

Error sources

A deviation of the microcapsules' intrinsic properties was identified as the main reason for the comparatively low measurement precision of the presented technique. Another influencing factor, however, is the cameras noise, more precisely the SNR.

For the images from which the results presented in 5.19 are derived, the overall $SNR_{\text{b1,b2}}$ is calculated to be 98, according to the procedure described in the following. First the noise is calculated for each camera from the standard deviation of all pixels' intensity, when the images are not illuminated (dark

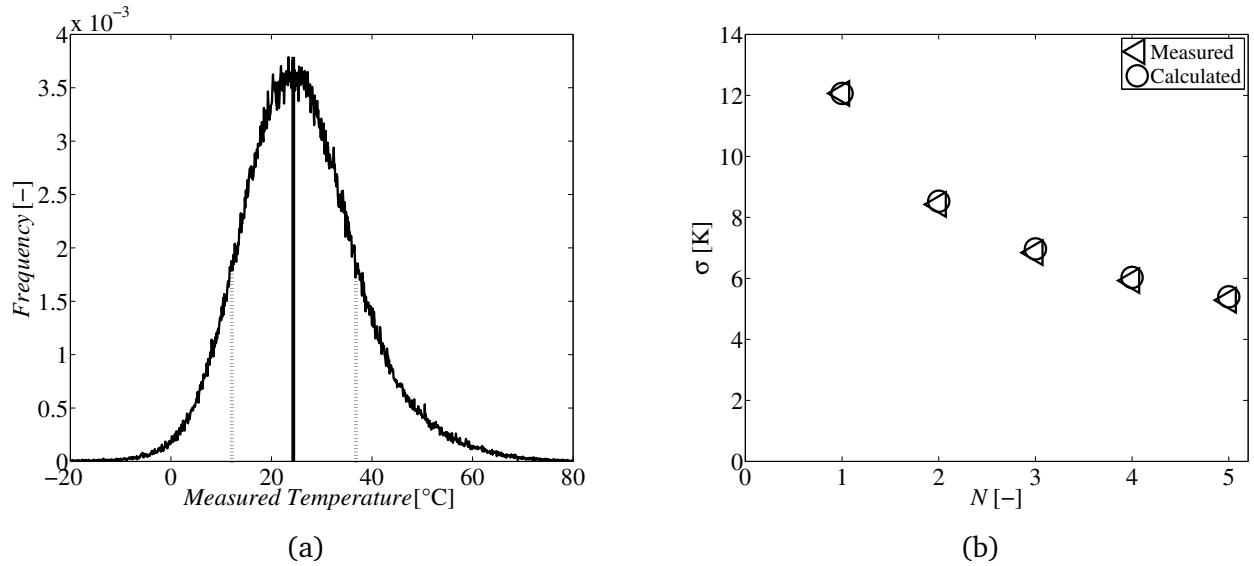

(a) (b)

Figure 5.19: Relative frequency distribution (a) of the temperature determined from individual particles (no averaging over multiple particles performed) and standard deviation (b) of measured temperature (corresponds to the width of the region marked with dashed lines in (a) for N=1) for varying number of images pairs (matches with number of particles) considered for averaging.

images without laser pulse). The SNR corresponds to the quotient of the mean signal, calculated from the average intensity of all detected particles in the illuminated images, divided by the noise.

As the ratio results from these two fluctuating signals, the final $SNR_{\mathrm{b1,b2}}$ is calculated according to the principle of error propagation for stochastic uncorrelated errors [24]:

$$SNR_{\mathrm{b1,b2}} = 1/\sqrt{\left(\frac{1}{SNR_{\mathrm{b1}}}\right)^2 + \left(\frac{1}{SNR_{\mathrm{b2}}}\right)^2} \tag{5.3}$$

This results in a standard deviation for the determination of the ratio of $1/SNR_{\mathrm{b1,b2}} = 1.03$ %, when no temporal or spatial averaging is performed. With a temperature sensitivity of 0.5 %, this provides a standard deviation of the resulting temperature caused by the cameras' noise of $\sigma_{\mathrm{cams}} = 2.0$ K. Compared to the overall standard deviation of the measured temperature depicted in Figure 5.19 ($\sigma = 12.3$ K) the contribution caused by the cameras' noise is insignificant. Into the bargain, local averaging (M=5) is performed for the data in Figure 5.19, which reduces the portion of σ_{cams} by a factor of $\sqrt{5}$ to $\sigma_{\mathrm{cams}} = 0.9$ K. Hence, the finding that there is no significant correlation between the images' SNR and the measurement certainty (see table 5.1) is confirmed. The SNRs presented there contribute to the overall temperature fluctuations with $\sigma_{\mathrm{cams,singlepulse}} = 1.25$ K and $\sigma_{\mathrm{cams,5pulses}} = 0.5$ K, respectively. The slightly increased precision for the images with higher SNR is compensated by the reduced statistical correlation of subsequent image pairs associated with the single pulse illumination (see section 5.1.4).

In the following, the correlation between the absolute image intensity and the particles' ratio is investigated using the same data as presented in Figure 5.19 (homogeneous temperature field with homogeneous velocity distribution). The data processing, however, is slightly different. After the misalignment correction (section 4.1.1) and particle detection (section 4.1.3), a 300 × 250 pixels region is selected as the region of interest. All particles detected in this region are investigated separately with regard to their intensity in image B and their ratio. This is repeated for many image pairs and stored in two vectors, where every element represents the ratio and the corresponding intensity of one particle.

On the left side of Figure 5.20, the ratios in the resulting vectors are plotted against their intensities. The dots represent the single ratios, while the red lines correspond to the mean of all ratios at a spe-

cific intensity. It can be recognized that there is a correlation between the mean intensity and the ratio. Further, the curve can be divided into two regions, showing a strong dependency (region A) respectively a reduced dependency on the intensity (region B). The subplots stacked in vertical direction represent measurements at varied laser excitation power[2]. On the right side of Figure 5.20 the frequency distribution of the ratio, representing the relative number of data points available for each integer step of intensity, is shown.

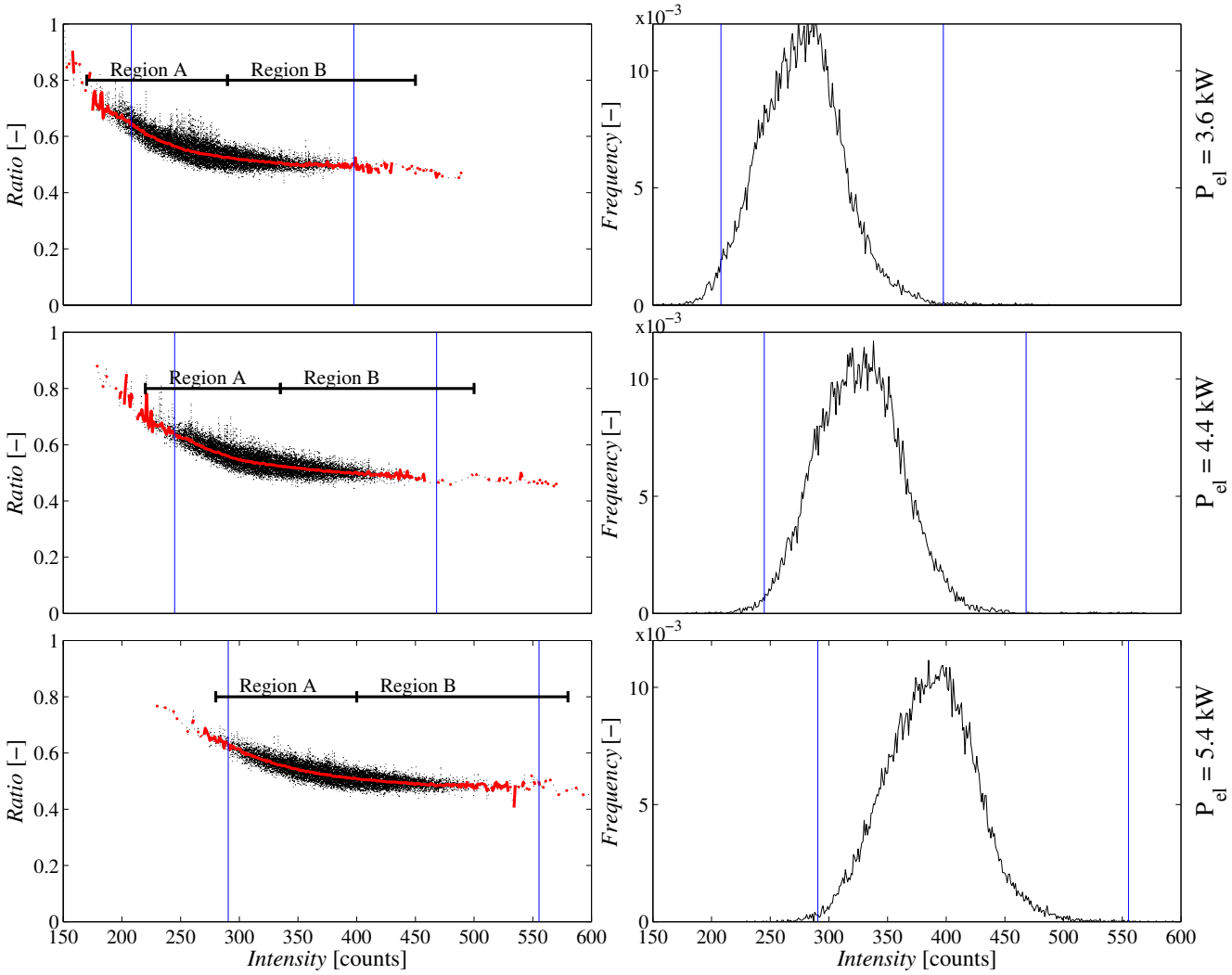

Figure 5.20: Ratio of particles and relative frequency of particle intensity plotted over the particle intensity for different laser powers. Region A marks the range in which a strong correlation between the ratio and the particle intensity can be observed. This correlation strongly decreases in region B.

Both, the ratio curve and frequency distribution exhibit a shift towards higher intensities with increasing excitation power. An accordant shift can be noticed for regions A and B as well. This implies that the intensity does not cause the ratio drop in region A, as it occurs for different absolute intensities. Hence, neither a fluctuation of the fluorescence radiant flux, nor an error in the signal detection system (e.g. nonlinearities of the camera response) can explain these observations. In fact, both quantities must depend on the same fluctuating parameter, which causes the observed correlation. Additionally this parameter is supposed to be normally distributed.

[2] Electrical input power is varied. Optical output power is proportional to the electrical power, but cannot be quantified.

The most likely explanation for these findings is the variation in particle size, which influences the particle intensity according to section 2.2.1. Equation 2.8 results in I $\propto d^3$, since the measurement volume V corresponds to microcapsules with diameter d.

As explained by equation 2.5, the ratio of a single microcapsule depends on the length of the optical path (distance the signal has to pass through the absorbing medium). Equation 2.5 was derived for the case of two signals with discrete wavelengths originating from one single point and passing through an absorbing medium along the path x. In the microcapsules, on the contrary, re-emission processes result from a combination of excitation and signal generation by fluorescence followed by the re-absorption of this signal with subsequent fluorescent re-emission. For the microcapsules used, the optical path length x corresponds to their radius. Anyhow, this correlation is a reasonable approximation to describe the absorption processes inside the microcapsules.

In Figure 5.21 the absorption spectrum of the microencapsulated core solution is shown. The dotted-dashed line marks the excitation wavelength, while the hatched regions highlight the domains from which the temperature sensitive signal (590 nm $< \lambda_2$) and the reference signal (540 nm $< \lambda_1 <$ 570 nm) are extracted. A remarkable difference of the absorption coefficients $\alpha(\lambda_1)/\alpha_{\max} \approx 0.3$ to 0.05 and $\alpha(\lambda_2)/\alpha_{\max} \approx 0$ can be recognized. This results in the observed ratio's dependency on the optical path length, as described by equation 2.5.

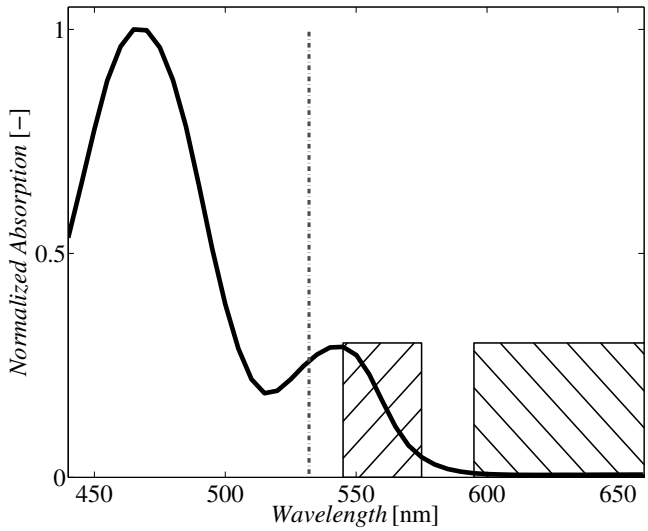

Figure 5.21: Relative absorption spectrum of microcapsules' core solution. The wavelength bands of the reference signal (540 nm < λ < 570 nm) and the temperature sensitive signal (590 nm < λ) are marked by hashed regions.

Such a dependency of the measured fluorescence ratio on the droplet size has also been observed by Labergue et al. [36] for measurements of water and n-decane droplets with varying size ($d_{\text{Droplet}} = 45$ µm to 360 µm). A droplet generator was used to generate the droplets. They recognized a reduction of the fluorescence ratio for droplet diameters exceeding 200 µm of ≈ 2.5 %, which is in line with their theoretical calculations of the ratio taking into account re-absorption effects.

Another verification can be found in Figure 3.6 that is provided by the particles' manufacturer. The particles' size is normally distributed as well, with 10 % of the particles being smaller than 8.3 µm, 10 % bigger than 10.3 µm and a median value of 8.9 µm. Assuming that $I = K_{\text{opt}} \cdot d^3$ is valid and the most frequent intensity corresponds to the most frequent particle size (8.9 µm), K_{opt} can be estimated. Hence, the intensities corresponding to the boundaries of the 90 %-interval are calculated and plotted as blue vertical lines in 5.20. Their horizontal position is in good accordance with the positions of the corresponding particle sizes in Figure 3.6.

Concluding it can be said that an intrinsic variation of the particles' ratio is the main error source for the presented measurement technique. A correlation between the mean ratio of the particles and their intensity in the images can be observed, suggesting that the ratio depends on the particle size, as described previously. However, besides the particle size, there are many other factors influencing the particle brightness that differ for every particle in the field of view. Such factors are the interaction of the fluorescence signal with objects in the optical path (other particles, the carrying fluid), its position perpendicular to the focal plane and local variations of the excitation power. As these influencing variables can neither be controlled nor reduced, the only possibility for achieving an appropriate measurement precision are averaging procedures as used in the applications in section 5.1.4 and 5.1.5.

For measurements that take a comparatively long time, or when many repeated measurements are necessary, another error can become significant. As illustrated in Figure 5.22, a clear increase of the difference between the temperature calculated from the microcapsules' ratio and the reference temperature measured by thermocouples in the fluid can be observed. These data are obtained from measurements of homogeneous temperature fields (setup described in section 3.1.6) with a spatial averaging over the entire field of view. No linear relationship between the time (referring to the ending time of the calibration procedure) and the temperature difference can be recognized for plot (a). In plot (b), however, the linear fit (solid line) represents quite well the increase of temperature with the total number of image sequences taken. The error caused by this temporal drift can be corrected by conducting calibrations before and after the actual measurements.

There are two feasible explanations for this finding. First, a photochemical degradation (Photobleaching, see section 2.1.6) of the dyes in the microcapsules can alter the fluorescence properties which determine the ratio. This damage can be caused by exposing the dyes to long-lasting radiation with high fluxes. The second reason can be the faster sinking velocity of particles with a bigger diameter according to equation 3.6. Although the fluid with the dispersed particles is continuously pumped, there are some regions, where the flow that prevents the particles from descending due to gravitation is very slow, leading to a decrease of large particles in the flow. As explained previously, the ratio is correlated with particle size (bigger particles exhibit reduced ratio in the mean) and consequently the ratio and thus the calculated temperature rises gradually. However, this effect is only observed during measurements and the microcapsules are very stable in their fluorescence properties during storage. No differences are observed between the first experiments and the latest experiments that have been performed with a temporal separation of approximately 2 years. The microcapsules are provided by the manufacturer in dispersed form in purified water in a glass container and are also stored this way.

As shown above, the SNR of the camera images has minor influence on the measurement precision. However, the cameras can also cause a biased error, in the case of a low SNR. This is due to the fact that the signal generated by incident photons must exceed the dark noise (caused by electrons reaching the conduction band without photon excitation). For very low SNRs this offset alters the correlation of fluorescence and intensity counts in the camera images. Thus, also the temperature sensitivity in very dark image regions is smaller than for bright image regions, which causes errors (temperature at the edges in Figure 5.12), if this is not taken into account in the calibration procedure (see also section 4.1.7). However, the influence of this error strongly reduces with the particles' brightness and thus its contribution to the results that were obtained with image processing techniques including a particle detection is insignificant.

It is worth noting that the above fluctuations and biased deviations of the ratio strongly influence the determined temperature due to the comparatively low temperature sensitivity of 0.5 %/K. Although this is not an source of errors, it is a factor that linearly influences the measurement certainty.

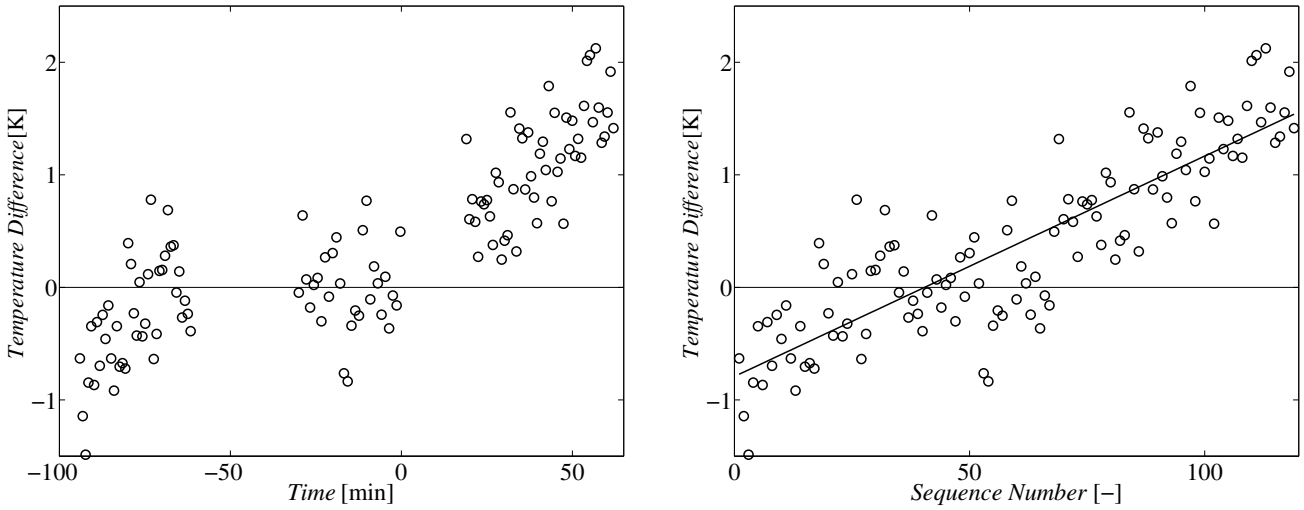

Figure 5.22: Difference between measured temperature and the reference temperature from thermocouples in the fluid, in which microcapsules are dispersed. In (a) the temperature difference is shown over time in relation to the ending time of the calibration procedure, while in (b) it is plotted over the consecutive number of the measurement. The continous line marks a linear fit to the data.

General applicability

In the following, the applicability of the developed method for future implementations, as well as important features that should be taken into account during utilization, are analyzed.

One drawback of the microcapsules are their high costs for manufacturing. Therefore, the microcapsules are preferably used in setups, where the volume of liquid needed for the measurement is limited to some milliliters.

One prerequisite of a potential application is the feasibility of an in-situ calibration. This means that the temperature calibration has to be done at exactly the same setup as the actual experiment. An in-situ calibration is necessary, as the ratio depends on numerous factors that must be taken into account by this procedure.

In section 5.1.4 and 5.1.5 it is demonstrated that experiments with a single pulse illuminating one image pair can be conducted. Consequently, the implemented installation facilitates simultaneous measurements of temperature and velocity fields at an acquisition rate of 1000 Hz. The time needed to heat up a single particle is estimated to be less than 1 ms (see section 3.1) and the fluorescence itself (absorption and emission of light) takes place on the order of 10^{-9} s. As a consequence, the acquisition rate is limited by the used equipment, to be more precise, by the pulse repetition rate (1000 Hz) of the laser.

To increase the precision in temperature determination it is advantageous to have a large displacement of the particles between subsequent images, due to the reduced statistical correlation of the images. Additionally, the particles' displacement should exceed the size of an interrogation window so that for every time step different particles are involved. On the other hand, velocity can only be evaluated, if the displacement is smaller than a correlation window in the PIV processing. Thus, the acquisition rate of the cameras must be chosen very carefully, to achieve the best possible results.

The spatial resolution is primarily defined by the optics used. For the microscope setup 3.1.5 one measurement point corresponds to 8×8 μm^2 in the image plane. In the case that temporal averaging

is not applicable, the limiting factor is the distance between particles, as the temperature can only be calculated for positions at which particles are present.

In the previous sections it is illustrated that the measurement precision can be increased by appropriate averaging procedures considering many different particles. Though, a reduction of temporal and/or spatial resolution has to be accepted when averaging is performed. Depending on the specific application, these three characteristic features must be balanced. For the measurement of transient phenomena, the feasibility of temporal averaging is limited. Hence, for such applications a low precision or a reduced spatial resolution must be accepted. Even in the case that the acquisition rate can be set much higher than the time-scale, in which the transient phenomena take place, temporal averaging is not effective. This is due to the fact that heat and mass transfer are coupled. For an effective averaging, particles between subsequent images should exhibit a displacement larger than the size of one interrogation window. But, when the particles are transported, heat is transported as well by convection. Thus, the change in temperature during the time between these two images, cannot be resolved.

5.1.7 Comparison with other temperature measurement techniques

In table 5.3, the developed microcapsule technique is compared to other methods for 2-dimensional temperature measurements in liquids. For some of them numerous works exist and only the most relevant works for this comparison are listed. A detailed description of the listed methods can be found in section 2.2.

The signal type listed in this table is of interest, since for fluorescent and luminescent signals, the excitation can be separated from the signal, while in the case of reflected signals (TLCs), the white light illumination cannot be filtered out. This superposition of signal and excitation can falsify the results, especially in the vicinity of reflecting objects (e.g. walls).

The applicability of volume illumination refers to measurements, for which temperature gradients along the optical axis of observation exist. For the LIF technique with dissolved dyes it cannot be determined, from which focal plane the signal arrives and thus the results are influenced by potential temperature gradients. In the case of particle based methods, however, the according focal plane can be located quite accurately due to distortions of the spherical particles appearing in the images.

One important advantage of the microcapsule technique is that they can be used in different fluids, provided that the microcapsule shell (PMMA) is chemically resistant. The fluorescence properties of temperature-sensitive dyes depend also on the surrounding medium. Thus, if LIF with dissolved dyes is applied, the dye has to be selected compatibly to the medium that is to be observed.

Method	Source	Signal type	Volume illumination	Temperature + velocity	Resolution	Measurement precision	Specifics
EuTTA particles	[72]	Phosphorescence	Yes (theoretically)	Yes	Spatial: 0.3 x 0.3 mm^2 Temporal: 40 ms	$\pm$0.4 K[3]	Lifetime based Required framerate = 15000 fps
Planar LIF	[51], present work	Fluorescence	No	No	Spatial: 22 x 22 μm^2 [51] Temporal: n.s. in[51][4]; 1 ms (present work)	σ = 0.49 K [51]	
LIF + scattering particles	[22]	Fluorescence	No	No	Spatial: 0.9 x 0.9 mm^2 Temporal: n.s.[5]	σ = 0.4 K to 1.1 K[6]	Trade-off: accurate temperature or velocity determination
Thermographic phosphors	[9]	Phosphorescence	Yes	Yes	Spatial: 1.3 x 1.3 mm^2 Temporal: n.s.[7]	σ = 6 K to 19 K	
TLCs	[50]	Reflection	Yes	Yes	Spatial: 0.1 x 0.1 mm^2 Temporal:> 10 ms[8]	Absolute:high ($\approx$ 0.01 K) Relative:low (20% of measurement range)	Measurement range limited (ΔT = 0.5 K to 40 K) Aging of TLCs observed
Microcapsules	Present work	Fluorescence	Yes	Yes	Spatial: 60 x 60 μm^2 Temporal: 33 ms[9]	σ = 2.6 K	Applicable in many liquids

Table 5.3: Overview of techniques for temperature field measurements in liquids.

[3] From residuals of calibration curves.
[4] Not specified; CCD-camera (framerate < 11 fps) used.
[5] Not specified; CCD-camera (framerate < 60 fps) used.
[6] Depending on number of particles and dye concentrations.
[7] Not specified; Averaging over 150 single shots.
[8] Limited by thermal response time of TLCs.
[9] Framerate set to 150 fps; Up to 1000 fps possible.

5.2 Solid microparticles from dyed polymers

5.2.1 Dyes excitable at 532 nm

In this section, the applicability of the combination of the dyes SRhB and Rh6G incorporated in films of the polymers polybutylmethacrylate (PBMA) and polyvinylacetate (PVAc) is investigated. Since these dyes are excitable at a wavelength of 532 nm, the available laser can be used for excitation. A detailed description of the selection of dyes and polymers as well as the experimental procedure can be found in section 3.2.1.

The dependency on temperature for the fluorescent emission of SRhB in PBMA (glass transition temperature of 15 °C) and PVAc (glass transition temperature of 27 °C) is illustrated in Figure 5.23. It can clearly be recognized that the fluorescent emission decreases with rising temperature. Except for the intensity at 40 °C (a) respectively 35 °C and 40 °C (b), good agreement between heating and cooling of the films is observable. The difference at 35 °C and 40 °C is probably due to hysteresis effects, when the glass transition temperature is exceeded. Thus, during the cooling cycle the polymer is still in the rubbery state at 40 °C respectively 35 °C, in which the energy transfer from the excited state to the surroundings is more effective and therefore the fluorescence intensity is reduced. For the heating cycle on the contrary, the polymer is still in a brittle state, as the glass transition temperature is not yet crossed and thus the emission intensity is enhanced. These results are in good agreement with the findings presented by Romano et al. [58] for RhB in polyurethane. Concluding it can be said that SRhB exhibits a temperature sensitivity in PBMA and PVAc, making it a potential dye for temperature measurements in these polymers.

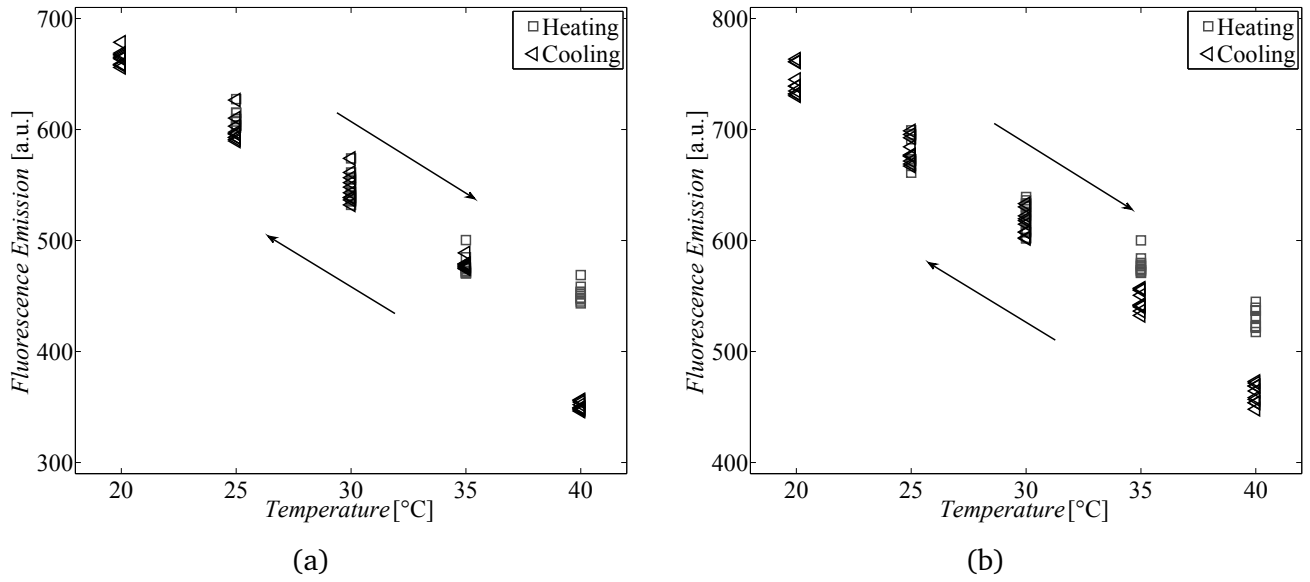

Figure 5.23: Overall fluorescent emission intensity of a film of PBMA (a) and PVAc (b) dyed with SRhB, plotted over temperature. Both films were first cooled down from 40 °C to 20 °C and then heated again to 40 °C (indicated by arrows). At each temperature step ten images are taken. The mean intensity in the region of interest corresponds to one measurement point.

According to equation 2.8 the fluorescencence intensity depends on the excited volume V, which corresponds to the particle's size. Thus, temperature measurements cannot be performed with a single dye, as the particle's size is subject to variations. A reference dye has to be incorporated that facilitates the determination of temperature following the 2-colour-LIF principle (equation 2.9).

In Figure 5.24 the emission spectra of a mixture of SRhB and Rh6G (a) and pure Rh6G (b) are illustrated. Although the pure Rh6G shows a clear fluorescence in PBMA with a emission peak around 565 nm, this emission vanishes in the mixture with SRhB and emission can only be recognized for wavelengths exceeding 580 nm (a). The concentration of Rh6G in PBMA is roughly the same for both cases (a) and (b). Increasing the proportion of Rh6G and SRhB by a factor of 8, did not cause any alteration in the spectrum. Consequently, the non-existence of the Rh6G emission in spectrum (a) cannot be explained by a superposition of a stronger SRhB emission. No reasonable explanation for the observed phenomenon could be found.

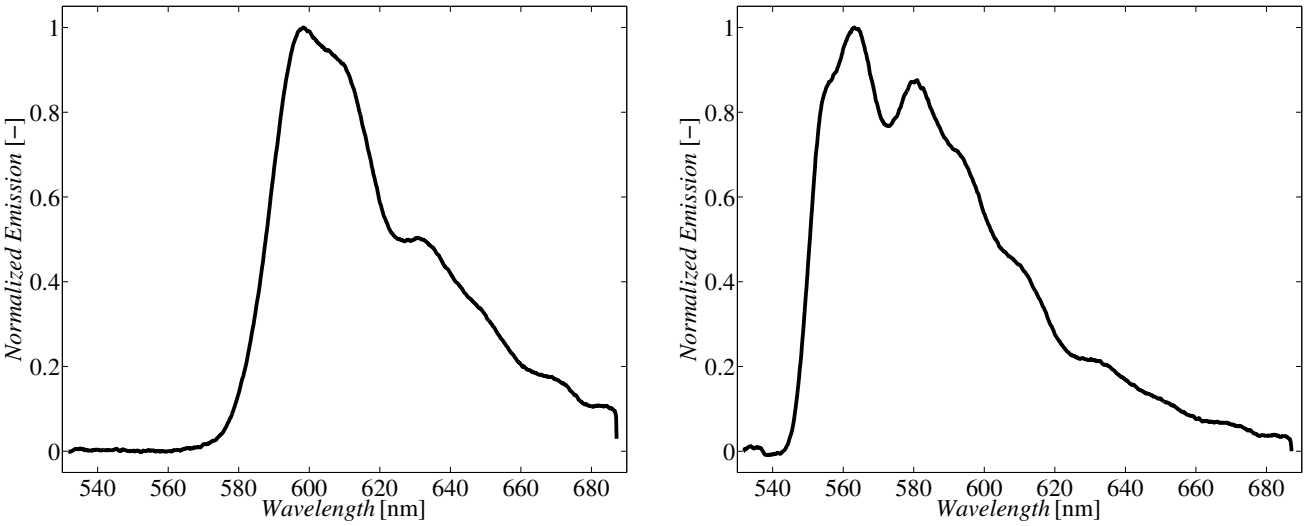

Figure 5.24: Comparison of the emission spectra of a mixture of Rh6G and SRhB (a) and of pure Rh6G (b) incorporated in a film of PBMA.

The spectral characteristics of the mixture of Rh6G and SRhB is also analyzed for the case that the dyes are incorporated in a film of PVAc. The resulting spectra at different temperatures can be found in Figure 5.25. In contrast to the emission of this mixture in PBMA (Figure 5.24), the emission of Rh6G is clearly recognizable in PVAc. Nevertheless, this combination of dyes in PVAc is not suitable for temperature measurements, as it exhibits no noticeable dependency on temperature.

Further dyes in PBMA have been investigated and the detailed results are presented in [57]. Summing up, it can be stated that none of the observed fluorescent dye combinations excitable at 532nm exhibits spectral properties in the polymers such that it is suitable for the determination of temperature by means of the 2-colour-LIF method. The fluorescence properties are strongly influenced by the surroundings of the dye molecules. Especially the dependency of the fluorescent emission intensity on temperature differs significantly for one dye incorporated in a polymer compared to the same dye in solution.

No predictions about the behavior of a specific dye composition in a specific polymer can be made. Thus, combinations of dyes and polymers that are suitable for temperature measurements can only be found empirically.

5.2.2 Dyes excitable with UV-light

In this section the applicability of polymers that are dyed with EuTTA and perylene for temperature measurements is valuated. Unlike the dyes investigated in section 5.2.1, the applicability of the com-

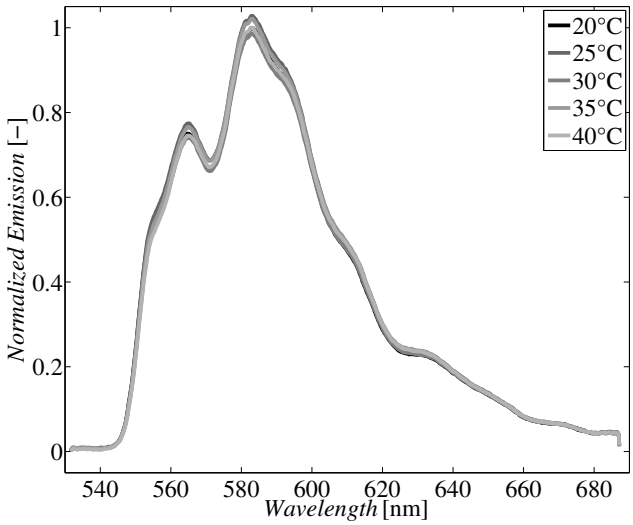

Figure 5.25: Emission spectra of the same mixture of Rh6G and SRhB used in Figure 5.24 incorporated in PVAc for different temperatures.

bination of EuTTA and perylene in different polymer films for temperature measurements has already been demonstrated in other publications [4], [45].

The analyses presented in the following are restricted to milled polymer films, as described in section 3.2.2, with regard to their potential use as temperature sensors. The experimental setup applying a colour-camera and a spectrometer, as well as the experimental procedure are both described in section 3.2.2.

The spectra shown in Figure 5.26 (a) are determined from the polymer flakes in tempered water that can be seen in Figure 5.27 (a). Two characteristic peaks, which can be assigned to the phosphorescence emission of EuTTA ($\approx$ 615 nm) and perylene ($\approx$ 480 nm) respectively, can be recognized. These peaks show different dependencies on temperature. Dividing the mean emission intensity of perylene by the mean emission intensity of EuTTA, results in the temperature dependent ratio shown in Figure 5.27 (b).

The colour images provided by a 3-CCD-camera (Hitachi-HV20) and illustrated in Figure 5.27 (a) also exhibit a colour shift with temperature that can even be recognized by human eyes. Colour images are composed of three single images: one for the red part, one for the green part and one for the blue part (RGB images). Dividing the blue single image by the red one and taking the mean of all resulting pixel values at positions where particles are present, provides the ratio presented in Figure 5.27 (b).

From Figure 5.26 a temperature sensitivity of the ratio of approximately 1.3 %/K can be calculated. This is the theoretically achievable temperature sensitivity for this specific combination of dyes in polysterene. Observing the temperature sensitivity of the ratio determined from the red and blue part of the 3-CCD-camera images, a numerical value of approximately 1.0 %/K can be identified. This reduction of sensitivity can be attributed to the transmission characteristics of the optical filters in front of the camera chips, which allow part of the blue light to reach the red detector and vice versa. The filters of the used 3-CCD-camera are suitable for temperature measurements with these specific dyes in polystyrene, as the temperature sensitivity is only slightly below the maximum achievable sensitivity.

It can be concluded that EuTTA and perylene incorporated in polystyrene are usable for the determination of temperatures, not only for films of polystyrene applied to surfaces (as reported by [4]), but also when these films are broke up mechanically and dispersed in water. In [4] temperature sensitivities ranging from 1.4 %/K to 2.1 %/K for the same combination of dyes in polystyrene are specified. The spectra illustrated in [4] are in good agreement with the one presented in this work.

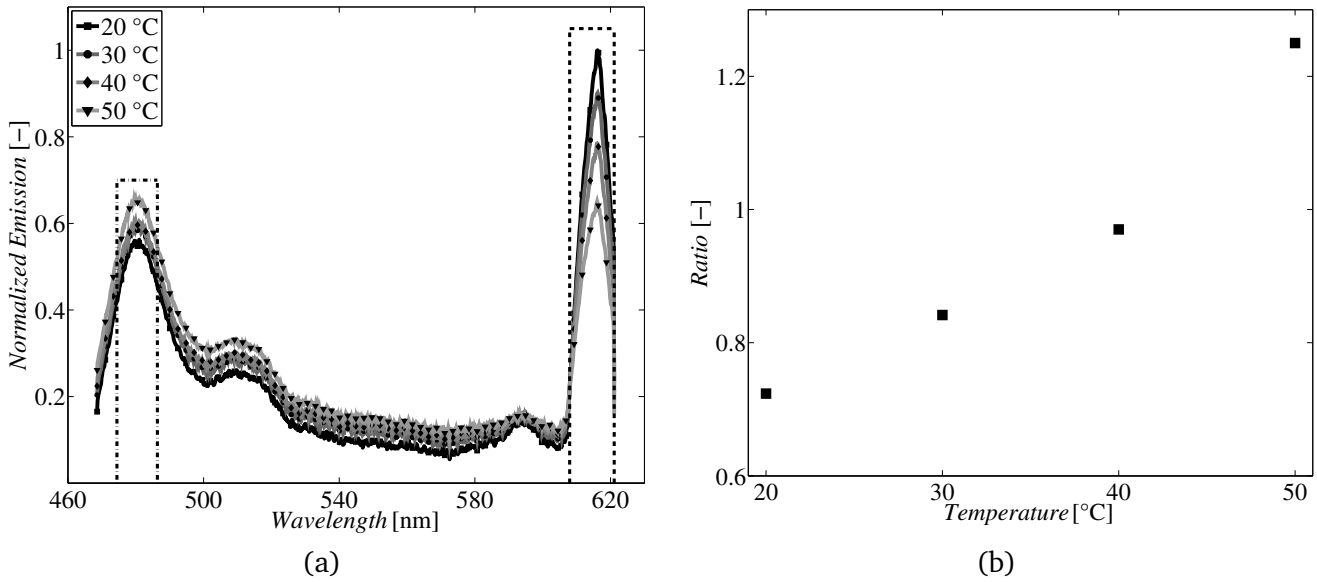

Figure 5.26: In (a) the emission spectra of EuTTA and perylene in polystyrene are shown for different temperatures. Spectra are measured from dyed polystyrene flakes shown in Figure 5.27 (a) that are illuminated by UV-light ($\lambda_{em,max}$ = 365 nm). Two regions with different temperature sensitivities are identified. The mean emission in the region marked with dash-dot line is divided by the same in the region specified by dashed line, resulting in the ratio plotted over temperature in (b).

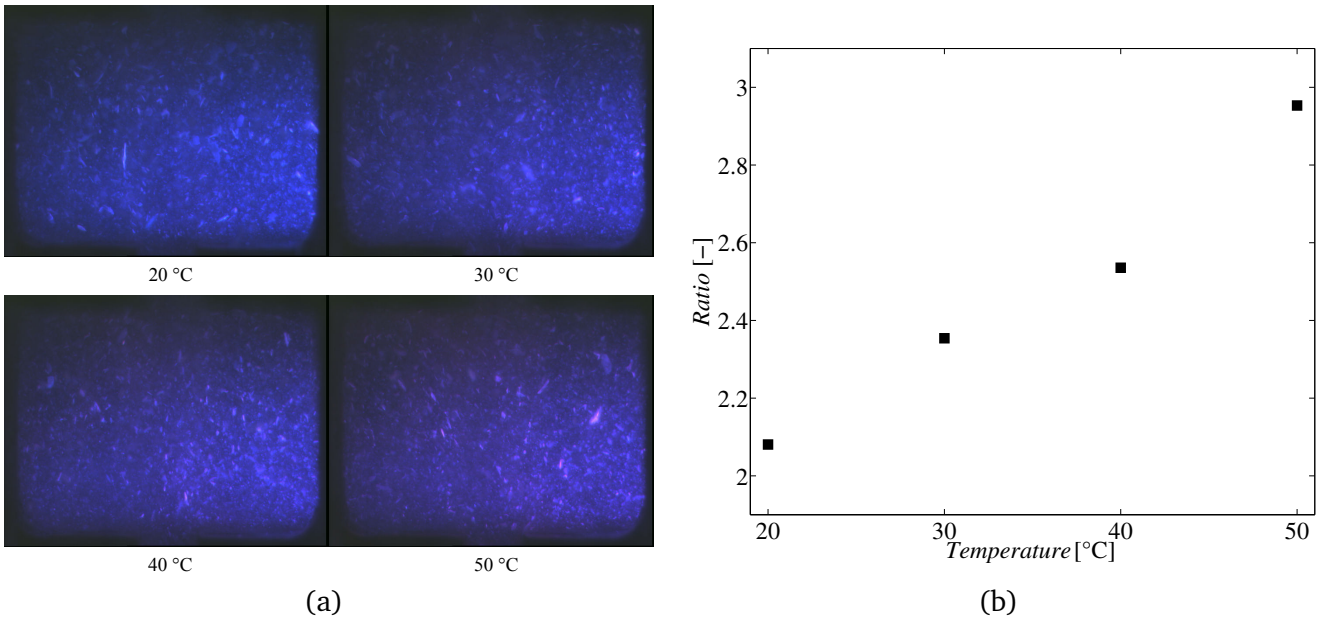

Figure 5.27: In (a) images of polystyrene flakes dyed with EuTTA and perylene taken by a 3-CCD-colour-camera at different temperatures are shown. A slight colour shift from blue to pink can be recognized by visual inspection. The ratio of the mean intensity in the blue image divided by the intensity in the red image for different temperatures is illustrated in (b).

Investigations of the spectra of polystyrene films dyed with EuTTA and perylene did not show any hysteresis in its emission intensity in both spectral bands.

For high resolution measurements, however, the produced polymer particles cannot be used, as they are firstly too big in size and secondly the size is strongly varying ($\approx$ 50 µm to 1 mm). If an appropriate technique is found that allows the fabrication of small, spherical particles with minor variation in size, this technique has a great potential to be used for simultaneous temperature and velocity measurements.

5.3 LIF for temperature field measurements during nucleate boiling

The developed PIT-method should be used to measure temperature and velocity fields during phase change processes, in particular nucleate boiling. At the Institute of Technical Thermodynamics at Technische Universität Darmstadt, an installation has been realized that allows the formation and optical observation of single vapor bubbles. To prove in advance the applicability of optical measurement methods in general, the ratiometric LIF method with dissolved dyes is used in combination with this setup. All details concerning the LIF method can be found in section 3.3, while for the setup generating the vapor bubbles it is referred to [53]. Data processing is carried out according to section 4.3. Due to the transient behavior of the observed nucleate boiling, no temporal averaging can be performed for the measurement data. If not specified differently, a 7×7 pixels median filter is applied to all temperature arrays presented in this section.

5.3.1 Measurement certainty and errors

Refraction at the liquid-vapor interface

When optical measurement techniques are used for the investigation of boiling phenomena, the occurring changes from liquid to vapor phase must be taken into account as an source of errors. At this interface a step in the refractive index leads to optical refraction and dispersion. In Figure 5.28 these effects are explained for the case of an elliptically shaped object (bubble) in a fluorescing fluid illuminated by a laser light sheet.

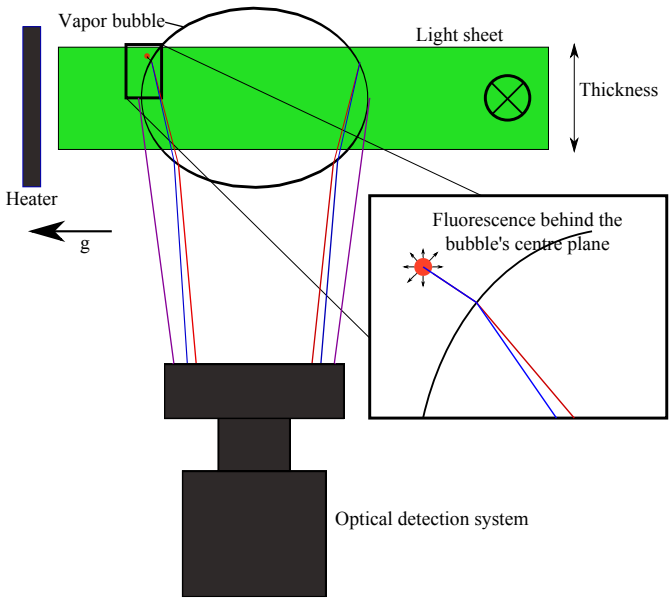

Figure 5.28: Illustration of chromatic dispersion caused by refraction at the liquid/vapour interface

Due to the thickness of the light sheet and the slightly varying position of bubble growth, there are fluorescing regions in front of and behind the vapour bubble. These regions cause the blurring of the liquid vapour interface in the images as illustrated in Figure 5.29. Refraction at the liquid-vapour-interface leads to a displacement of one fluorescing point in the object plane in relation to the corresponding point in the image plane. Furthermore, the wavelength dependency of the refractive index causes a spatial split-up of the temperature-sensitive and the reference signal (chromatic dispersion), which induces a

falsification of the ratio at these positions and leads to erroneous temperatures. This phenomenon is illustrated by the blue and red lines in Figure 5.28.

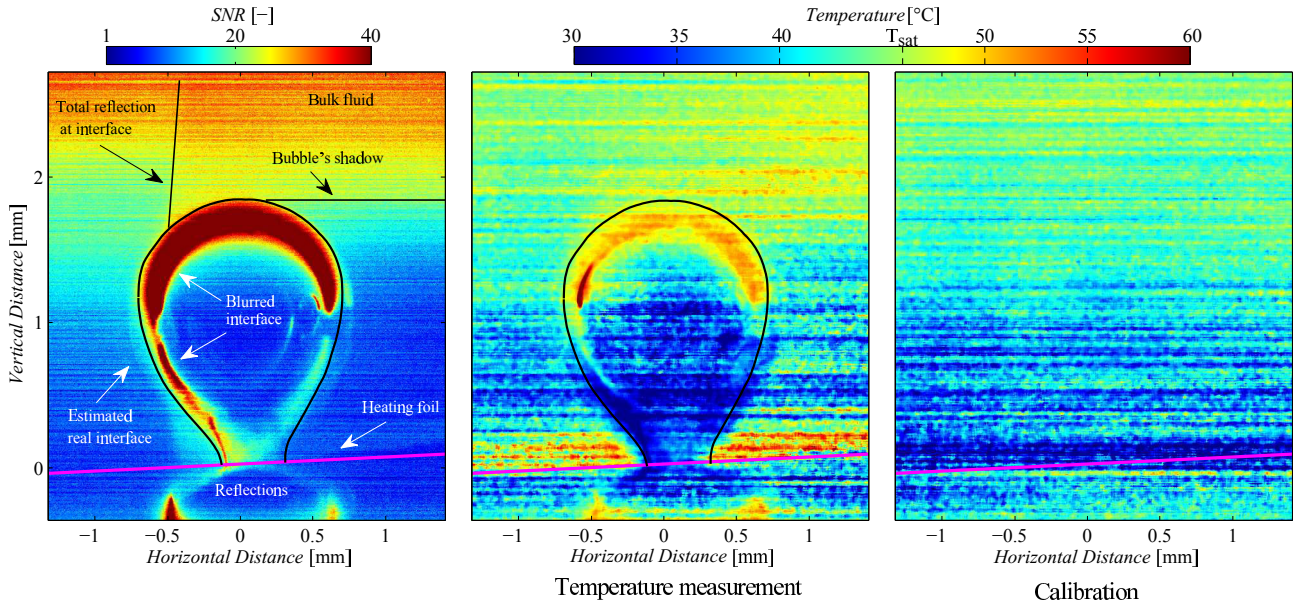

Figure 5.29: Illustration of optical effects and measured temperature for a growing bubble and the respective calibration images. On the very left the signal to noise ratio is displayed, which corresponds to the image brightness. Signal to noise ratio is calculated according to equation 5.3. All three subplots show the same image section.

In Figure 5.29 the erroneous temperatures at the blurred liquid-vapour interface can be observed. A symmetry to the horizontal axis through the bubble's center is recognizable, which ascertains the assumption that these errors are caused by the previously explained refraction at the interfaces.

Thus, the temperature can only be determined properly outside the real interface that is estimated from the bubbles shadow and the bubble foot. Further, the measured temperature in the bulk fluid above the bubble shows only little variations from the saturation temperature. On the left and the right side of the vapour bubble the results deviate clearly from the expected fluid temperature. This cannot be attributed to a real drop in temperature, but it must be a measurement error, as the temperature field calculated from a calibration image shows the same cold regions. For the calibration images a homogeneous distribution of temperature can be guaranteed and thus the cold areas observed in the temperature fields must be caused by measurement effects. Although only a global calibration has been performed, local differences of the brightness in the image are considered by a normalization, as described in section 4.1.7. A local calibration does not yield better results, since the particular low signal to noise ratio (see left image) at the relevant positions impedes the accurate determination of calibration polynomials. Thus, the low signal to noise ratio causes the incorrect determination of temperature at these positions.

Another problem associated with the low signal to noise ratio is the reduced measurement precision, which will be explained in more detail in the next section.

In the temperature field for the bubble measurements a zone of hot fluid above the heater can clearly be recognized. As this hot layer does not exist in the calibration results, where the heater is switched off, this observation can only be explained by the real existence of such a hot zone. The domain below the marked heater shows the reflections of the above fluorescence and has no relevance.

Signal to noise ratio

As stated before and illustrated in Figure 5.29, the signal to noise ratio of the acquired images is low, which causes a high measurement uncertainty. In the utilizable image regions, the SNR ranges from 10 to 30. It is computed according to equation 5.3 from the SNR of the unfiltered single images A and B. The domains in the image, where the phenomena that are worth examination take place, exhibit a local mean SNR of approximately 9. With a temperature sensitivity of 1.4 %/K, the uncertainty (standard deviation of temperature measurements) from the cameras' noise is estimated to be approximately ±7.9 K.

The actual precision of the measurement technique can be estimated from the standard deviation of temperature determined from experiments with a homogeneous and constant temperature distribution. These criteria are met well by the calibration data. Only part of the image is of interest and the standard deviation is depending on the images' local brightness. Hence, only this region of interest, more precisely the area where the layer of hot fluid is observed in the single bubble experiments, is taken into account. Calculating the standard deviation of temperature for the calibration images in the specified region, without applying a 7 × 7 pixels median filter, results in a numeric value of ±8.4 K. From these findings it can be concluded that the main source of errors is the images' low SNR, particularly in the region of interest. Thus, an increase of the images brightness leads to an significantly higher measurement precision.

This is confirmed by the results presented in Figure 5.30, showing the data of a measurement with reduced magnification. For this reason, the images are significantly brighter, which again means a higher SNR. The scale used to display the temperatures as colours is the same for both Figure 5.30 and Figure 5.29. It can clearly be recognized that the temperature variation is smaller in Figure 5.30.

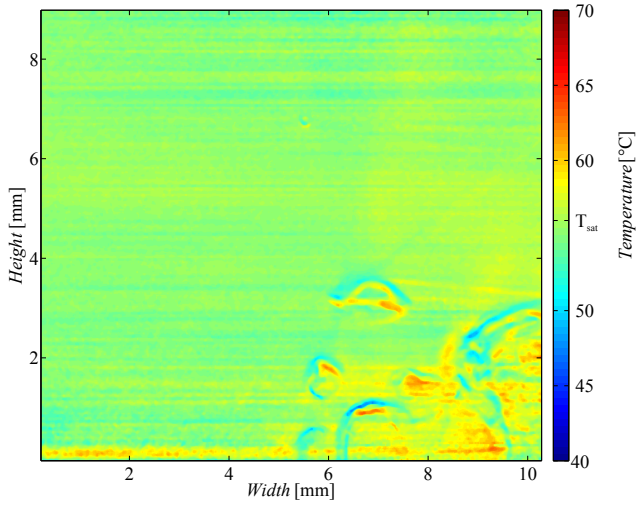

Figure 5.30: Temperature field for images with higher signal-to-noise ratio. Due to the high power input by exciting laser light on the heater, "explosive" nucleate boiling is observed.

On the right side of this temperature field, however, some rising vapor bubbles can be observed, which is a problem associated with the increased excitation irradiance. As the heater absorbs a part of the radiant energy incident on its surface, local hot zones on the heater occur. At these hot areas rapid evaporation takes place, causing the rapid bubble growth that can be seen in this Figure. Hence, increasing the images' brightness can not be realized by simply increasing the laser power. In fact, the electric power of the heater, the temperature of the bulk fluid as well as the laser power, the position and the direction of the light sheet must be matched very precisely with regard to the maximization of the

SNR in the resulting images. Additionally, the dye concentrations in the fluid influences the magnitude of the fluorescent signal.

5.3.2 Measurements of bubble growth and detachment

Due to the reduced measurement precision, which was analyzed in the previous section, the following results are commented only with regard to their qualitative nature. In Figure 5.31 one cycle of growth and detachment of a single vapour bubble is illustrated. Acetone is used for this measurements at an absolute pressure of 700 mbar. As the determination of temperature is only feasible outside the interface marked in Figure 5.29, no statement about the temperature in the zone where the bubble is in direct contact with the heater can be made. However, the hot fluid layer sitting above the heater seems to be pushed aside by the growing vapour bubble and flows back when the bubble detaches. This has also been observed in numerical simulations by Kunkelmann [35] and in experiments by Schweizer [67]. Schweizer measured the heating foil temperature from the bottom by means of an IR-camera and registered a local cooling of the foil at the bubble foot position. Consequently, it can be stated that temperature measurements in the liquid phase of acetone during a bubble cycle are feasible by means of the LIF-method. In future experiments the temperature profile in the layer with overheated fluid and also in vicinity of the liquid-gas interface might be resolvable, since the measurement precision still has great potential for optimization.

An area of $4.4 \times 4.4\ \mu m^2$ in the object plane is imaged onto one pixel in the raw images. The optical setup allows a further increase of the magnification. However, this would also lead to a reduction of the already low SNR. The image acquisition rate and thus the temporal resolution is limited to 1000 Hz by the pulse repetition rate of the Nd-YAG-Laser, while the cameras allow framerates up to 3000 Hz. Consequently, the presented results show the highest possible temporal resolution (1 ms) achievable with this setup. A reduction of the bubble frequency and thus a prolongation of one bubble cycle is aspired.

5.3.3 Conclusions for particle-based temperature measurements

The use of PIT-methods for the simultaneous measurement of temperature and velocity might overcome the problem of the blurred liquid-vapor interface described in section 5.3.1, because particles that are not located in the focal plane of the imaging system appear distorted. Therefore, it can be distinguished between signals coming from in- or out-of-focus particles.

While velocity fields are supposed to be measurable with a rather high precision, the accuracy of the developed technique using microencapsulated fluorescent dyes for temperature measurements still needs further development. As the nucleate boiling shows highly transient behavior, no temporal averaging can be performed. Hence, the precision of the technique (see section 5.1) must be significantly enhanced with regard to the determination of temperature fields for single shot measurements.

Moreover, the signal from the dissolved dyes is stronger, but still barely sufficient for the measurements requiring high magnification. Thus, the signal of the particle-based technique is expected to be too low for these measurements.

Concluding, it can be stated that currently the particle-based technique presented in section 3.1 and 5.1 is not feasible for temperature measurements during nucleate boiling, as presented above.

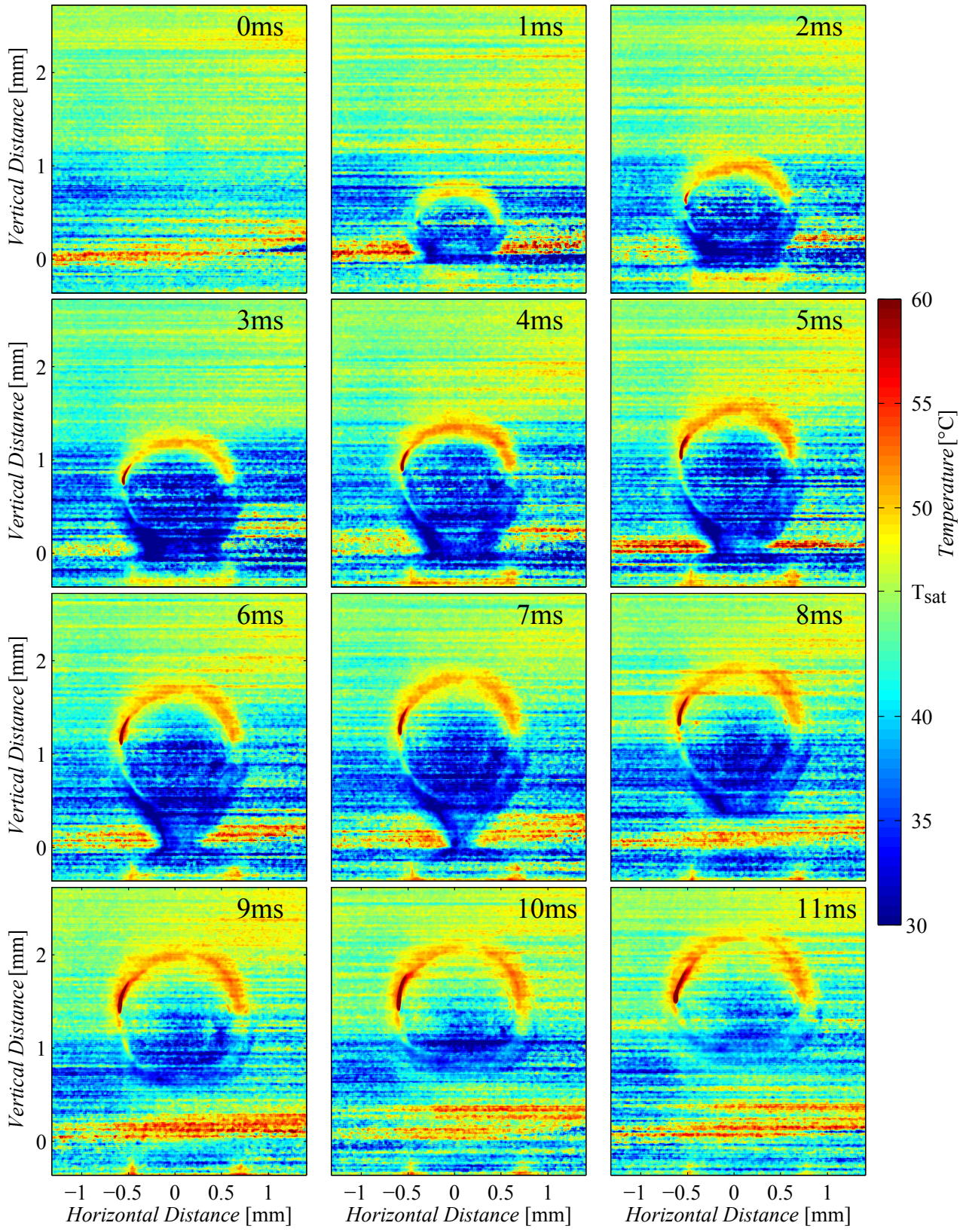

Figure 5.31: Cycle of growth and detachment of a single vapor bubble. The axis mark the corresponding distance from the nucleation site.

6 Summary and Outlook

The objective of the present thesis was the development of a technique for the simultaneous measurement of temperature and velocity fields based on luminescent particles and the characterization of this measurement method. During the development, the main focus is put on the temperature measurement, since existing methods can be used for the determination of velocity fields. Basically two different approaches are presented using microencapsulated dyes and dyed polymer particles. While the latter one is only investigated with regard to its elementary applicability for temperature measurements, the approach using microcapsules is analyzed in detail. Additionally, the feasibility of the well-established LIF method using dissolved dyes for temperature measurements in the liquid around a growing vapour bubble is studied. These parts of present thesis will be summarized in the following.

6.1 Microencapsulated dyes

The novel particle image thermometry method introduced in this thesis uses a microencapsulated solution of fluorescent dyes for simultaneous determination of temperature and velocity fields. The solid shell of the developed microcapsules has an outer diameter of 8.9 μm and is made from poly(methyl methacrylate), while the core solution consists of two fluorescent dyes (PM597-8C9 and PM567) dissolved in hexadecane. Using this dye mixture, a 2-colour-LIF approach can be applied, which is necessary to compensate for fluctuating fluorescent intensities of the particles. Therefore, the signal emitted by the reference dye (PM567) is divided by the signal of the temperature-sensitive dye (PM597-8C9), resulting in a ratio that only depends on temperature.

The separate detection of both fluorescent signals is carried out by two high-speed cameras (CMOS-cameras) equipped with an appropriate beamsplitter and filters. From the particles' brightnesses in the images of both cameras, temperature fields can be determined, while velocity fields result from the displacement of particles in subsequent images of one camera.

In order to extract relevant information from the acquired images, image processing algorithms were developed. The first step of this processing is the matching of the corresponding images from both cameras. For this purpose, a self-calibration approach is applied using the particle images themselves to derive a transform function that is employed for alignment of the images. Further processing depends on the actual application. For images with a high-seeding density (distance between particles in the image is marginal), a pixelwise division of the corresponding images from both cameras is performed and appropriate averaging procedures are applied to the resulting ratio-matrizes. These averaged matrices are then used in combination with calibration polynomials derived from in-situ calibration measurements, to determine the temperature fields. For images with lower seeding density, a particle detection is performed and the ratio is determined only at positions where particles are present. The resulting ratio-matrices are averaged as well and converted to temperature fields using in-situ calibration measurements.

The applicability of the developed microcapsules for simultaneous measurement of temperature and velocity fields is demonstrated experimentally for light-sheet and volume illumination.

Light-sheet illumination

Applicability for light-sheet illumination has been investigated using a cubic cell with $10 \times 10 \times 10$ mm^3 inner dimensions and four transparent walls made from acrylic glass. This setup enables illumination from the top and signal detection perpendicular to the measurement plane generated by the light-sheet.

Due to differently tempered side walls, a two-dimensional, stationary temperature- and flow-profile establishes that can easily be reproduced by a numerical simulation.

The velocity- and temperature-fields measured by the presented technique with microcapsules are in good agreement with the results of the numerical simulation. A measurement acquisition rate of 1000 Hz has been achieved by the use of high-speed cameras in combination with a pulsed laser. To attain this acquisition rate, each image was illuminated by a single laser pulse. The temperature measurements exhibit a 95 % confidence interval of ± 6 K, when appropriate averaging procedures are applied. For that case, one point in the resulting temperature field corresponds to an area of 60×60 μm^2 in the measurement plane and the temporal resolution is 33 ms. Depending on the particular application, averaging procedures can be adapted to increase the precision of the technique under acceptance of a reduced temporal and spatial resolution.

Volume illumination

In many microfluidic devices a single optical access is available making the application of volume illumination necessary. In order to investigate the applicability of the developed measurement technique for volume illumination, a setup has been realized that facilitates the creation of a distinct, 3-dimensional temperature profile in a capillary tube with an inner diameter of 580 μm. Glycerol is used as medium carrying the microcapsules. It flows inside the capillary tube and surrounds the tube also from the outside. By this means, refraction phenomena at the curved interfaces are compensated in large parts by refractive index matching.

A 2-dimensional temperature field is measured in the plane coincident with the rotational axis of the capillary tube, using an inverted microscope in combination with the 2-camera assembly. Due to the low seeding density that is required for applications with volume illumination, an extensive temporal averaging has to be performed, in order to have enough particles at all positions in the accumulated image. Although a temporal averaging over 500 images has been performed in present case, the precision of the measurement results is comparatively low (95 % confidence interval ranging from ± 6.9 K to ± 8.6 K). A single point in the evaluated temperature field corresponds to an area of 8×8 μm^2 in the measurement plane. Despite the low precision, comparing numerical and measured temperature profiles, a good qualitative agreement can be found with only minor deviations (ranging from 0.2 K to 1.6 K) of their mean values. These findings imply that the presented measurement technique – on the contrary to LIF methods with dissolved dyes – can be applied in the case of volume illumination, even if temperature gradients perpendicular to the measurement plane are present. Due to the required temporal averaging, only steady-state phenomena can be investigated.

Sources of errors and future improvements

The variation of intrinsic particle properties was identified as the main source of errors. To be more precise, the measured ratio shows a high deviation when numerous particles, all being at the same temperature, are examined separately. The most probable reason for this observation is an overlap of absorption and emission spectra of the dyes in the microcapsules' core solution. This causes a stronger re-absorption of the reference signal in the capsules' core. Therefore, the ratio depends on the microcapsules' diameter that fluctuates due to the manufacturing process. The cameras' noise contributes to the fluctuations of the measured temperature only in little parts. A further reason that the precision of the presented technique is small compared to LIF with dissolved dyes, is its low temperature sensitivity (0.5 %/K).

Based on the findings above, the precision of the measurement technique can be strongly increased, if a combination of dyes is found that is also soluble in non-polar liquids, showing a reduced re-absorption and a higher temperature sensitivity.

6.2 Dyed polymer particles

Another possibility to generate particles with temperature-sensitive fluorescence properties is to incorporate appropriate dyes in a polymer. Therefore, the dyes are added to a solution of the polymer with subsequent extraction of the solvent (e.g. by evaporation) resulting in dyed solid polymers that can also be prepared as microparticles with a spherical shape.

Polymers with dyes excitable at λ = 532 nm

Various dyes that show potential for ratio-metric LIF measurements when they are dissolved in water or ethanol have been incorporated in different polymers and investigated with regard to their temperature sensitivity. All these dyes can be excited by the available laser with an emission wavelength of 532 nm. The fluorescence properties of the dyes are strongly influenced by their environment and hence by the polymer characteristics. None of the investigated combinations of dyes and polymer are suitable for temperature measurements.

Polymers dyed with EuTTA and perylene

The absorption maxima of the dyes EuTTA and perylene, also used in temperature sensitive paints, are in the ultraviolet wavelength range, precluding utilization of the available laser. However, this dye combination is suggested by [4] to be used as temperature sensor on surfaces when they are incorporated in a polystyrene film.

In the present thesis such films are prepared and investigated with regard to their applicability for temperature measurements in liquids. Therefore, the polymer films were mechanically pulverized and the resulting flakes were dispersed in water. This dispersion was filled in a temperable container and illuminated by an UV-LED. The emitted signal is detected by means of a spectrometer and a 3-CCD-RGB camera. Analyzing the acquired spectra and RGB-images, a temperature sensitivity of approximately 1.0 %/K has been calculated for the dyed polymer flakes. Consequently, it can be stated that these dyes in polystyrene are suitable for temperature measurements in liquids.

For their use as temperature and velocity sensors, particles with a uniform size and a spherical shape must be developed. If such particles can be fabricated, similar setups and processing algorithms as for the microcapsules can be used.

Improvements and Applications

An appropriate method for fabrication of such particles must guarantee that no dye diffusion from the particles to the surrounding medium occurs during curing of the polymer. This is necessary to ensure that all particles contain the same concentrations of dyes. If the particles are used for temporally and spatially highly resolved measurements, illumination must be realized by a pulsed UV-laser, since the LED used in this thesis cannot provide sufficient excitation energy.

In case that spherical particles can be fabricated economically, they can be used as a "Low-cost-method" for simultaneous velocity and temperature field measurements. Instead of two expensive high-speed cameras in combination with a quite sophisticated installation of beamsplitters and optical filters, a single comparatively economic 3-CCD-RGB camera can be used (due to the large shift of emission peaks of temperature-sensitive and reference signal) for signal detection. Additionally, for measurements that do not require a high resolution, the excitation can still be realized by an UV-LED instead of using a quite expensive pulsed laser. However, the particles movement will cause streak patterns in the acquired images, if a continuous illumination is installed. The processing of such images requires special image

processing algorithms that were developed in the framework of the Graduiertenkolleg 1114[1] by Voss et al. [86] and might also be used in the aforementioned "Low-cost-method".

6.3 LIF with dissolved dyes

The 2-colour-LIF method with dissolved dyes has been extensively studied in previous works. Its implementation for temperature measurement requires less effort than the microcapsule technique developed in this thesis. In the framework of this thesis it is used for the measurement of temperature fields during nucleate boiling. Thus, the applicability of optical measurement methods for the experimental study of such highly transient, small scale phenomena is investigated.

Applicability for temperature measurements during nucleate boiling

An appropriate dye combination soluble in acetone and suitable for temperature measurements by means of the 2-colour-LIF principle had to be identified. In literature no such dye combination could be found, because commonly LIF measurements are performed in aqueous solutions with RhB and Rh110. In present work a combination of DCM and Rh19 is used.

The experimental setup for the generation and observation of vapour bubbles at a defined position has been developed in a separate project and is therefore only rudimentarily described in this thesis.

The optical system is the same used for the natural convection experiments with microcapsules and enables an acquisition rate of 1000 Hz. Thus, it is possible to resolve a bubble cycle with approximately 15 images. The results show that the temperature near the liquid-vapour interface cannot be determined due to diffraction effects. Furthermore, a high uncertainty (± 8 K) was recognized which can be attributed to a low signal-to-noise-ratio and missing possibilities for averaging. The low signal-to-noise-ratio is caused by the high optical magnification and a non-satisfying illumination of the investigated area around the vapour bubble. The latter one might be improved in future experiments. Nevertheless, qualitative results are in good agreement with previous experimental studies and numerical investigations.

The fluorescent signal emitted from the dissolved dyes is much higher than the signal from the developed microcapsules. Additionally, the measurement precision of the PIT technique presented in this thesis is lower than for the LIF technique using DCM and Rh19 in acetone.

Considering the previously described restrictions for the temperature measurements around a growing vapour bubble using the LIF method with dissolved dyes, it must be stated that the particle based method is not suited for this kind of measurements, in its present stage of development.

Future Applications

The LIF-method with dissolved dyes can be used for high-resolution temperature measurements at an evaporating meniscus similar to the experiments described by Song et al. [74]. Further fluids, like ethanol or acetone, can be investigated, since appropriate dye combinations are available.

[1] Graduate school: Optical measurement methods for characterization of transport phenomena at interfaces.

Bibliography

[1] Adrian, R.: *Twenty years of particle image velocimetry*. Experiments in Fluids, 39:159–169, 2005.

[2] Allison, S. and G. Gillies: *Remote thermometry with thermographic phosphors: Instrumentation and applications*. Review of Scientific Instruments, 68:2615–2650, 1997.

[3] Atkins, P., A. Höpfner, A. Schleitzer und M. Bär: *Physikalische Chemie*, Bd. 2. Wiley-Vch, 1990.

[4] Basu, B. and S. Venkatraman: *Fabrication of a bi-luminophore temperature sensitive coating by embedding europium thenoyltrifluoroacetonate (EuTTA) and perylene in polystyrene*. Journal of fluorescence, 19(3):479–485, 2009.

[5] Benita, S.: *Microencapsulation: methods and industrial applications*. Taylor & Francis, 2006.

[6] Bown, M., J. MacInnes, and R. Allen: *Micro-PIV simulation and measurement in complex microchannel geometries*. Measurement Science and Technology, 16:619, 2005.

[7] Brown E.N., Kessler M.R., S.N. and W. S.R.: *In situ poly (urea-formaldehyde) microencapsulation of dicyclopentadiene*. Journal of Microencapsulation, 20:719–730, 2003.

[8] Brübach, J.: *Spektroskopische Methoden zur oberflächennahen Thermometrie in technischen Verbrennungsumgebungen*. Dissertation, TU Darmstadt, 2008.

[9] Brübach, J., A. Patt, and A. Dreizler: *Spray thermometry using thermographic phosphors*. Applied Physics B: Lasers and Optics, 83:499–502, 2006.

[10] Bruchhausen, M., F. Guillard, and F. Lemoine: *Instantaneous measurement of two-dimensional temperature distributions by means of two-color planar laser induced fluorescence (PLIF)*. Experiments in fluids, 38:123–131, 2005.

[11] Castanet, G., P. Lavieille, M. Lebouché, and F. Lemoine: *Measurement of the temperature distribution within monodisperse combusting droplets in linear streams using two-color laser-induced fluorescence*. Experiments in fluids, 35:563–571, 2003.

[12] Chamarthy, P., H. Dhavaleswarapu, S. Garimella, J. Murthy, and S. Wereley: *Visualization of convection patterns near an evaporating meniscus using μPIV*. Experiments in Fluids, 44:431–438, 2008.

[13] Chamarthy, P., S. Garimella, and S. Wereley: *Measurement of the temperature non-uniformity in a microchannel heat sink using microscale laser-induced fluorescence*. International Journal of Heat and Mass Transfer, 53:3275–3283, 2010.

[14] Comsol: *Comsol Multiphysics v4.2 User's guide*, 2011.

[15] Coolen, M., R. Kieft, C. Rindt, and A. Van Steenhoven: *Application of 2-d LIF temperature measurements in water using a Nd:YAG laser*. Experiments in Fluids, 27:420–426, 1999.

[16] Coppeta, J. and C. Rogers: *Dual emission laser induced fluorescence for direct planar scalar behavior measurements*. Experiments in Fluids, 25:1–15, 1998.

[17] CVI: *The CVI melles griot technical guide*. Techn. rep., CVI Melles Griot, 2009.

[18] Dabiri, D.: *Digital particle image thermometry/velocimetry: a review*. Experiments in Fluids, 46:191–241, 2009.

[19] Deprédurand, V., P. Miron, A. Labergue, M. Wolff, G. Castanet, and F. Lemoine: *A temperature-sensitive tracer suitable for two-colour laser-induced fluorescence thermometry applied to evaporating fuel droplets*. Measurement Science and Technology, 19:105403, 2008.

[20] Dreizler, A., T. C. und K. Hufnagel: *Messtechnik im Maschinenbau*. Vorlesungsunterlagen Sommersemester 2010, TU Darmstadt, 2010.

[21] Drexhage, K.: *Dye lasers*, ch. Structure and properties of laser dyes, pp. 144–193. Springer, Berlin, 1977.

[22] Funatani, S., N. Fujisawa, and H. Ikeda: *Simultaneous measurement of temperature and velocity using two-colour LIF combined with PIV with a colour CCD camera and its application to the turbulent buoyant plume*. Measurement Science and Technology, 15:983–990, 2004.

[23] Grabe, M.: *Measurement uncertainties in science and technology*. Springer, 2005.

[24] Gränicher, H.: *Messung beendet-was nun?: Einführung und Nachschlagewerk für die Planung und Auswertung von Messungen*. vdf, Hochschulverlag AG an der ETH Zürich, 1996.

[25] Haken, H. und H. C. Wolf: *Molekülphysik und Quantenchemie*. Springer, 2006.

[26] Hishida, K. and J. Sakakibara: *Combined planar laser-induced fluorescence–particle image velocimetry technique for velocity and temperature fields*. Experiments in fluids, 29:129–140, 2000.

[27] Hoffmann, M., M. Schlüter, and N. Räbiger: *Experimental investigation of liquid–liquid mixing in T-shaped micro-mixers using μ-LIF and μ-PIV*. Chemical engineering science, 61:2968 – 2976, 2006.

[28] Jähne, B.: *Digitale Bildverarbeitung*. Springer, 2005.

[29] Keane, R. and R. Adrian: *Theory of cross-correlation analysis of piv images*. Applied scientific research, 49:191–215, 1992.

[30] Khalid, A. and K. Kontis: *Thermographic phosphors for high temperature measurements: principles, current state of the art and recent applications*. Sensors, 8:5673–5744, 2008.

[31] Khalil, G., K. Lau, G. Phelan, B. Carlson, M. Gouterman, J. Callis, and L. Dalton: *Europium beta-diketonate temperature sensors: Effects of ligands, matrix, and concentration*. Review of scientific instruments, 75:192–207, 2004.

[32] Kim, H., K. Kihm, and J. Allen: *Examination of ratiometric laser induced fluorescence thermometry for microscale spatial measurement resolution*. International journal of heat and mass transfer, 46:3967–3974, 2003.

[33] Kissel, T.: *Spektroskopische Methoden zur Charakterisierung wandnaher Verbrennungsvorgänge*. Dissertation, TU Darmstadt, 2011.

[34] Knauer, O., M. Lang, A. Braeuer, and A. Leipertz: *Simultaneous determination of the composition and temperature gradients in the vicinity of boiling bubbles in liquid binary mixtures using one-dimensional raman measurements*. Journal of Raman Spectroscopy, 42:195–200, 2011.

[35] Kunkelmann, C.: *Numerical Modeling and Investigation of Boiling Phenomena*. PhD thesis, TU Darmstadt, 2011.

[36] Labergue, A., V. Deprédurand, A. Delconte, G. Castanet, and F. Lemoine: *New insight into two-color LIF thermometry applied to temperature measurements of droplets*. Experiments in fluids, 49:547–556, 2010.

[37] Lakowicz, R.: *Principles of Fluorescence Spectroscopy*. Springer, 2006.

[38] Lamb, H.: *Hydrodynamics*. Cambridge University Press, 1993.

[39] Larsen, L. and J. Crimaldi: *The effect of photobleaching on PLIF*. Experiments in fluids, 41:803–812, 2006.

[40] Lavieille, P., A. Delconte, D. Blondel, M. Lebouché, and F. Lemoine: *Non-intrusive temperature measurements using three-color laser-induced fluorescence*. Experiments in fluids, 36:706–716, 2004.

[41] Lavieille, P., F. Lemoine, G. Lavergne, and M. Lebouché: *Evaporating and combusting droplet temperature measurements using two-color laser-induced fluorescence*. Experiments in fluids, 31:45–55, 2001.

[42] Lemoine, F., Y. Antoine, M. Wolff, and M. Lebouche: *Simultaneous temperature and 2d velocity measurements in a turbulent heated jet using combined laser-induced fluorescence and LDA*. Experiments in Fluids, 26:315–323, 1999.

[43] Liebig, M.: *Charakterisierung einer Methode zur Temperaturfeldmessung basierend auf der Fluoreszenz mikrogekapselter Farbstoffe*. Diplomarbeit, TU Darmstadt, 2010.

[44] Lindken R., Westerweel J., W.B.: *Development of a self-calibrating stereo-μ-PIV system and its application to the three-dimensional flow in a T-shaped mixer*. In *6th International Symposium on PIV, Pasadena, California, USA*, 2005.

[45] Liu, T. and J. Sullivan: *Pressure and temperature sensitive paints*. Springer Verlag, 2004.

[46] López Arbeloa, T., M. Tapia Estevez, F. López Arbeloa, I. Urretxa Aguirresacona, and I. López Arbeloa: *Luminescence properties of rhodamines in water/ethanol mixtures*. Journal of Luminescence, 48:400–404, 1991.

[47] Maqua, C., G. Castanet, F. Lemoine, N. Doue, and G. Lavergne: *Temperature measurements of binary droplets using three-color laser-induced fluorescence*. Experiments in fluids, 40:786–797, 2006.

[48] Mathworks: *Matlab Image processing toolbox user's guide*, 2008.

[49] Meinhart, C., S. Wereley, and M. Gray: *Volume illumination for two-dimensional particle image velocimetry*. Measurement Science and Technology, 11:809, 2000.

[50] Nasarek, R.: *Temperature Field Measurements with High Spatial and Temporal Resolution Using Liquid Crystal Thermography and Laser Induced Fluorescence*. PhD thesis, TU Darmstadt, 2010.

[51] Natrajan, V. and K. Christensen: *Two-color laser-induced fluorescent thermometry for microfluidic systems*. Measurement Science and Technology, 20:015401–, 2009.

[52] O'Donnell, P. and J. McGinity: *Preparation of microspheres by the solvent evaporation technique*. Advanced Drug Delivery Reviews, 28:25–42, 1997.

[53] Oltmann, S.: *Untersuchung der Temperaturverteilung in der Flüssigkeit beim Blasensieden mittels Laser Induzierter Fluoreszenz*. Diplomarbeit, TU Darmstadt, 2012.

[54] Omrane, A., F. Ossler, and M. Aldén: *Temperature measurements of combustible and non-combustible surfaces using laser induced phosphorescence*. Experimental thermal and fluid science, 28:669–676, 2004.

[55] Pereira, F. and M. Gharib: *Defocusing digital particle image velocimetry and the three-dimensional characterization of two-phase flows*. Measurement Science and Technology, 13:683ff, 2002.

[56] Plewinsky, B.: *Das Ingenieurwissen*, Kap. C Chemie. Springer, 2004.

[57] Preusche, A.: *Untersuchung der Eigenschaften eines Fluoreszenzfarbstoffes bei Einbindung in Mikropartikel aus Polymeren*. Diplomarbeit, TU Darmstadt, 2009.

[58] Romano, V., A. Zweig, M. Frenz, and H. Weber: *Time-resolved thermal microscopy with fluorescent films*. Applied Physics B: Lasers and Optics, 49:527–533, 1989.

[59] Ross, D., M. Gaitan, and L. Locascio: *Temperature measurement in microfluidic systems using a temperature-dependent fluorescent dye*. Analytical Chemistry, 73:4117–4123, 2001.

[60] Sakakibara, J. and R. Adrian: *Whole field measurement of temperature in water using two-color laser induced fluorescence*. Experiments in Fluids, 26(1):7–15, 1999.

[61] Sakakibara, J. and R. Adrian: *Measurement of temperature field of a Rayleigh-Bénard convection using two-color laser-induced fluorescence*. Experiments in fluids, 37:331–340, 2004.

[62] Sakakibara, J., K. Hishida, and M. Maeda: *Measurements of thermally stratified pipe flow using image-processing techniques*. Experiments in Fluids, 16(2):82–96, 1993.

[63] Sakakibara, J., K. Hishida, and M. Maeda: *Vortex structure and heat transfer in the stagnation region of an impinging plane jet (simultaneous measurements of velocity and temperature fields by digital particle image velocimetry and laser-induced fluorescence)*. International journal of heat and mass transfer, 40(13):3163–3176, 1997.

[64] Schmidt-Rohr, K. and H.W. Spiess: *Nature of nonexponential loss of correlation above the glass transition investigated by multidimensional nmr*. Phys. Rev. Lett., 66:3020–3023, 1991.

[65] Schorr, J.: *Entwicklung und Anwendung von Fluoreszenztracer-Verfahren für die lasergestützte, abbildende Spraydiagnostik*. Dissertation, Universität Heidelberg, 2003.

[66] Schulz, C. and V. Sick: *Tracer-LIF diagnostics: quantitative measurement of fuel concentration, temperature and fuel/air ratio in practical combustion systems*. Progress in Energy and Combustion Science, 31(1):75–121, 2005.

[67] Schweizer, N.: *Multi-Scale Investigation of Nucleate Boiling Phenomena in Microgravity*. PhD thesis, TU Darmstadt, 2010.

[68] Sheng, J., E. Malkiel, and J. Katz: *Single beam two-views holographic particle image velocimetry*. Applied optics, 42:235–250, 2003.

[69] Shinohara, K., Y. Sugii, A. Aota, A. Hibara, M. Tokeshi, T. Kitamori, and K. Okamoto: *High-speed micro-PIV measurements of transient flow in microfluidic devices*. Measurement science and Technology, 15, 2004.

[70] Sigma Aldrich: *Sigma-Aldrich Chemie GmbH Produktkatalog*, 2009.

[71] Soloff, S., R. Adrian, and Z. Liu: *Distortion compensation for generalized stereoscopic particle image velocimetry*. Measurement science and technology, 8:1441–1454, 1997.

[72] Someya, S., D. Ochi, Y. Li, K. Tominaga, K. Ishii, and K. Okamoto: *Combined two-dimensional velocity and temperature measurements using a high-speed camera and luminescent particles*. Applied Physics B: Lasers and Optics, 99:325–332, 2010.

[73] Someya, S., S. Yoshida, Y. Li, and K. Okamoto: *Combined measurement of velocity and temperature distributions in oil based on the luminescent lifetimes of seeded particles*. Measurement Science and Technology, 20:025403, 2009.

[74] Song, X. and D. Nobes: *Experimental investigation of evaporation-induced convection in water using laser based measurement techniques*. Experimental Thermal and Fluid Science, 35:910–919, 2011.

[75] Spiegelberg, S.: *Herstellung von Mikropartikeln aus einem abbaubaren Multiblockcopolymer zur Freisetzung von proteinischen Wirkstoffen*. Dissertation, RWTH Aachen, 2004.

[76] Spurk, J. und N. Aksel: *Strömungslehre: Einführung in die Theorie der Strömungen*. Springer, 2005.

[77] Stephan, P.: *Skriptum zur Vorlesung Wärme-und Stoffübertragung*. Vorlesungsunterlagen, TU Darmstadt, 2009.

[78] Sugii, Y., S. Nishio, and K. Okamoto: *Measurement of a velocity field in microvessels using a high resolution piv technique*. Annals of the New York Academy of Sciences, 972:331–336, 2002.

[79] Susdorf, T.: *Photophysikalische Charakterisierung von Pyrromethen-Laserfarbstoffen in verschiedenen Festkörperpolymeren*. Dissertation, Universität Regensburg, 2006.

[80] SwRI: *Micro/Nano encapsulation*. Techn. rep., Southwest Research Institute® San Antonio, Texas, 2011.

[81] Tropea, C., A. Yarin, and J. Foss: *Springer handbook of experimental fluid mechanics*. Springer, 2007.

[82] Valeur, B.: *Molecular fluorescence: principles and applications*. Wiley-Vch, 2002.

[83] VDI-Gesellschaft Verfahrenstechnik (Hrsg.): *VDI-Wärmeatlas, 8. Auflage*. Springer-Verlag, 1997.

[84] Vennemann, P., K. Kiger, R. Lindken, B. Groenendijk, S. Stekelenburg-de Vos, T. ten Hagen, N. Ursem, R. Poelmann, J. Westerweel, and B. Hierck: *In vivo micro particle image velocimetry measurements of blood-plasma in the embryonic avian heart*. Journal of biomechanics, 39:1191–1200, 2006.

[85] Vogt, J.: *Charakterisierung der Messmethode laserinduzierte Fluoreszenz (LIF) zur Bestimmung von Temperaturfeldern in Flüssigkeiten*. Diplomarbeit, TU Darmstadt, 2008.

[86] Voss, B., J. Stapf, A. Berthe, and C. Garbe: *Bichromatic particle streak velocimetry bPSV*. Experiments in Fluids, pp. 1–16, 2012.

[87] Walker, D.: *A fluorescence technique for measurement of concentration in mixing liquids*. Journal of Physics E: Scientific Instruments, 20:217–224, 1987.

[88] Watts, P., M. Davies, and C. Melia: *Microencapsulation using emulsification/solvent evaporation: an overview of techniques and applications*. Critical reviews in therapeutic drug carrier systems, 7:235, 1990.

[89] Wereley, S. and C. Meinhart: *Microscale Diagnostic Techniques*, ch. Micron-resolution particle image velocimetry, pp. 51–112. Springer, 2005.

[90] Westerweel, J.: *Theoretical analysis of the measurement precision in particle image velocimetry*. Experiments in Fluids, 29:3–12, 2000.

[91] Wieneke, B.: *Stereo-PIV using self-calibration on particle images*. Experiments in fluids, 39:267–280, 2005.

[92] Willert, C. and M. Gharib: *Digital particle image velocimetry*. Experiments in fluids, 10:181–193, 1991.

[93] Wolff, M., A. Delconte, F. Schmidt, P. Gucher, and F. Lemoine: *High-pressure Diesel spray temperature measurements using two-colour laser-induced fluorescence*. Measurement Science and Technology, 18:697–706, 2007.

[94] Yeo, Y. and K. Park: *A new microencapsulation method using an ultrasonic atomizer based on interfacial solvent exchange*. Journal of controlled release, 100:379–388, 2004.

[95] Yin, W.: *Development of Novel Microencapsulation Processes*. PhD thesis, University of Rochester, 2009.

[96] Yoon, S. and K. Kim: *Signal intensity enhancement of μ-LIF by using ultra-thin laser sheet illumination and aqueous mixture with ethanol/methanol for micro-channel applications*. Optics and lasers in engineering, 44:224–239, 2006.

[97] Zelelow, B., G. Khalil, G. Phelan, B. Carlson, M. Gouterman, J. Callis, and L. Dalton: *Dual luminophor pressure sensitive paint:: II. lifetime based measurement of pressure and temperature*. Sensors and Actuators B: Chemical, 96:304–314, 2003.

Curriculum vitae

Persönliche Daten

Geburtsdatum	1. November 1981
Geburtsort	Miltenberg

Schulbildung

1988 - 1992	Grundschule Miltenberg
1992 - 2001	Johannes-Butzbach-Gymnasium Miltenberg

Studium

10/2002 - 10/2008	Maschinenbau an der Technischen Universität Darmstadt

Berufliche Tätigkeit

11/2008 - 01/2012	Promotion am Fachgebiet Technische Thermodynamik der Technischen Universität Darmstadt
seit 02/2012	Entwicklungsingenieur bei Alstom Power